Development of III-V nitride optoelectronic devices

Tseng, Chun-Lung

Award date:
2003

Awarding institution:
University of Bath

DEVELOPMENT OF III-V NITRIDE OPTOELECTRONIC DEVICES

Submitted by Chun-Lung Tseng
for the degree of
Doctor of Philosophy
of the University of Bath
2003

Signed :

ProQuest LLC
789 East Eisenhower Parkway
P.O. Box 1346
Ann Arbor, MI 48106-1346

Abstract

The development of III-nitride optoelectronic devices, including field emission electron emitters and high efficiency light emitting diodes, has been undertaken, involving the investigation of processing techniques and device design. This work comprises the study of the light transmission of Ni/Au contacts, ZnO growth, inductively-coupled plasma etching for GaN, and the damage induced by SiO_2 ion beam sputtering deposition. These studies were subsequently applied to the design of anti-reflection and current spreading using a Ni/Au/ZnO contact for p-GaN, and the fabrication of GaN nanotubes. The characteristics of field emission for the GaN nanotubes were also investigated.

The mechanism of increased light transmission for an annealed thin Ni/Au layer on p-GaN has been studied. The increase in light transmission is attributed to the open areas formed due to the formation of Ni/Au island structures after annealing. The importance of Au in the Ni/Au contact was thus investigated. It was found that the presence of Au is essential for lowering the contact resistance. ZnO growth by ion beam sputtering was performed for the further design of anti-reflection coating. The structural, electrical, and optical properties has been found to be sensitive to the substrate temperature and oxygen flow rate. According to the studies described above, a novel Ni/Au/ZnO contact for p-GaN was developed. The light transmission has been increased to 89% at a wavelength of 470 nm due to the additional ZnO film which acts as an anti-reflection layer. The additional ZnO layer also induced a better resistance match to the n-GaN in a GaN-based LED, resulting in better current spreading and higher light emission efficiency at the same injected current.

Inductively-coupled plasma etching for GaN has been investigated. It was found that the ICP power, RF power, and chamber pressure significantly affected the etch rate, DC bias and etched surface morphology. The etching technique was then applied to the fabrication of GaN nanotubes which have a wall thickness of $\sim$20nm and outer diameter of $\sim$200nm. One application for a field emission electron emitter, using the n-GaN nanotubes was explored. The turn-on electric field was effectively decreased with respect to the bulk n-GaN film due to the high geometric field enhancement. Damage induced by SiO_2 ion beam sputtering deposition was also studied. The decrease in the photoluminescence intensity from a multiple quantum well structure was observed after removing the coated SiO_2, indicating that the damage was mainly due to SiO_2 deposition.

Acknowledgements

For the past years there are many people who have provided support and guidance for my project and life. With regards to the work presented in this thesis, I would like to express gratitude to my supervisors, Prof. W. N. Wang and Prof. R. Stevens, for giving me the opportunity to undertake the research and for their guidance and encouragement.

Many thanks go to Dr. M. J. Youh, Dr. G. P. Moore, Dr. M. A. Hopkins and Dr. N. A. Fox for providing so much help and discussion for my research.

Many friends in Bath have helped me to adapt and appreciate life in the UK. Their patience and kindness has given me strong support while working long hours in the university.

Finally I can express my overwhelming appreciation to my wife whose help and encouragement, and company, has made this thesis possible.

Contents

1 Introduction **1**

1.1 Lighting – A Historical Perspective 1

1.2 Development of Group III-Nitrides 3

1.3 Development of Processing and Device Design for Group III-Nitrides 5

1.3.1 Ohmic Contacts for Group III-Nitrides 5

1.3.2 Etching for Group III-Nitrides 7

1.3.3 Field Emission from Group III-Nitrides 8

1.4 Aims and Objectives 9

References **11**

2 Transparent Ohmic Contact for p-GaN **14**

2.1 Introduction 14

2.1.1 Theory of Metal–Semiconductor Contacts 15

2.1.2 Measurement Methods of Specific Contact Resistance . . . 19

2.1.3 n-GaN Ohmic Contacts 23

2.1.4 p-GaN Ohmic Contacts 26

2.1.5 Transparent p-GaN Contacts 29

2.2 Mechanism of Transparency for Annealed Ni/Au Contact 31

2.2.1 Waves in Thin Film System 31

2.2.2 Reflectance 32

2.2.3 Interference 34

2.2.4 Optical Simulation for Ni/Au Contact on GaN 36

2.2.5 Surface Morphology of Ni/Au After Annealing 39

2.3 Development of Ni/Au/ZnO Transparent Contact for p-GaN . . . 39

2.3.1 ZnO Growth by Ion Beam Sputtering 41

2.3.2 The Importance of Au in Ni/Au Contact 54

2.3.3 Ni/Au/ZnO Contact for p-GaN 57

2.4 Summary 60

References **62**

3 ICP Etching of III-Nitrides **67**

3.1 Introduction 67

3.2 The ICP Etcher 68

3.3 Basic Plasma Physics 69

3.3.1 Collisions of Particles in Plasma 69

3.3.2 Motion of Single Charged Particles 72

3.3.3 Electron and Ion Temperature 74

3.3.4 Plasma Potential 74

3.3.5 Sheath Formation 75
3.3.6 Development of DC Bias of RF Electrodes 75
3.3.7 Etch Chemistry of Group III-Nitrides 77
3.3.8 Redeposition of Etch Products 79
3.4 ICP Etching Parameters 81
3.4.1 RF Power 81
3.4.2 ICP Power 81
3.4.3 Chamber Pressure 82
3.5 ICP Etching for III-Nitrides LED 83
3.5.1 Taguchi Method 83
3.5.2 Experiment 84
3.5.3 Results and Discussion 86
3.6 Damage Induced by SiO_2 Sputter Deposition 98
3.6.1 Basics of Ion Beam Sputtering 99
3.6.2 Photoluminescence 102
3.6.3 Experiment 103
3.6.4 Results and Discussion 105
3.7 Summary 110

References **113**

4 GaN Nanotube Formation and Application **117**

4.1 Introduction 117

4.2 Dislocations in GaN 120

4.3 Piezoelectric Effect in Dislocations of GaN 122

4.4 GaN Nanotube Formation 123

4.4.1 Experiment 124

4.4.2 Results and Discussion 124

4.5 Characterisation of Field Emission from GaN Nanotubes 133

4.5.1 Introduction 133

4.5.2 Basics of Field Emission 135

4.5.3 The Fowler-Nordheim Plot 137

4.5.4 Experiment 137

4.5.5 Results and Discussion 138

4.6 Summary 140

References **145**

5 High Efficiency GaN-based Light Emitting Diodes **148**

5.1 Introduction 148

5.2 LED Operational Theory 149

5.2.1 Internal Radiation 152

5.2.2 Light Extraction from LED Structures 152

5.3 Current Spreading for LEDs 155

5.4 Current Spreading Simulation for GaN LED 160

5.5 Design of High Efficiency GaN-based LEDs 166

5.6 Experiment 168

5.7 Results and Discussion 169

5.8 Summary 172

References **174**

6 Conclusions and Future Work **176**

6.1 Conclusions 176

6.2 Suggestions for Future Work 178

List of Figures

1.1 Relative eye sensitivity and efficacy measured in lumens per Watt of optical power. 3

1.2 The various ternary and quaternary materials used for LEDs. . . 4

1.3 The publication trends for GaN related research. 5

1.4 The publication trend for studies of GaN contacts. 6

1.5 The publication trend for GaN etching. 8

1.6 The publication trend for nanotube field emission. 9

2.1 Energy-band diagrams for metal - n-type semiconductor contact and metal - p-type semiconductor contact. 16

2.2 Rectangular TLM and circular TLM patterns for contact resistance measurement. 22

2.3 Plot used to obtain specific contact resistance. 22

2.4 Band diagram of a metal in contact with n-GaN. 24

2.5 Work function of commonly used metals. 24

2.6 Microstructure of a Ti contact on n-GaN. 25

2.7 Band diagram of a metal contact with p-GaN. 27

2.8 TEM picture of the annealed Ni/Au/p-GaN film. 29

2.9 Illustration of the reflection. 33

2.10 Illustration of the interference. 35

2.11 Setup for the simulation of light transmittance. 36

2.12 Simulated light transmittance of a thin Ni and Au film. 38

2.13 AFM image of the as-grown Ni, as-grown Ni/Au and annealed Ni/Au film. 40

2.14 Zn content measured by WDX for a ZnO film grown at different O_2 flow rates and substrate temperatures. 46

2.15 XRD spectra of ZnO film grown at different O_2 flow rates. 47

2.16 XRD for Substrate temperature effect. 48

2.17 FWHM as a function of substrate temperature and O_2 flow rate. 50

2.18 TEM pictures for the ZnO film. 50

2.19 Diffraction pattern of the ZnO films. 51

2.20 Effect of O_2 flow rate and substrate temperature on ZnO. 52

2.21 O_2 flow rate effect on the light transmittance of the ZnO film. . . 53

2.22 The structure of samples used in the study of the importance of Au in Ni/Au contacts. 55

2.23 AFM images for annealed Ni film and Au film deposited on this annealed Ni film. 56

2.24 SEM picture of the annealed Ni/Au/ZnO film. 58

2.25 Experimental and simulated light transmittance of Ni/Au and Ni/Au/ZnO. 60

3.1 Schematic of an ICP etching unit. 69

3.2 Schematic of a space charge sheath developed in front of a floating substrate. 76

3.3 Illustration of electrical forces acting on a negative-charged particle. 80

3.4 Schematic of the LED structure. 85

3.5 Effect plot of etch parameter versus DC bias. 87

3.6 Effect plot of etch parameter versus etch rate. 88

3.7 XRD spectrum of the GaN LED etched using the conditions listed in Table 3.5 for 5 minutes. The XRD peak (1), (2) and (3) are identified as beta gallium chloride (0 3 2), (2 1 $\bar{3}$) and (3 1 2), respectively. 89

3.8 Effect plot of etch parameter versus sidewall angle. 91

3.9 SEM images of sidewall profile of etched GaN. 92

3.10 Effect plot of etch parameter versus surface roughness. 93

3.11 SEM image of sidewall profile of the sample etched by optimised conditions. 96

3.12 SEM image of etched bulk GaN. 97

3.13 Schematic of an ion beam source and the potential distribution in the direction of ion injection. 101

3.14 Structure of InGaN MQW. 103

3.15 Schematic of Nordiko dual ion beam system. 104

3.16 Effect plot of sputtering parameters for SiO_2 deposition rate. . . 107

3.17 Effect plot of sputtering parameters versus PL intensity decrease. 109

4.1 TEM picture for a single-wall and multi-wall CNT. 119

4.2 SEM pictures of whiskers produced by selective etching of dislocations. 121

4.3 TEM pictures for a screw dislocation and mixed dislocation. . . . 121

4.4 Illustration of a screw dislocation. 123

4.5 SEM picture of a GaN nanotube. 125

4.6 TEM picture of a GaN nanotube. 126

4.7 AFM images for the 3.8μm-thick GaN film etched for different times. 128

4.8 X-ray diffraction pattern of a GaN nanotube. 129

4.9 Formation mechanism of GaN nanotubes. 131

4.10 SEM image of GaN nanotubes protruding from the GaN film, aligned along the $(10\bar{1}0)$ scratch direction. 132

4.11 SEM images for a GaN pyramid array. 134

4.12 Schematic of an energy diagram for a metal–vacuum interface. Note that the barrier height (ϕ) for the electrons of kinetic energy E_e is $\phi = \phi_m + \mu - E_e$. 135

4.13 Schematic for the field emission measurement. 142

4.14 AFM image of the surface morphology for as-grown n-GaN. . . . 142

4.15 SEM image of the n-GaN nanotubes. 143

4.16 Field emission I-V characteristics of as-grown n-GaN and n-GaN nanotubes. 143

4.17 Field emission from the vicinity of the conduction band of a semiconductor. 144

4.18 Fowler-Nordheim plot for as-grown GaN and GaN nano-tubes. . 144

5.1 Carrier distribution across a p-n junction. 150

5.2 Illustration of the recombination of carriers in a semiconductor. . 151

5.3 Light emission power vs. injection current for a GaN-based LED [14]. Note the near-linear characteristic for the injection current between 20 and 70 mA. 153

5.4 Illustration of a distributed Bragg reflector (DBR) coated in the backside of a LED structure. 154

5.5 Illustration of geometric effect on the light propagation inside the semiconductor. 155

5.6 Illustration of the current spreading for a conductive-substrate type LED. 156

5.7 Illustration of the current spreading for a LED with a insulating substrate. 156

5.8 The possible current paths from the p-type to n-type ohmic contact for a GaN LED. 158

5.9 The contact pad for a commercial and modified LED. 158

5.10 The equivalent circuit for a GaN LED with a Ni/Au/ZnO contact. 160

5.11 The equivalent circuit used in the simulation for the GaN LED with a Ni/Au/ZnO contact. 162

5.12 The equivalent circuit used in the simulation for the GaN LED with a Ni/Au contact. 163

5.13 The equivalent circuit used in the simulation for the GaN LED with a highly conductive contact. 163

5.14 The simulated current distribution for the rectangular GaN-based LEDs with the width 100 μm and the lengths (a) 70 μm, (b) 150 μm, (c) 230 μm, (d) 480 μm, and (e) 1000 μm. 165

5.15 Energy band diagram of the charge asymmetric resonance tunnelling LED structure. 167

5.16 The structure detail of the LED. 169

5.17 I-V characteristic of the LED with a Ni/Au and Ni/Au/ZnO contact. 170

5.18 The electroluminescence of a circular LED with a radius of 1mm, 480μm, and 230μm at an injected current of 30mA. 171

List of Tables

1.1 Comparison of light bulbs and light emitting diodes. 2

1.2 Published configuration of p-GaN ohmic contacts. 7

2.1 Optical properties of Ni [66], Au [66], GaN [20, 21] and ZnO [22]. 37

2.2 ZnO growth condition for the Ni/Au/ZnO electrode. 58

3.1 The physical properties of possible etch products of AlN, GaN and InN reacting with F, Cl, Br and I radicals. 78

3.2 Parameters and levels used in the ICP etching study. 85

3.3 Experimental matrix for the investigation of ICP etching for GaN. 85

3.4 The relative effect table of ICP etching parameters on etch rate, sidewall angle, DC bias and Surface roughness. 95

3.5 The optimised conditions for the GaN LED structure. 95

3.6 The weighted effect table of ICP etching parameters on etch rate, sidewall angle, and surface roughness. 96

3.7 Parameters and levels used in the study of the damage induced by SiO_2 deposition. 104

3.8 Experimental matrix of the SiO_2 ion beam sputtering deposition tests, according to the Taguchi experimental method. 105

3.9 The relative effect table of sputtering parameters on SiO_2 deposition rate and the decrease of PL intensity. 109

3.10 The sputtering parameters of optimised condition for low damage induced by SiO_2 ion beam sputtering deposition. 110

3.11 The weighted effect table of sputtering parameters on SiO_2 deposition rate and the decrease of PL intensity. 110

4.1 Comparison of properties of GaN and CNTs 119

5.1 List of components used in the current spreading simulation. . . . 161

5.2 List of values used in the current spreading simulation. 161

5.3 Integrated current over location and the percentage of the integrated current of Ni/Au/ZnO contact. 166

List of Abbreviations

Abbreviations	Description
AFM	Atomic Force Microscopy
CNT	Carbon Nanotube
CTLM	Circular Transmission Line Method
DBR	Distributed Bragg Reflector
ECR	Electron Cyclotron Resonance
EDX	Energy Dispersive X-ray Spectrometry
F-N	Fowler-Nordheim
FWHM	Full-Width at Half Maximum
ICP	Inductively Coupled Plasma
I-V	Current-Voltage
LCD	Liquid Crystal Display
LD	Laser Diode
MOCVD	Metal-Organic Chemical Vapour Deposition
MQW	Multiple Quantum Well
MWNT	Multi-Wall Nanotube
OA	Orthogonal array
PL	Photoluminescence
RF	Radio Frequency
RIE	Reactive Ion Etching
RTA	Rapid Thermal Annealing
SEM	Scanning Electron Microscopy
SWNT	Single-Wall Nanotube
TEM	Transmission Electron Microscopy
TLM	Transmission Line Method
WDX	Wavelength Dispersive X-ray Spectrometry
XRD	X-ray Diffractometry

List of Symbols

Symbol	Description	Unit
A_{grid}	Grid area	m^2
A_{sub}	Substrate area	m^2
A, A_a, A_b	Area	m^2
a, b	constant	
$\mathbf{B}$	Magnetic field	weber/m^2
$\mathbf{b}$, b_s	Burger vector	m
c	Speed of light	m/sec
$\mathbf{D}$	Electric displacement	C/m^2
D_g	Grain size	nm
D	Density of material	kg/m^3
d, d_a, d_b	Gap between anode and cathode	m
e_{15}, e_{31}, e_{33}	Piezoelectric stress constant	
E_{Fn}	Fermi energy of n-type semiconductor	eV
E_{Fp}	Fermi energy of p-type semiconductor	eV
E_{ion}	Ion energy	eV
E_{rad}	Energy of total radiative recombination	eV
E_c	Bottom of conduction band	eV
E_e	Kinetic energy of electrons	eV
E_F	Fermi energy level	eV
E_g	Energy bandgap	eV
E_k	Kinetic energy	J
E_t	Trap energy level	eV
E_v	Top of valence band	eV
$\mathbf{E}$, E_x, E_y, E_z	Electric field	V/m
$\mathbf{E}_{DC}$	Electric field in an ICP system	V/m
f	Frequency	Hz
F	Applied field for field emission	V/m
$\mathbf{F}_{net}$	Net force acting on a particle	N
h	Planck constant	J-s
$\hbar$	Reduced Planck constant	J-s
$\mathbf{H}$	Magnetic intensity	A/m
i	Current	A
I_0, I_1, K_0, K_1	Modified Bessel functions of the first and second kind	
J	Current density	A/cm^2
k	Extinction coefficient	
k_B	Boltzmann constant	J/K

Symbol	Description	Unit
L_T, L'_T	Transmission length	m
L, l	Distance	m
$\mathbf{m}$	Integer	
M, m, m_1, m_2	Mass	kg
m^*	Effective mass	kg
N	Complex refractive index	
n	Refractive index	
N_i	number density	cm^{-3}
N_{ion}	Number of ions	
N_{mat}	Number of particles	
N_{rad}	Number of radiative recombination	
$N_{non-rad}$	Number of non-radiative recombination	
N_D	Donor impurity density	cm^{-3}
n_i	Carrier concentration of n-type semiconductor	cm^{-3}
N_t	Trap density	cm^{-3}
P_{PL}	Photoluminescence intensity	W
P_{rad}	Power of single radiative recombination	W
p_i	Carrier concentration of p-type semiconductor	cm^{-3}
$\mathbf{P}_s$	Polarisation	C/m^2
q	Magnitude of electronic charge	C
Q	Collision cross section	m^2
R	Resistance	Ω
r	radius	m
R_{dep}	Deposition rate	nm/hr
R_c	Contact resistance	Ω
R_s	Sheet resistance	$\Omega/\square$
S_s	Strain	
T	Temperature	K
t	Time	second
t_t, t_p, t_n, $t_{Ni/Au}$, t_{ZnO}	Thickness	m
U	Recombination rate	cm^{-3}/s
U_{rad}	Radiative recombination rate	cm^{-3}/s
U_0	Surface binding energy	eV

Symbol	Description	Unit
u_x, u_z, u_{sx}, u_{sy}, u_{sz}	displacement of dislocation	nm
V	Voltage	V
v	Velocity	m/sec
V_{acc}	Accelerator grid voltage	V
v_{th}	Carrier thermal velocity	cm/s
V_a	Applied voltage	V
V_f	Floating potential	V
V_j	Voltage drop across a p-n junction	V
V_p	Plasma potential	V
V_s	Screen grid voltage	V
V_T	Total voltage drop	V
v_x^0, v_y^0, v_z^0	Initial speed	m/sec
v, v_x, v_y, v_z	speed	m/sec
W	Width	m
Z	Length	m
β, β_a, β_b	Field enhancement factor	
$\Delta\Phi$	Image force barrier lowering	V
η	Fraction of particles deposited on the substrate	
λ	Wavelength	nm
μ	Fermi energy of metal	eV
μ_0	Permeability in vacuum	H/m
μ_r	Relative Permeability	H/m
∇	Differential operator	
ν	Collision frequency	Hz
ω	Angular frequency	Hz
ϕ	Barrier height	eV
Φ_{Bn}	Schottky barrier height on n-type semiconductor	V
Φ_{Bp}	Schottky barrier height on p-type semiconductor	V
ϕ_m	Metal work function	V
ϕ_s	Semiconductor work function	V
ρ	Electric free charge density	C/cm^3

Symbol	Description	Unit
ρ_t, ρ_n, ρ_p, $\rho_{Ni/Au/ZnO}$, $\rho_{Ni/Au/ZnO}$, $\rho_{Ni/Au}$	Resistivity	Ω·cm
σ	Conductivity	Ω/m
ΣF_{ion}	Total ion drag force	N
$\Sigma F_{neutral}$	Total neutral particle drag force	N
θ_c	Critical angle	degree
θ_i	Incident angle	degree
θ_t	Exit angle	degree
ε_0	Permittivity in vacuum	F/m
ε_r	Relative permittivity	F/m
ζ	Intercept in the Fowler-Nordheim plot	
χ	electron affinity	eV
Φ_0	Energy level at surface	V
ρ_c, $\rho_{ZnO-Ni/Au}$	Specific contact resistance	$\Omega\cdot$ cm^2

Chapter 1

Introduction

1.1 Lighting – A Historical Perspective

Flames produced by combustion of oils, and later gas, had been used as artificial lighting sources until T. Edison first demonstrated light bulbs in 1879. The current flowing through to the filament of a light bulb generates heat to emit light, but the efficiency is very low. Thus, seeking a lighting source which has high light emission efficiency and low power consumption has been at the core of research into light emitting devices. In 1907, H. J. Round discovered electro-luminescence by driving a current through a metal contact into a carborundum crystal [1]. There was little progress until Pankove *et al.* [2] first reported efficient electro-luminescence from GaAs in 1962. Since then, considerable effort has devoted this type of lighting source.

There are many advantages to light emitting diodes in comparison with conventional lighting devices. Table 1.1 shows the comparison of light bulbs and light emitting diodes for application in traffic lights and railway signals [3]. It is clear that light emitting diodes have lower power consumption and $\sim$ 10 times longer lifetime. The most interesting property of light emitting diodes is that the emitted colour is direct from the source, but that light bulbs have to use colour filters to generate the required colour, such that the energy of the non-required colour

	Power Consumption			Lifetime	Failure Mode	Visibility
	Red	Yellow	Green			
Light Bulbs	70W	70W	70W	6-12 months	Sudden total failure	Uses colour filter
LED	18W	25W	35W	5-10 years	Gradual intensity decrease	Direct

TABLE 1.1: Comparison of light bulbs and light emitting diodes for application in traffic lights and railway signals [3].

is wasted. These properties of light emitting diodes have been utilised to many applications.

GaAs-based light emitting devices have been successfully demonstrated over the red light range with high efficiency and low power consumption. Many researchers are seeking suitable semiconductors which can emit light in the range from green to blue and UV. Figure 1.1 illustrates human eye sensitivity and efficacy for colours [47]. The eye sensitivity reaches a peak at a wavelength of 555nm and decays to only 10% in the blue light region. This implies that the light emitting devices in the blue light region have to be more efficient than green and yellow light. ZnSe, ZnO, and GaN are potential semiconductor materials which have a direct bandgap of 3.3eV, 2.7eV and 3.45 eV, respectively. The first electronically pumped ZnSe-based blue laser was achieved by Haase *et al.* in 1991 [33]. However, the high series resistance originating in the ohmic contacts limits the device performance and lifetime, and effective solutions are still absent. ZnO is the other alternative material, but the fabrication of p-ZnO has only just been realised in 1999 [34]. The research for ZnO light emitting devices are ongoing. In contrast, GaN has been processed as high quality single crystal and p-GaN has been available since 1990 [7, 8]. Extensive research has been undertaken on the improvement of GaN growth, and the associated processing techniques. The techniques developed provide effective solutions for the applications of group III-nitrides. This has resulted in group III-nitrides being the dominant materials for the light emitting devices in the UV and blue ranges.

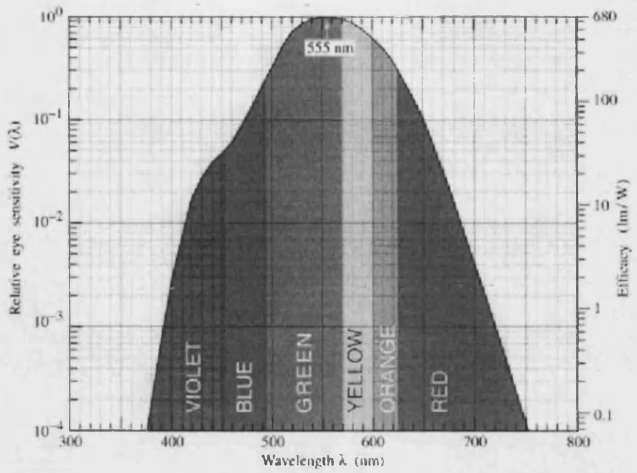

FIGURE 1.1: Relative eye sensitivity (left axis) and efficacy measured in Lumens per Watt of optical power (right axis).

1.2 Development of Group III-Nitrides

Since the 1990s, group III-nitrides have been utilised to fabricate various electronic devices due to their excellent electrical and physical properties. The wide and direct bandgaps, 3.4 eV for GaN, 6.2 eV for AlN and 1.9 eV for InN, make them promising candidates for short wavelength light emitting diodes (LEDs) and laser diodes (LDs) in the blue to ultraviolet region [3]. A LED-based full colour display has been demonstrated since blue LEDs were introduced (Figure 1.2) [4]. White LEDs with high brightness have also been developed by luminescence conversion [5]. These white light sources not only provide long lifetime devices, but also have much lower power consumption compared with incandescent or fluorescent light sources. Short wavelength LDs are the key components required by high density optical storage technologies. Nakamura *et al.* [6] have demonstrated InGaN/GaN/AlGaN-based laser diodes with a wavelength as short as 417 nm and a lifetime estimated at ~10,000 hours, indicating the suitability of the group III-nitrides LDs for high density optical storage applications.

Figure 1.3 demonstrates the publication trend of GaN related researches from 1981 to 2002. These data, taken from the database of *ISI Web of Science Service*, is obtained using the search "GaN". It can be seen that the number of publications starts to increase in 1990 and has grown dramatically since 1995. The increase is

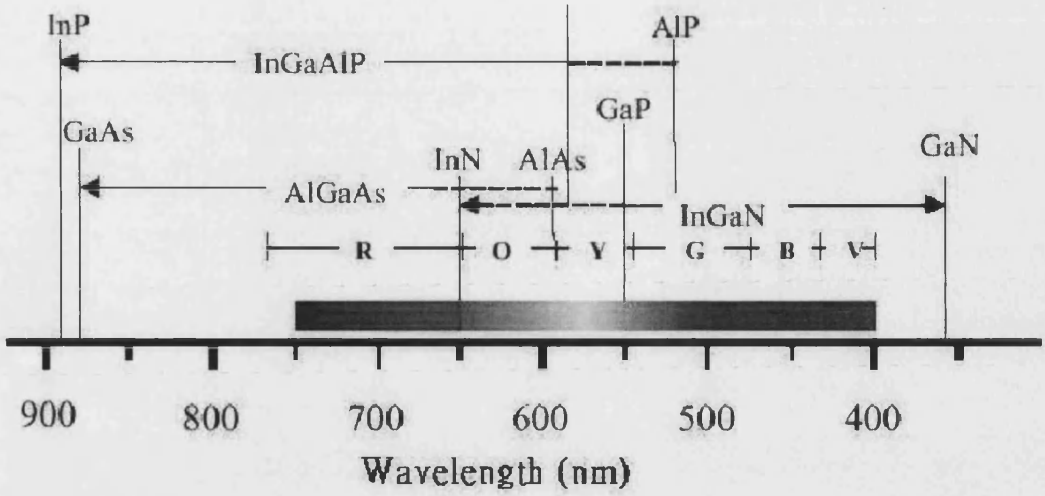

FIGURE 1.2: The various ternary and quaternary materials used for LEDs with the wavelength ranges indicated [4].

mainly due to the successful growth of high quality GaN single crystal epilayers and the availability of highly conductive p-GaN. The GaN epilayer is normally grown on a sapphire substrate but the dislocation density of the films is too high due to the thermal and lattice mismatch between GaN and sapphire. In 1986, Amano *et al.* [7] developed a technique which uses an AlN buffer layer between the sapphire substrate and GaN, and the quality of the GaN epilayer was significantly improved. This technique has allowed the application of group III-nitrides. A highly conductive p-GaN was successfully grown in 1989 by the same group. Amano *et al.* [8] used low energy electron beam irradiation to activate the carriers in the p-GaN and found the resistivity was 35 Ω·cm. This success has promoted the applications of group III-nitrides to light emitting devices in the colour range of blue and ultraviolet [9]. Subsequently, considerable efforts have been made in the investigation of group III-nitrides.

Because the GaN crystal quality and p-GaN conductivity have been improved, the processing and design of GaN optoelectronic devices become the topical issues. The main processes for group III-nitride devices are ohmic contact formation, dry or wet etching and thin film coating. Ohmic contacts act as electrodes for current injection, dry or wet etching is used for patterning the devices, and thin film coating is for metal layer deposition of ohmic contacts or etching mask fabrication. The design conditions for GaN-based optoelectronic devices includes

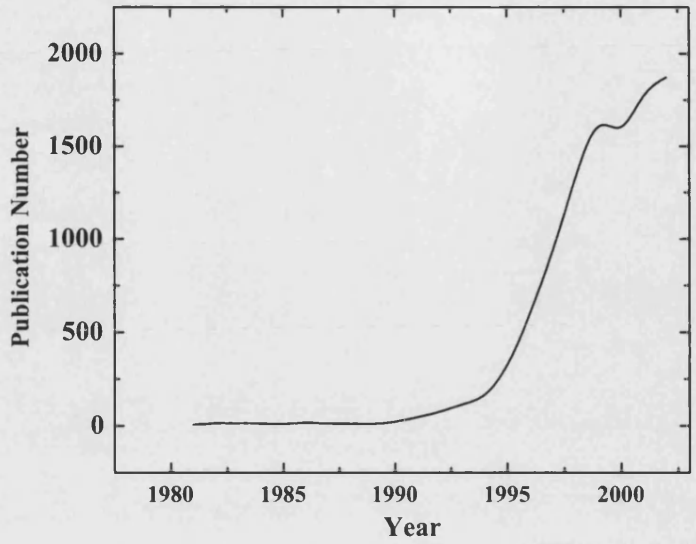

FIGURE 1.3: The publication trends for GaN related research from 1981 to 2002.

current spreading and light extraction. Hence, the device design and processing technology can strongly affect the device performance. Consequently, a study of these issues is essential.

1.3 Development of Processing and Device Design for Group III-Nitrides

1.3.1 Ohmic Contacts for Group III-Nitrides

The research into ohmic contacts for GaN are mainly concerned with exploring different metallisation, annealing condition effects, and surface cleaning and modification. Figure 1.4 shows the publication trend for studies of GaN contacts. It is seen that the number of publications has increased steadily since 1994. This is consistent with the progress of GaN crystal quality and the availability of p-GaN.

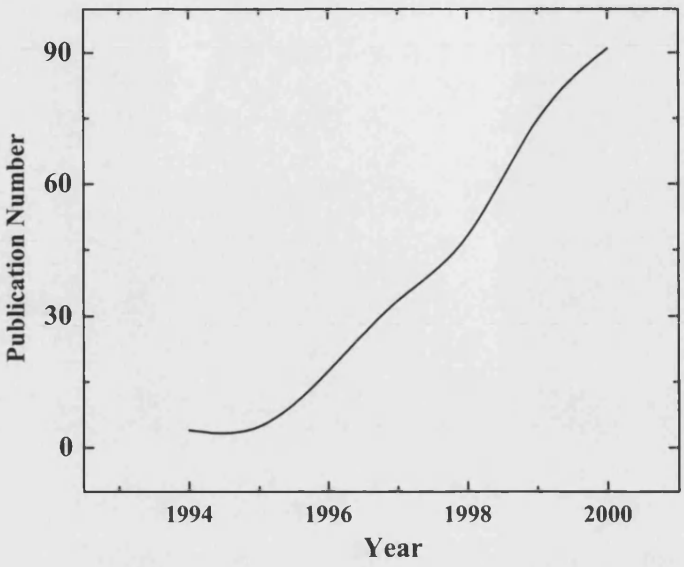

FIGURE 1.4: The publication trend of studies of GaN contacts from 1994 to 2000.

For n-GaN contacts, Lin *et al.* [10] have achieved a low specific contact resistance 8×10^{-6} $\Omega\cdot cm^2$ using a Ti/Al contact which is annealed at 900 ^oC in N_2 for 30 seconds. Different metals, Al [12], W [13], Cr/Al [14], and ZrN/Zr [15], were found to produce ohmic characteristics and contact resistances in the range of 10^{-4} to 10^{-6} $\Omega\cdot cm^2$. Surface modification by Si implantation has been reported and a very low specific contact resistance 3.6×10^{-8} $\Omega\cdot cm^2$ has been obtained [36]. The reports indicate the existence of fewer problems in achieving low specific contact resistance for contact to n-type GaN.

In contrast, ohmic contacts to p-GaN have been an important issue because the low carrier concentration and high work function of p-GaN [35]. Table 1.2 shows the published processing information on p-GaN ohmic contacts. It is seen that Ni-based and Pt-based contacts have low specific contact resistance. In practice, Ni-based contacts are the most commonly used metallisation for p-GaN because Ni is relatively abundant and cheap. The specific contact resistance is in the range of 10^{-2} to 10^{-3} $\Omega\cdot cm^2$. Many reports show that the surface cleaning and modification by chemicals results in high sensitivity to the p-GaN ohmic contacts [19, 27, 28, 29, 30, 26]. The other consideration especially for surface

Contact	Specific contact resistance (Ω·cm^2)	Annealing Conditions	Ref.
Ni/Au=100/100nm	1.2×10^{-2}	750 °C, 1 min, N_2	[16]
Ni/In=100/100nm	8.9×10^{-3}	800°C, 1 min, N_2	[17]
Ni/Pd/Au=20/20/100nm	1×10^{-4}	550°C, 5 min, O_2	[18]
Ni/Mg/Ni/Si=25/8/25/240nm	1×10^{-3}	350°C, 30 min, N_2	[19]
Pt/Ni/Au=20/30/80nm	5.1×10^{-4}	350°C, 1 min, ambient NA	[20]
Pt=25 nm	3.0×10^{-5}	As grown, $(NH_4)_xS$ treated	[21]
Pd/Au=20/500nm	4.3×10^{-4}	As-grown, Aqua regia treated	[22]
Ta/Ti=60/40nm	7×10^{-5}	800°C, 20 min, vacuum	[23]
p-GaAs(C-doped)=200nm	7×10^{-3}	800°C, time & ambient NA	[24]
Ti/Pt/Au/InGaN=15/50/80nm	4.6×10^{-4}	300°C, 5 min	[25]
Ni/p-$Al_xGa_{1-x}N$	9.3×10^{-4}	400°C, 5 min, ambient NA	[26]

TABLE 1.2: Published configuration of p-GaN ohmic contacts.

light emitting devices is the requirement for transparent p-GaN ohmic contacts because the contacts act as an obstruction to the emitted light. There are only a few published studies referring to this issue [31, 32].

1.3.2 Etching for Group III-Nitrides

Etching processes have been used to transfer patterns onto a target material since the 16^{th} century [48]. This involves the use of etchants for the target materials and masking materials which can resist the etchants. Over the last few decades, this process was found to be very effective to pattern semiconductor devices. The etching for group III-nitrides is particularly difficult because of their high bonding energy, 7.72 eV for InN, 8.92 eV for GaN, and 11.52 eV for AlN. Figure 1.5 shows the publication trend of GaN etching from 1994 to 2000. This trend is consistent with the development of GaN-based devices. In the early stage of research for GaN etching, different etching methods, *i.e.* reactive ion etching (RIE) [36], electron cyclotron resonance (ECR) etching [37], and wet etching [38, 39], were studied and found that the wet etching gave a very low etch rate and that ECR etching was more effective to pattern group III-nitrides but the etch rate of GaN was only in the range of 700 Å/min. In 1996, Shul *et al.* [40] first reported

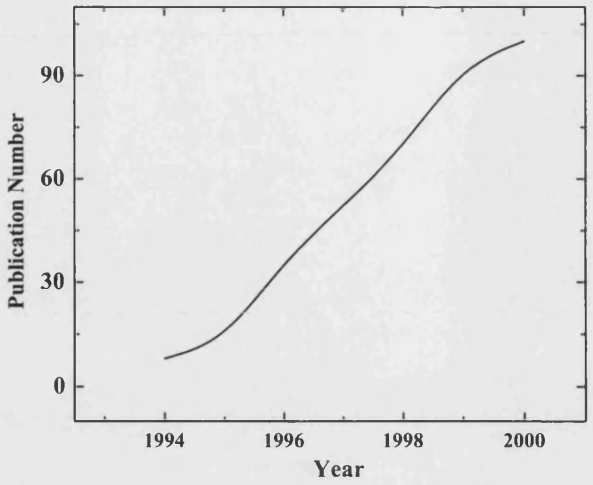

FIGURE 1.5: The publication trend for GaN etching from 1994 to 2000.

inductively coupled plasma (ICP) etching of GaN and an etch rate as high as 6875 Å/min. Since then, ICP etching has been the predominant etching method for patterning GaN-related materials.

1.3.3 Field Emission from Group III-Nitrides

Electron sources have become increasingly important in research and everyday life. Cold cathode emitters made of semiconductors are of interest because they can be fabricated on small dimensions and precise locations by semiconductor processing. They have shown great potential for numerous applications.

Nanotubes are very attractive for cold cathode emitters because of their high localised field enhancement effect. Figure 1.6 shows the publication trend of nanotube field emission. It is seen that the publication quantity starts to increase from 1995 and then draws a lot of attention since then. In 1995, carbon nanotubes were found to have a very low turn on field and high current density emission [41, 42]. In 1999, a fully sealed field-emission display 4.5 inch in size was demonstrated using single-wall carbon nanotube-organic binders [43].

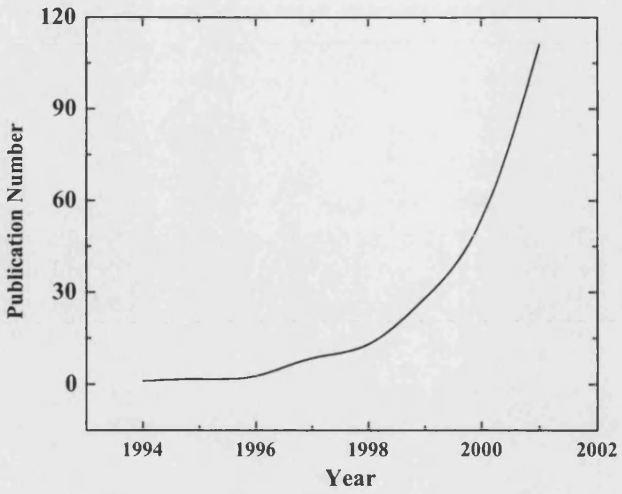

FIGURE 1.6: The publication trend for nanotube field emission from 1994 to 2001.

Group III-nitrides can be used as cold cathode emitters because of their low electron affinities [35]. The research has been focused on the field emission characteristics of GaN and AlGaN and into developing processing techniques to lower the turn on electric field [44, 45, 46]. The results show that they are potential materials for cold cathode electron emitters.

1.4 Aims and Objectives

This thesis is focused on the development of group III-nitrides processing techniques and associated optoelectronic devices. Emphasis on the process development has been placed on transparent ohmic contacts for p-GaN and ICP etching. The published research into transparent ohmic contacts for p-GaN is not extensive but such interfaces are very important for surface light emitting devices. ICP etching of group III-nitrides has been widely studied but the research is fragmented. An experimental design process will be introduced to integrate the results of etch rate, DC bias, etched sidewall angle and surface roughness. The design of group III-nitrides is focused on cold cathode electron emitters and surface

light emitting diodes.

Chapter 2 investigates the transparency mechanism for Ni/Au contacts on p-GaN. This has resulted in the development of one novel contact, Ni/Au/ZnO, for p-GaN to increase the light transmittance at certain wavelength. A ZnO growth technique which involves an ion beam sputtering system and Zn metallic target has also been developed. The aim of this growth technique is to fabricate a highly conductive ZnO film with a high light transmittance.

Chapter 3 reports on the effect of ICP etching parameters on GaN. The etch rate, DC bias, sidewall angle and surface roughness are discussed. The influence of SiO_2 deposition by ion beam sputtering has been also investigated. A minimum photoluminescence loss is the objective to be achieved in this study.

Chapter 4 develops a novel method for the formation of GaN nanotubes. These nanotubes are characterised by TEM, SEM, XRD, WDX, and AFM. One possible application, a cold cathode electron emitter, is explored. A low turn on electric field is expected because of the small dimensions of the GaN nanotubes.

Chapter 5 applies the developments made in chapter 2 and 3 into a light emitting device. Current spreading for large light emitting diodes has also been investigated.

Chapter 6 offers a conclusion and the outlook of the future research prospects in this exciting field.

References

[1] H. J. Round, *Electrical World* **49**, 309 (1907).

[2] J. I. Pankove, and J. E. Berkeyheiser, *Proc. IRE.* **50**, 1976 (1962).

[3] S. Nakamura and G. Fasol, *The Blue Laser Diode*(Springer, New York, 1997).

[4] S. J. Pearton, F. Ren, A. P. Zhang, and K. P. Lee, *Mat. Sci. & Eng.* **R59**, 55 (2000).

[5] P. Schlotter, J. Baur, Ch. Hielscher, M. Obloh, R. Schmidt, and J. Schneider, *Materials Science & Engineering B* **59**, 390 (1999).

[6] S. Nakamura, M. Senoh, S. Nagahama, N. Iwasa, T. Yamada, T. Matsushita, H. Kiyoku, Y. Sugimoto, T. Kozaki, H. Umemoto, M. Sano, and K. Chocho, *Jpn. J. Appl. Phys. Pt. 2* **36**, L1568 (1997).

[7] H. Amano, N. Sawaki, I. Akasaki, and Y. Toyoda, *Appl. Phys. Lett.* **76**, 529 (1999).

[8] H. Amano, M. Kito, K. Hiramatsu, and I. Akasaki, *Jpn. J. Appl. Phys. Pt2.* **28**, L2112 (1989).

[9] H. Amano, and I. Akasaki, *Solid State Phys.* **25**, 399 (1990).

[10] M. E. Lin, Z. Ma, F. Y. Huang, Z. F. Fan, L. H. Allen, H. Morkoç, *Appl. Phys. Lett.* **48**, 353 (1986).

[11] B. P. Luther, S. E. Mohney, and T. N. Jackson, *Semicon. Sci. Tech.* **13**, 1322 (1998).

[12] B. P. Luther, S. E. Mohney, T. N. Jackson, M. Asif Khan, Q. Chen, and J. W. Yang, *Appl. Phys. Lett.* **70**, 57 (1997).

[13] W. Gladfelter, J. M. Van Hove, J. N. Kuznia, M. A. Khan, A. Franciosi, F. Ren, C. R. Abernathy, S. N. G. Chu, J. R. Lothian, and S. J. Pearton, *Appl. Phys. Lett.* **66**, 1503 (1995).

[14] N. A. Papanicolaou, A. Edwards, N. V. Rao, J. A. Mittereder, and W. T. Anderson, *Mater. Sci. Form.* **264-2**, 1407(1998).

[15] S. D. Wolter, B. P. Luther, S. E. Mohney, R. F. Karlicek, and R. S. Kern, *Electrochem. Solid St.* **2**, 151(1999).

[16] L. Sugiura, M. Suzuki, and H. Nishio, *Appl. Phys. Lett.* **72**, 1748 (1998).

[17] J. Chevallier, *Mat. Sci. & Eng. B* **71**, 62 (2000).

[18] P. H. Holloway, T. J. Kim, J. T. Trexler, S. Miller, W. V. Lampert, and T. W. Haas, *Appl. Surf. Sci.* **117/118**, 362 (1997).

[19] H. Ishikawa, S. Kobayashi, Y. Koide, S. Yamasaki, S. Nagai, J. Umezaki, M. Koike, and M. Murakami, *J. Appl. Phys.* **81**, 1315 (1997).

[20] Y. Koide, H. Ishikawa, S. Kobayashi, S. Yamasaki, S. Nagai, J. Umezaki, M. Koike, and M. Murakami, *Appl. Surf. Sci.* **117/118**, 373 (1997).

[21] A. K. Fung, J. E. Borton, M. I. Nathan, J. M. van Hove, R. Hickman II, P. P. Chow, and A. M. Wowchak, *J. Electron. Mater.* **28**, 572 (1999).

[22] D. B. Ingerly, Y. A. Chang, and Y. Chen, *MRS Internet. J. Nitride Semicond. Res.* **4S1**, G6.49 (1999).

[23] C. F. Chu, C. C. Yu, Y. K. Wang, J. Y. tsai, F. I. Lai, and S. C. Wang, *Appl. Phys. Lett.* **77**, 3423 (2000).

[24] E. Kaminska, A. Pritrowsks, J. Jasinski, J. Kozubowski, A. Barcz, K. Golaszewska, D. B. Thomson, R. F. Davis, and M. D. Bremser, *MRS Internet. J. Nitride Semicond. Res.* **4S1**, G9.9 (1999).

[25] J. S. Jang, I. S. Chang, H. K. Kim, T. Y. Seong, S. Lee, and S. J. Park, *Appl. Phys. Lett.* **74**, 70 (1999).

[26] J. S. Jang, and T. Y. Seong, *Appl. Phys. Lett.* **76**, 2743 (2000).

[27] J. K. Kim, J. L. Lee, J. W. Lee, H. E. Shin, Y. J. Park, and T. Kim, *Appl. Phys. Lett.* **73**, 2953 (1998).

[28] J. L. Lee, J. K. Kim, J. W. Lee, Y. J. Park, and T. Kim, *Solid-State Electronics* **43**, 435 (1999).

[29] P. Sporken, C. Silien, F. Malengreau, K. Grigorov, R. Caudano, F. J. Sánchez, E. Calleja, E. Muñoz, B. Beaumont, and P. Gibart, *MRS Internet J. Nitride Semicond. Res.* **2**, 23(1997).

[30] B. Liu, M. H. Ahonen, and P. H. Holloway, *J. Vac. Sci. Technol. A* **18**, 1919 (2000).

[31] J. K. Sheu ,Y. K. Su, G. C. Chi, P. L. Koh, M. J. Jou, C. M. Chang, C. C. Liu, and W. C. Hung, *Appl. Phys. Lett.* **74**, 2340 (1999).

[32] D. W. Kim, Y. J. Sung, J. W. Park, and G. Y. Yeom, *Thin Solid Films* **398-399**, 87 (2001).

[33] M. A. Haase, J. Qiu, J. M. DePuydt, and H. Cheng, *Appl. Phys. Lett.* **59**, 1272 (1991).

[34] M. Joseph, H. Tabata, and T. Kawai, *Jpn. J. Appl. Phys.* **38**, L1205 (1999).

[35] C. I. Wu and A. Kahn, *Appl. Surf. Sci.* **162-163**, 250 (2000).

[36] I. Adesida, A. Mahahan, E. Andideh, M. Asif Khan, S. T. Olsen, and J. N. Kuznia, *Appl. Phys. Lett.* **63**, 2777 (1993).

[37] S. J. Pearton, C. R. Abernathy, F. Ren, J. R. Lothian, *Semicond. Sci. Technil.* **8**, 310 (1993).

[38] T. L. Chu, *J. Electrochem. Soc.* **119**, 1200 (1971).

[39] J. I. Pankove, *J. Electrochem. Soc.* **119**, 1118 (1972).

[40] R. J. Shul, G. B. McClellan, S. A. Casalnuovo, D. J. Rieger, S. J. Pearton, C. Constantine, C. Barratt, R. F. Karlicek, C. Tran, and M. Schurman, *Appl. Phys. Lett.* **69**, 1119 (1996).

[41] A. G. Rinzler, J. H. Hafner, P. Nicolaev, P. Lou, S. G. Kim, D. Tomanek, P. Nordlander, D. T. Colbert, R. E. Smalley, *Science* **269**, 1550 (1995).

[42] W. A. De Heer, A. Châtelain, D. Ugarte, *Science* **270**, 1179 (1995).

[43] W. B. Choi, D. S. Chung, J. H. Kang, H. Y. Kim, Y. W. Jin, I. T. Han, Y. H. Lee, J. E. Jung, N. S. Lee, G. S. Park, and J. M. Kim, *Appl. Phys. Lett.* **75**, 3129 (1999).

[44] T. Kozawa, T. Ohwaki, Y. Taga, and N. Sawaki, *Appl. Phys. Lett.* **75**, 3330 (1999).

[45] T. Sugino, T. Hori, C. Kimura, and T. Yamanoto, *Appl. Phys. Lett.* **78**, 3229 (2001).

[46] M. Kasu, and N. Kobayashi, *Appl. Phys. Lett.* **79**, 3642 (2001).

[47] S. M. Sze, *Physics of Semiconductor Devices* 2nd edition(Willey, Canada, 1981).

[48] L. M. Emanuel, *Etching and Etchings*(Sir Isaac Pitman & Sons, LTD., London, 1930).

Chapter 2

Transparent Ohmic Contact for p-GaN

2.1 Introduction

Ohmic contacts are used as interfaces between the current sources and semiconductors. Ideally, there is no current loss at this interface. However, a barrier is formed at the interface if there is a mismatch of work functions between the contact material and semiconductor. In order to form an ohmic contact, the barrier height which is the difference of the work function of contact materials and semiconductors has to be reduced, or the semiconductors are heavily doped so that the depletion layer becomes thinner and the carriers in the semiconductors can tunnel through the barrier; a combination of both can be used. The following two sections describe the theory of metal-semiconductor contacts and the measurement methods for the specific contact resistance.

Transparent ohmic contacts are of interest for surface light emitting devices. Conventional metal contacts are used as electrodes for current injection, but part of the emitted light can be reflected and absorbed by the metal electrodes and thus reduces the light extraction efficiency. Reducing the area of the electrodes can increase the light emission, but the current spreading may be worse, resulting

in a lower current injection to the active regions. In this chapter, a transparent Ni/Au/ZnO ohmic contact for p-GaN is proposed as a solution. Through the anti-reflection design, the light extraction efficiency can be increased to 15%.

2.1.1 Theory of Metal–Semiconductor Contacts

Energy Band Description for Metal–Semiconductor Contacts

The electrical properties of solid materials are a consequence of its electron band structure which is the arrangement of the outermost electron bands and the way in which they are filled with electrons. The band that contains the highest-energy, or valence, electrons is termed the valence band (E_v). The conduction band (E_c) is the next highest energy band which is virtually unoccupied by electrons under most circumstances. Another important concept for the energy band description is that of the Fermi level (E_F). It is the energy level in solids at which the probability of a state being occupied by an electron is equal to 0.5. The Fermi level of a semiconductor varies with the nature and concentration of impurities. For a metal, it is related to the density of conduction electrons. When a metal and a semiconductor, with no surface states, are brought into contact, the interface condition is changed because of thermal equilibrium. The electrons will flow from the high-energy side to the low-energy side and thus align the Fermi levels. Figure 2.1a shows the energy diagram for an ideal metal – n-type semiconductor contact. ϕ_m is the metal work function which is the energy difference between the vacuum level and the Fermi level; χ is the electron affinity measured from the bottom of the conduction band to the vacuum level. The barrier height $q\Phi_{Bn}$ is given by

$$q\Phi_{Bn} = q(\Phi_m - \chi) \tag{2.1}$$

For an ideal contact between a metal and a p-type semiconductor (Figure 2.1b), the barrier height $q\Phi_{Bp}$ is given by

$$q\Phi_{Bp} = E_g - q(\Phi_m - \chi) \tag{2.2}$$

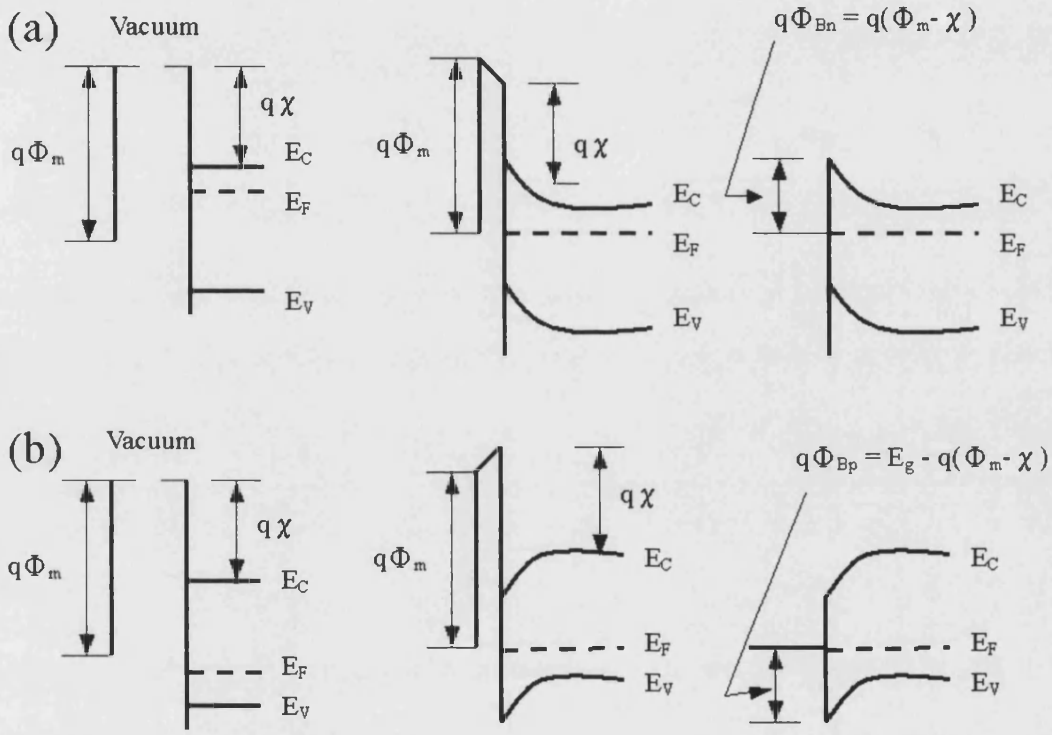

FIGURE 2.1: Illustration of the effect of the gap between a metal and (a) an n-type semiconductor, (b) a p-type semiconductor on the energy bands. Note that the Fermi level is aligned when the gap is very small (middle figure) or zero (left-hand side figure) due to thermal equilibrium.

Current Transportation Through Metal – Semiconductor Junctions

The current flow across metal–semiconductor junctions is dominated by majority carriers. Assuming that there are no defects at the interface of a metal–semiconductor contact, there are three current transport mechanisms involved in this metal–semiconductor system,

(1) thermionic emission of carriers across the barrier,
(2) diffusion of carriers from the semiconductor into the metal, and
(3) tunnelling through the barrier.

The thermionic emission theory postulates that only energetic carriers, those having an energy equal to or larger than the conduction band energy at the metal–semiconductor interface contribute to the current flow. The diffusion theory assumes that the driving force is diffusion of carriers due to the density gradient in the depletion layer. Tunnelling through the barrier takes into account the wave-nature of the electrons, allowing them to penetrate through thin barriers. In a given junction, it is possible to find a combination of all three mechanisms. However, practically we may discover that certain mechanisms dominate the current transportation.

Schottky Contacts

If a barrier exists between a metal and a semiconductor, the current density is proportional to a term $[\exp(\frac{qV_a}{k_BT} - 1)]$, where V_a is the applied voltage and k_B is the Boltzmann constant [2]. It indicates an asymmetric current – voltage characteristic of the contact. This type of metal – semiconductor contact is called a Schottky contact. Because of the current – voltage characteristic, it has been applied to many electronic devices such as the gate electrodes of a field-effect transistor.

The barrier height is varied by the presence of a surface state density. When the surface state density is very large, the barrier height is nearly independent of the

metal work function and is given by

$$q\Phi_{Bn} = (E_g - q\Phi_o) - q\Delta\Phi \tag{2.3}$$

where Φ_0 is the energy level at the surface and $\Delta\Phi$ is the image-force-induced lowering of the barrier which is dependent on the applied electric field on the solid. The origin of the image force can be described in terms of an image charge located on the other side of the barrier. This force will have the opposite sign compared with the force from the donor atoms. The overall effect is a strong electrostatic field towards the solid near the interface.

Take the Schottky effect into account and the barrier height is given by modifying Eq.2.1 and 2.2

$$q\Phi_{Bn} = q(\Phi_m - \chi) - q\Delta\Phi \tag{2.4}$$

$$q\Phi_{Bp} = E_g - q(\Phi_m - \chi) - q\Delta\Phi \tag{2.5}$$

Ohmic Contact

An ohmic contact is an electrode which has a very small contact resistance compared with the bulk or spreading resistance of the semiconductor. The ohmic contact resistance is defined as the ratio of the potential drop across the contact versus the current flowing through the contact and is independent of the applied voltages. A satisfactory ohmic contact should not significantly perturb device performance, and it is able to supply the required current with a voltage drop that is sufficiently small compared with the drop across the active region of the device. The specific contact resistance is expressed as

$$\rho_c = \left(\frac{\partial J}{\partial V}\right)^{-1}_{V=0} \tag{2.6}$$

where J and V is the current density and applied voltage, respectively.

For metal–semiconductor contacts with lower doping concentrations, the thermionic–emission current dominates the current transport. The specific contact resistance is given by [2]

$$\rho_c = \frac{k}{qA^*T} \exp\left(\frac{q\Phi_B}{k_BT}\right) \tag{2.7}$$

where Φ_B is the barrier height between metal and semiconductor, A^* is the effective Richardson constant for thermionic emission and given by $4\pi qm^*k^2/h^3$, where m^* is the effective mass of electron/hole for the semiconductor.

For contacts with a higher doping level, the tunnelling process will dominate and the specific contact resistance is given by [2]

$$\rho_c \approx exp\left[\frac{2\sqrt{\epsilon_s m^*}}{\hbar}\left(\frac{\Phi_B}{\sqrt{N_D}}\right)\right] \tag{2.8}$$

where ϵ_s and N_D is the semiconductor permittivity and donor impurity density, respectively.

It implies that in the tunnelling regime the specific contact resistance is dependent on doping concentration and varies exponentially with the factor $\left(\frac{\Phi_B}{\sqrt{N_D}}\right)$. According to Eq.2.2 and 2.8, it is found that high doping concentration and high metal work function can be used to obtain low specific contact resistance for a metal–p-type semiconductor system.

2.1.2 Measurement Methods of Specific Contact Resistance

The measurement of contact resistance is based on the transmission line method (TLM). The commonly used test pattern has either rectangular or circular geometry. The rectangular test pattern (Figure 2.3a) has width, W, length, Z, and

different spacing, d_i. The total resistance (R) between two contact pads becomes

$$R = 2R_c + d_i\frac{R_s}{Z} \tag{2.9}$$

where R_c and R_s is the contact resistance and sheet resistance, respectively. It is seen that the total resistance is linearly dependent on the slope $\frac{R_s}{Z}$ (Figure 2.3a). The intercept of d_i axis is $2L_T$, where $Z \cdot \frac{R_c}{R_s} \equiv L_T$. The specific contact resistance (R_s) is then given by

$$\rho_c = R_c \cdot Z \cdot L_t = R_s {L_T}^2 \tag{2.10}$$

In the rectangular TLM model, the current flow dispersion at the contact edge significantly affects the results of the contact resistance measurement [3]. It can be improved by use of the circular transmission line model (CTLM) [3, 4]. Figure 2.2b shows the pattern used in CTLM. The current flow through the contact and the voltage drop parallel to the interface are given by

$$\mathrm{d}i = \frac{V(2\pi r \cdot \mathrm{d}r)}{\rho_c} \tag{2.11}$$

$$\mathrm{d}V = \frac{R_s \cdot \mathrm{d}r \cdot i}{2\pi r} \tag{2.12}$$

where i is the current and V is the voltage. From these two equations one can obtain

$$\frac{\mathrm{d}^2V}{\mathrm{d}r^2} + \frac{1}{r}\frac{\mathrm{d}V}{\mathrm{d}r} - \frac{V}{{L'_T}^2} = 0 \tag{2.13}$$

where $L'_T \equiv \sqrt{\frac{\rho_c}{R_s}}$. Solving this equation by applying the boundary conditions for the current flow $i(0) = 0$, $i(r_0) = i_0$, $i(r_1) = i_0$ and $i(\infty) = 0$, the voltage

difference ΔV across the spacing is given by

$$\Delta V = \frac{i_0 R_s}{2\pi}\left[\ln\left(\frac{r_1}{r_0}\right) + \frac{L'_T I_0(r_0/L'_T)}{r_0 I_1(r_0/L'_T)} + \frac{L'_T K_0(r_1/L'_T)}{r_1 K_1(r_1/L'_T)}\right] \tag{2.14}$$

where I_0, K_0, I_1 and K_1 are modified Bessel Functions of the first and second kind, respectively; r_0 and r_1 are the radii (Figure 2.2 b). When r_0 and r_1 are greater than L_T at least by a factor of 4, both I_0/I_1 and K_0/K_1 approximate to unity. Thus the total resistance across two contact pads becomes

$$R = \frac{\Delta V}{i_0} \approx \frac{R_s}{2\pi}\left[\ln\left(\frac{r_1}{r_0}\right) + L'_T\left(\frac{1}{r_1} + \frac{1}{r_0}\right)\right] \tag{2.15}$$

In this measurement, the central circle has the same radius, *i.e.* r_0 = constant. Differentiating Eq. 2.15 respect to the term $\left[\ln\left(\frac{r_1}{r_0}\right)\right]$ gives

$$\frac{\mathrm{d}R}{\mathrm{d}\left[\ln\left(\frac{r_1}{r_0}\right)\right]} = \frac{R_s}{2\pi}\left(1 - \frac{L_T}{r_1}\right) \tag{2.16}$$

Because r_1 is designed to be much larger than L_T, the term $\left[\frac{L_T}{r_1}\right]$ is approximate to zero, implying a reasonable approximation that R is only the function of $\left[\ln\left(\frac{r_1}{r_0}\right)\right]$. Plotting the total resistance obtained from different r_1 values against $\left[\ln\left(\frac{r_1}{r_0}\right)\right]$ the R_s and ρ_c can be obtained (Figure 2.3b).

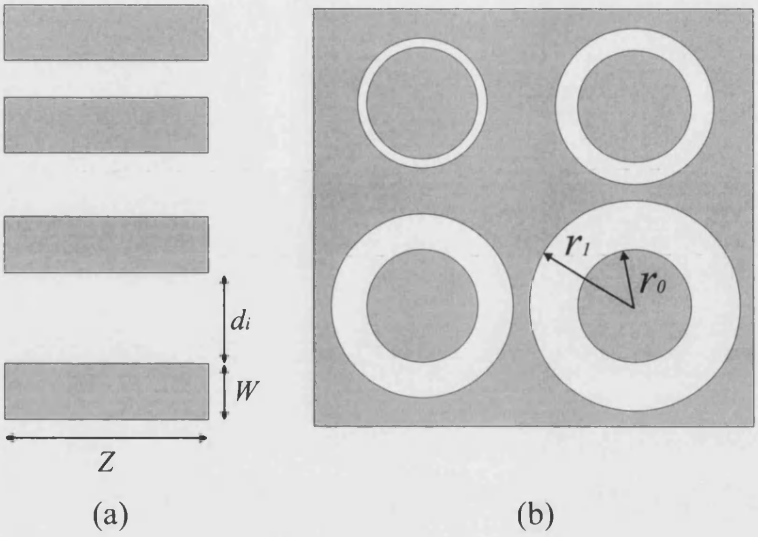

FIGURE 2.2: (a) Rectangular TLM and (b) circular TLM patterns for contact resistance measurement.

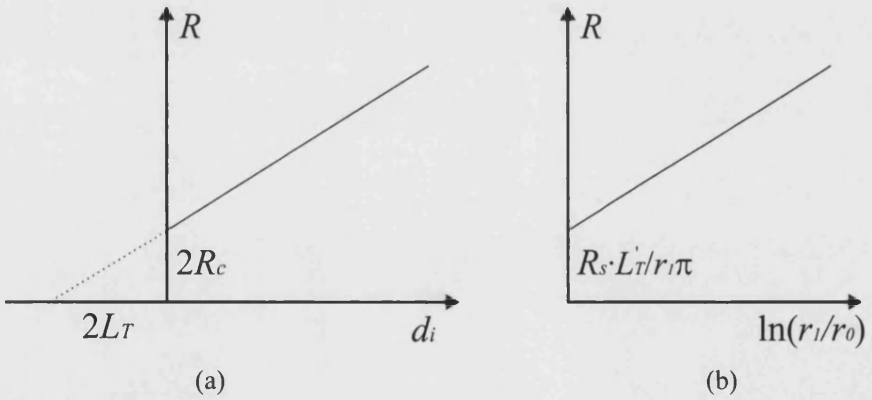

FIGURE 2.3: Plot of the total resistance against (a) spacing d_i in TLM pattern and (b) $\left[\ln\left(\frac{r_1}{r_0}\right)\right]$ in CTLM pattern.

2.1.3 n-GaN Ohmic Contacts

Current injection into semiconductor electronic devices is normally achieved via electrodes deposited on the semiconductors. In order to obtain ohmic current–voltage (I-V) behaviour there should be no barriers, or very thin depletion layers formed for tunnelling of carriers between semiconductors and electrodes. If a barrier is present, heat will be generated by the scattering of carriers during current injection and consequently a reduction in device lifetime will result.

High quality GaN films are very important for the fabrication of devices. An unintentionally doped GaN film shows n-type conductivity with a donor concentration of more than 10^{19} cm^{-3}. The origin of the donors is thought to be the nitrogen vacancies and/or residual impurities [5]. However, the quality of these films is not good enough for device applications. An AlN buffer layer was found to be very effective to achieve this goal, but the GaN film grown on the top of the AlN demonstrates a low donor concentration, less than 1×10^{16} cm^{-3}, with the resistivity more than 1 Ω·cm at room temperature. This issue can be solved by doping other impurities into the GaN film. It has been found that Si is a very effective dopant for n-GaN [6]. The donor concentration has been improved to 2×10^{18} cm^{-3} with a resistivity of 0.01 Ω·cm. The ionisation ratio for Si is increased with the increase of Si concentration, but the surface morphology may deteriorate.

The electron affinity (χ) of GaN has been measured to be 3.3 eV [28]. One can deduce that the work function of n-GaN (ϕ_s) is very close to 3.3 eV because the Fermi level (E_F) of n-GaN is in the range of 30 – 70 meV, which is very close to the conduction band level (Figure 2.4). After a metal and n-GaN are brought together, the barrier height is deduced to be $q(\phi_m - 3.3)$. Theoretically, ohmic contact behaviour can be obtained by using the materials which have their work function equal to or less than 3.3 eV. Figure 2.5 shows the work function of the commonly used metals. It is seen that most of metals have a work function in the 4 – 5 eV range, indicating the presence of a barrier between metals and n-GaN. However, increasing the donor concentration can transfer the mechanism of carrier transportation from thermionic to tunnelling, when the carriers can tunnel through a thinner depletion layer (Figure 2.4b).

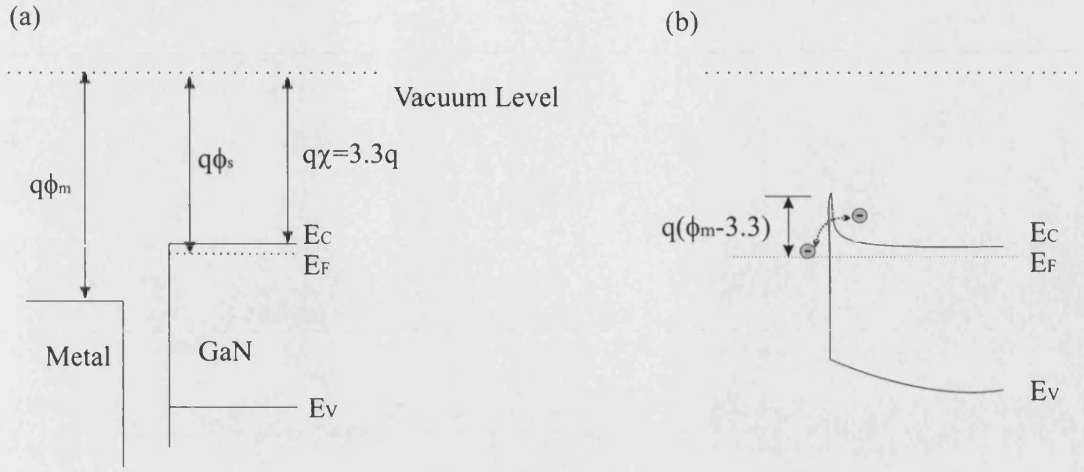

FIGURE 2.4: Band diagram of n-GaN and metal (a) before contact, and (b) after contact.

FIGURE 2.5: Work function of commonly used metals.

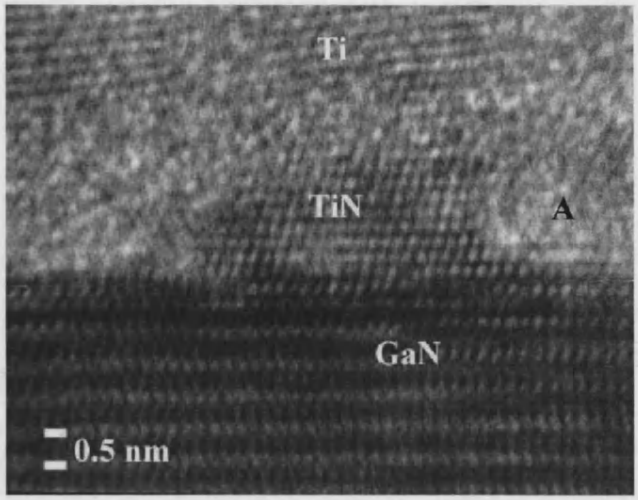

FIGURE 2.6: Microstructure of a Ti contact on n-GaN ("A" is the amorphous layer) [30].

Ti-based metal contacts are the commonly used electrodes for n-GaN. In the work of Luther *et al.* [29], Ti (150 nm) annealed at 800 °C in N_2 ambient pressure for 1 minute can achieve a low specific contact resistance 4×10^{-6} $\Omega\cdot cm^2$. Before annealing, the contact has shown an ohmic I-V behaviour. However, the work function of Ti is 4.33 eV, which is higher than the value of GaN 3.3 eV, indicating the presence of a barrier. The ohmic behaviour then may be due to the surface states generated during annealing and the high donor concentration ($> 10^{18}$ cm^{-3}) of n-GaN, resulting in a tunnelling regime for the carrier transportation between Ti and n-GaN. The high annealing temperature may decompose GaN and the removed nitrogen atoms react with Ti to form TiN. More nitrogen vacancies are generated at the surface, which can act as donors for n-GaN. Consequently a n^+-GaN layer is formed and tunnelling of carriers is possible. The result of annealing Ti in Ar ambient pressure showed that Ti reacts with the N atoms of GaN and forms TiN (Figure 2.6) [30].

W-based contacts for n-GaN have gained attention because of their thermal stability. The specific contact resistance for n-GaN is in the range 2.6×10^{-6} $\Omega\cdot cm^2$ to 1.1×10^{-4} $\Omega\cdot cm^2$ after annealing at about 1000 °C [32]-[34]. At such a high temperature nitrogen atoms in the GaN are easily removed and the compound decomposed [35]. Using Si implantation to increase the high electron concentration in shallow layers is an alternative method to achieve a low specific contact re-

sistance for n-GaN [36, 37]. However, the high activation annealing temperature (~1150 °C) of Si may result in a problem of decomposition for GaN [35].

In general, a low specific contact resistance in the range of 10^{-6} $\Omega \cdot cm^2$ for n-GaN has been achieved using a Ti/Al contact [29, 30]. W-based contacts show high thermal stability with a specific contact resistance $\sim 10^{-6}$ $\Omega \cdot cm^2$ [32]-[34]. The achievement of a low specific contact resistance is mainly attributed to the simplicity of n-GaN doping [6].

2.1.4 p-GaN Ohmic Contacts

Development of an ohmic contact for p-GaN with a low specific contact resistance is a very important issue for the development of III-nitrides optoelectronic devices. For example, the operating current density for a GaN laser is as high as 4.8 kA/cm^2 [7], which can generate massive heat from the interface of the metal and p-GaN and consequently limits the device lifetime. Nakamura *et al.* [8] has found that the heat enhances the metal migration through threading dislocations, which may electrically short the p-n junction. According to metal-semiconductor contact theory, the methods available for lowering the specific contact resistance are to increase the hole concentration and to use high work function metals. However, it is very difficult to obtain high hole concentrations because of the difficulties of incorporation of Mg and activation of the Mg dopant. Figure 2.7 demonstrates the band diagram of the metal and p-GaN contact. Because of the low acceptor concentration for p-GaN ($\sim 10^{17}$ cm^{-3}), the depletion layer is thick; hence the thermionic emission across the Schottky barrier is the dominant mechanism for the carrier transportation (Figure 2.7b). In addition, an automatic ohmic behaviour only can be obtained using a metal which has a work function higher than 6.6 eV. Unfortunately, there is no such known metal (Figure 2.5).

Considerable effort has been put into investigations of metallisation to lower the specific contact resistance of p-GaN ohmic contacts. Ni/Au with a total thickness of 8nm - 20nm has been widely used as the standard metal contact [11]. Ni [19], Au [19], Pd [44], Pt [50], Pd/Au [14], Ta/Ti [15], Pt/Ni/Au [16], and Pd/Pt/Au [18] have been investigated under the different annealing conditions and surface

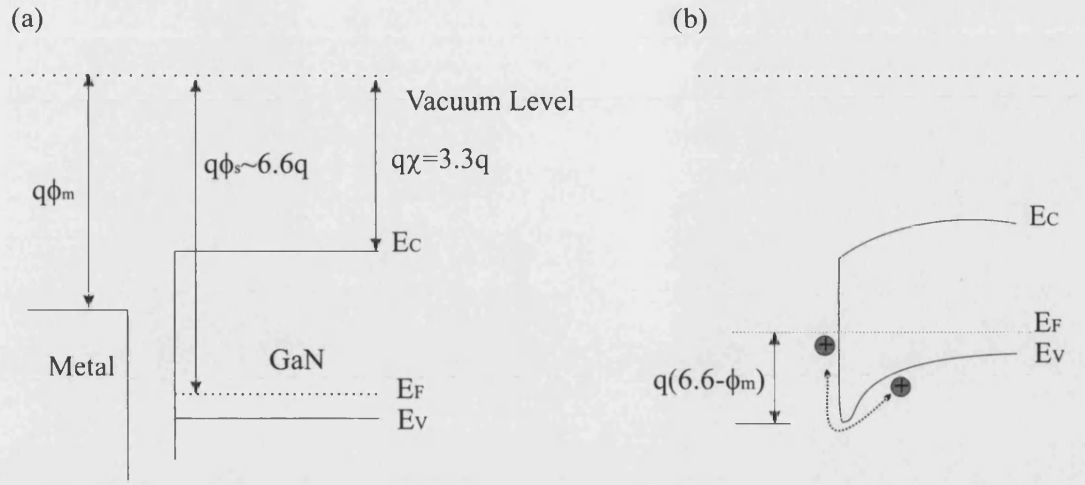

FIGURE 2.7: Band diagram of p-GaN and metal (a) before contact, and (b) after contact.

treatments.

One important issue has been raised concerning the growth of p-GaN. During the metal-organic chemical vapour deposition (MOCVD), the introduction of hydrogen is necessary for carrying metalorganic sources to the reactor and improving film quality. It has been found that the low p-type doping efficiency in the as-grown p-GaN is attributed to the formation of electrically inactive acceptor–hydrogen complexes [41]. For the as-grown p-GaN, only a fraction of Mg atoms acts as acceptors to compensate the presence of native or impurity-related donors. Götz *et al.* [9] have investigated the activation of acceptors in Mg-doped GaN in the temperature range 500 °C – 775 °C. For the as-grown p-GaN, the resistivity was as high as 10^{10} Ω·cm. After annealing at 775 °C, the resistivity was dramatically reduced to 3 Ω·cm. This improvement of p-GaN resistivity was mainly attributed to the dissociation of acceptor-hydrogen complexes rather than removal of separate compensating donors.

Another approach to obtain a high hole concentration is to increase the concentration of the Mg dopant. Kozodoy *et al.* [42] has studied the heavy doping effects in Mg-doped GaN. The hole concentration was increased to a certain value and then decreased while increasing the Mg dopant concentration. The observed compensation between donors and acceptors rose dramatically as the dopant level

was increased. This compensation is believed to be due to native donors and/or Mg-related states. However, the increase of Mg dopant concentration can effectively lower the activation energy. For the most heavily doped sample a severe degradation of the surface morphology, consisting of densely packed hexagonal pyramids, was observed.

Beside the improvement of p-GaN doping, different metal contacts for p-GaN have been examined. Fung *et al.* [43] investigated the electrical characteristics of Co, In, Mg, Mn, Ni, and Zn, each with a Au overlayer deposited on the p-GaN. For all the metals, none of the I-V characteristics is completely linear even after annealing. The specific contact resistance was found to be dependent on the work function of the metal, indicating the absence of Fermi level pinning. Koide *et al.* [10] characterised the Pt, Ni, Pd, Au, Cu, Ti, Al, and Ta contacts for p-GaN and similar results were observed.

The Ni/Au contact is still considered to be a cheap and effective electrode for p-GaN. Many reports show that this contact is very sensitive to the film thickness, annealing temperature and ambient atmosphere. Ho *et al.* [38] found that an annealing process in oxygen can dramatically improve the Ni/Au contact. The authors demonstrated that annealing at 500 ^{o}C in air introduced the formation of a mixture of crystalline NiO, Au, and amorphous Ni-Ga-O phases [39]. Small voids adjacent to the p-GaN film were also observed. During the annealing process, Ni atoms diffuse through the Au film onto the surface and react with oxygen to form NiO (Figure 2.8). Subsequently, the Au atoms were pushed down to form a Au-Ni alloy. It has also been discovered that different Ni/Au layer thicknesses gave different specific contact resistance [38]. Later studies found that a different thickness of Ni/Au gave the different bonding length for the Ni-O which affects the hole concentration of the Ni-O film [40]. This result suggested that the improvement of the oxidised Ni/Au contact for p-GaN may be due to the enhanced hole concentration at the Ni site.

Surface cleaning has been found to be very critical for the p-GaN ohmic contact; the presence of an oxide layer formed on the p-GaN surface can act as a barrier for carrier transportation. Buffered HF, KOH, aqua regia (HNO_3:HCl = 1:3), $(NH_4)_2S_x$ and HCl have been used to clean the p-GaN surface [12, 48]. A reduction of the native oxide layer was observed using these surface cleaning tech-

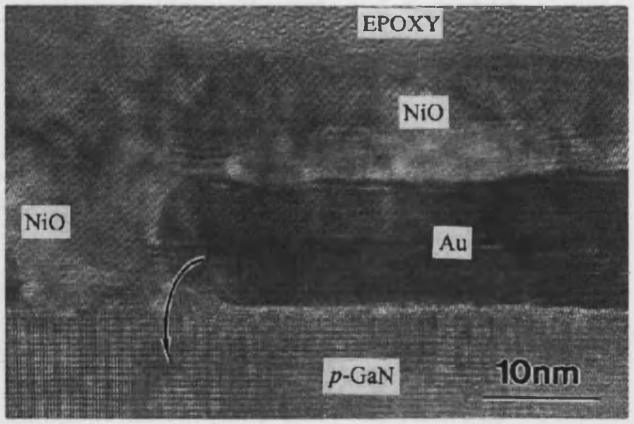

FIGURE 2.8: TEM picture of the Ni/Au/p-GaN film annealed at 500 °C for 10 minutes in air [38].

niques. $(NH_4)_2S_x$ was not only found to effectively remove the native oxide layer, but also an increase in hole concentration was observed [47]. Pt-based contacts have been found to be very greatly affected by the $(NH_4)_2S_x$ surface cleaning [13]. The specific contact resistance was decreased by three orders of magnitude after cleaning with alcohol-based $(NH_4)_2S_x$.

Kumakura *et al.* [51] used a thin strained InGaN layer to modify the p-GaN band structure. Because of the elastic strain, a very strong piezoelectric field is induced at the interface of the InGaN and p-GaN. An optimised InGaN thickness for lowering the specific contact resistance was 2nm. Another advantage of this strained InGaN layer is its high hole concentration and low work function. A Pd/Au contact deposited on this InGaN strained layer showed a linear I-V characteristic, indicating ohmic I-V behaviour. Higher specific contact resistance was observed using a thicker InGaN layer. The strain-induced piezoelectric field may well disappear due to the lattice relaxation with thicker InGaN films.

2.1.5 Transparent p-GaN Contacts

The realisation of a highly transparent p-GaN ohmic contact is particularly important for the light extraction from LEDs. However, the range of thickness of metal contacts is typically 20 nm – 150 nm, producing non-transparent lay-

ers. A highly transparent Ni/Au contact with thicknesses of 2nm/6nm has been obtained with 88% transmittance at 470 nm wavelength [19]. The specific contact resistance was found to be 1.7×10^{-2} $\Omega\cdot cm^2$. Before annealing, the light transmittance was approximately 50%. When the annealing temperature was increased to 400°C, the light transmittance was increased to 60%. A further increase of temperature to 450°C dramatically improved the transmittance to 83% light transmittance. Hence, the annealing process affects the light transmission.

Potential candidate materials for the transparent electrodes would be indium tin oxide (ITO) and ZnO. Both have a high light transmittance (>90%) in a wavelength range from 450 nm to 500 nm. The work function of ITO is 4.4 eV , which is not high enough to achieve ohmic contact behaviour for p-GaN [49]. ZnO has a similar work function to ITO, but has several advantages – high conductivity, inexpensive and abundant. In this chapter, ZnO will be considered as an electrode to try achieving a highly transparent ohmic contact.

2.2 Mechanism of Transparency for Annealed Ni/Au Contact

2.2.1 Waves in Thin Film System

For the simulation of light travelling in a thin film system, the most useful method is to solve Maxwell's equation. For isotropic and homogeneous media, these are:

$$\text{div}\,\mathbf{D} = \rho \tag{2.17}$$

$$\text{div}\,\mathbf{B} = 0 \tag{2.18}$$

$$\text{curl}\,\mathbf{E} = -\frac{\partial \mathbf{B}}{\partial t} \tag{2.19}$$

$$\text{curl}\,\mathbf{H} = \mathbf{J} + \frac{\partial \mathbf{D}}{\partial t} \tag{2.20}$$

The meanings of symbols are listed below:

Symbol	Description
$\mathbf{D}$	Electric displacement, $=\varepsilon_r\varepsilon_0\mathbf{E}$
$\mathbf{H}$	Magnetic intensity, $=\mathbf{B}/\mu_r\mu_0$
$\mathbf{B}$	Magnetic field
$\mathbf{E}$	Electric field
$\mathbf{J}$	Electric free current density, $=\sigma\mathbf{E}$
σ	Conductivity
ρ	Electric free charge density
t	Time
ε_0	Permittivity in vacuum
ε_r	Relative permittivity
μ_0	Permeability in vacuum
μ_r	Relative Permeability

Assuming that there is no space charge in the medium, *i.e.* div $\mathbf{D} = 0$, one can obtain the following equation from Maxwell's equations [17]:

$$\nabla^2\mathbf{E} = \varepsilon_r\varepsilon_0\mu_r\mu_0\frac{\partial^2\mathbf{E}}{\partial t} + \mu_r\mu_0\sigma\frac{\partial\mathbf{E}}{\partial t} \tag{2.21}$$

One solution for this equation is of the form [17]

$$\mathbf{E} = \mathbf{E}_0\exp[j\omega(t - \frac{x}{v})] \tag{2.22}$$

where $\mathbf{E}_0$ is the incident electric field, v is the velocity in a medium and $[j\omega(t-\frac{x}{v})]$ is the displacement at time t after a disturbance, created by the electric field at a point situated at x along the line of propagation.

The velocity of propagation through the medium of complex refractive index $N \equiv n-jk$ is related to the speed of light in a vacuum, c, by $v=c/N$. Substituting this into Eq. 2.22 one can obtain

$$\mathbf{E} = \mathbf{E}_0\exp(-\frac{\omega k}{c}x)\exp\left[j\left(\omega t - \frac{\omega n}{c}x\right)\right] \tag{2.23}$$

where n is the refractive index and k is the extinction coefficient. Physically, the real part, which is the function of k in the complex refractive index, represents the damping situation of the wave, while the imaginary part, which is related to n in the complex refractive index, represents the phase change of the wave.

2.2.2 Reflectance

When plane waves are incident on a boundary between two different media, some of the incident energy is transmitted and some is reflected (Figure 2.9). The energy reflection coefficient, or *reflectance*, is described below.

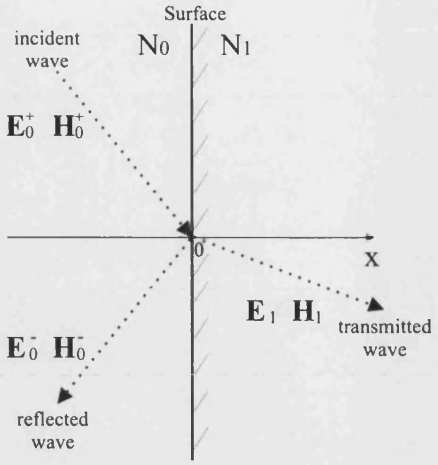

FIGURE 2.9: Illustration of the reflection.

From Eq. 2.20, Eq. 2.21 and Eq. 2.23 one equation can be obtained [66]:

$$\mathbf{H} = N(\mathbf{r} \times \mathbf{E}) \tag{2.24}$$

where $\mathbf{r} \equiv \alpha\mathbf{i} + \beta\mathbf{j} + \gamma\mathbf{k}$ is an unit vector along a propagation direction of a plane wave. For the positive-going and negative-going wave, Eq. 2.24 becomes

$$\begin{aligned} \mathbf{H}_0^+ &= N_0(\mathbf{i} \times \mathbf{E}_0^+) \\ \mathbf{H}_0^- &= N_0(-\mathbf{i} \times \mathbf{E}_0^-) \\ \mathbf{H}_1 &= N_1(\mathbf{i} \times \mathbf{E}_1) \end{aligned}$$

Applying the boundary conditions, the conservation of the tangential component of $\mathbf{E}$ and $\mathbf{H}$ at x=0,

$$\begin{aligned} \mathbf{E}_1 &= \mathbf{E}_0^+ + \mathbf{E}_0^- \quad at\ x = 0 \\ \mathbf{H}_1 &= \mathbf{H}_0^+ + \mathbf{H}_0^- \quad at\ x = 0 \end{aligned}$$

so that

$$\begin{aligned} N_1(\mathbf{i}\times\mathbf{E}_1) &= N_0(\mathbf{i}\times\mathbf{E}_0^+ - \mathbf{i}\times\mathbf{E}_0^-) \\ N_1\mathbf{E}_1 &= N_0(\mathbf{E}_0^+ - \mathbf{E}_0^-) \\ \mathbf{E}_0^- &= \frac{N_0 - N_1}{N_0 + N_1}\mathbf{E}_0^+ \end{aligned}$$

The term $(\frac{N_0 - N_1}{N_0 + N_1})$ is the amplitude reflection coefficient. From the expression for the Poynting vector the energy reflection coefficient or *reflectance*, R, is give by

$$R = \left(\frac{N_0 - N_1}{N_0 + N_1}\right)\left(\frac{N_0 - N_1}{N_0 + N_1}\right)^* \tag{2.25}$$

where * is the complex conjugate.

2.2.3 Interference

In a thin film system, the incident light (Ψ_i) is reflected at the interface between the incident medium and thin film (Ψ_1), and is reflected from the interface between the thin film and substrate (Ψ_2). When Ψ_2 enters into the incident medium and meets Ψ_1, the two waves experience constructive (Figure 2.10a) or destructive interaction (Figure 2.10a). This phenomenon is called interference. Substituting $\omega = 2\pi f$ and $c = f\lambda$, where f and λ are the frequency and wavelength of a plane wave, respectively , to Eq. 2.23, the electric field is in the form of

$$\mathbf{E} = \mathbf{E}_0 \exp(-\frac{\omega k}{c}x) \exp\left[\mathbf{j}\left(\omega t - \frac{2n\pi}{\lambda}x\right)\right] \tag{2.26}$$

From figure 2.10 it is seen that the phase difference for constructive and destructive interference is $\mathbf{m}\pi$ and $(\mathbf{m}+1/2)\pi$, respectively, where $\mathbf{m}$ is an integer.

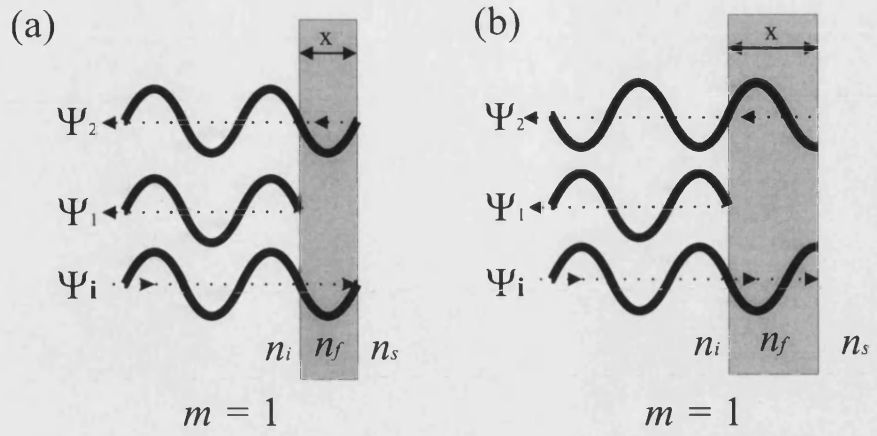

FIGURE 2.10: Illustration of the interference of (a) constructive and (b) destructive.

According to Eq. 2.26, the condition is given by

$$\begin{aligned} \frac{2n\pi}{\lambda}x &= \mathbf{m}\pi \\ x &= \mathbf{m}\frac{\lambda}{2n} \end{aligned} \tag{2.27}$$

for constructive interference and

$$\begin{aligned} \frac{2n\pi}{\lambda}x &= \left(\mathbf{m}+\frac{1}{2}\right)\pi \\ x &= \left(\mathbf{m}+\frac{1}{2}\right)\frac{\lambda}{2n} \end{aligned} \tag{2.28}$$

for destructive interference. These conditions are valid only if $n_i < n_f < n_s$ or $n_i > n_f > n_s$.

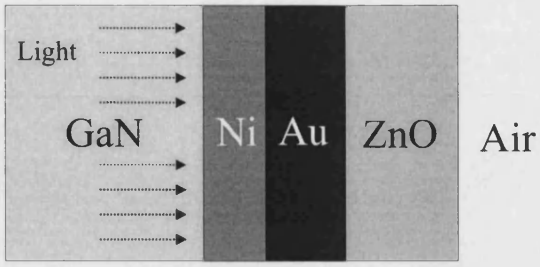

FIGURE 2.11: Setup for the simulation of light transmittance.

2.2.4 Optical Simulation for Ni/Au Contact on GaN

Optical simulation for a Ni/Au film is based on the theory described above. One suite of optical simulation software, **Essential Macleod** (Version 8.5c), was employed for calculation of the transmittance of the Ni/Au layer (Figure 2.11). Table 2.1 shows the optical properties used in this simulation. The optical properties of GaN were taken from the study of Yu *et al.* [20] and Ambacher *et al.* [21]. ZnO optical properties were adapted from the work of Dumont *et al.* [22]. In this simulation, the normal incidence of light from GaN film was assumed.

Optical Properties of Au		
Wavelength (nm)	Refractive Indices	Extinction Coefficient
200.00	1.43	1.215
450.00	1.40	1.88
470.00	1.176	1.9688
500.00	0.84	2.102
550.00	0.33	2.324
600.00	0.20	2.897
650.00	0.14	3.374
700.00	0.13	3.842
750.00	0.14	4.266
800.00	0.15	4.654

Optical Properties of Ni		
Wavelength (nm)	Refractive Indices	Extinction Coefficient
440	1.56	2.68
470	1.7	2.857
540	1.85	3.27
660	2.06	3.89
775	2.43	4.31
800	2.48	4.38

Optical Properties of GaN		
Wavelength (nm)	Refractive Indices	Extinction Coefficient
375	2.51	0.011966462
406	2.46	0.006493999
437.5	2.435	0.00351633
469	2.405	0.00447862
500	2.41	0.002347535
562	2.35	0.001811263
625	2.34	0.00109419
688	2.32	0.001040237
750	2.305	0.00077588

Optical Properties of ZnO		
Wavelength (nm)	Refractive Indices	Extinction Coefficient
400	2.19	0.00625
412.5	2.14	0.0035
425	2.09	0.00625
450	2.06	0.00625
462.5	2.045	0.00625
475	2.03	0.00625
487.5	2.024	0.00625
500	2.0125	0.00004
550	1.98	0.00004
600	1.96	0.00004
650	1.945	0.00004
700	1.94	0.00004

TABLE 2.1: Optical properties of Ni [66], Au [66], GaN [20, 21] and ZnO [22].

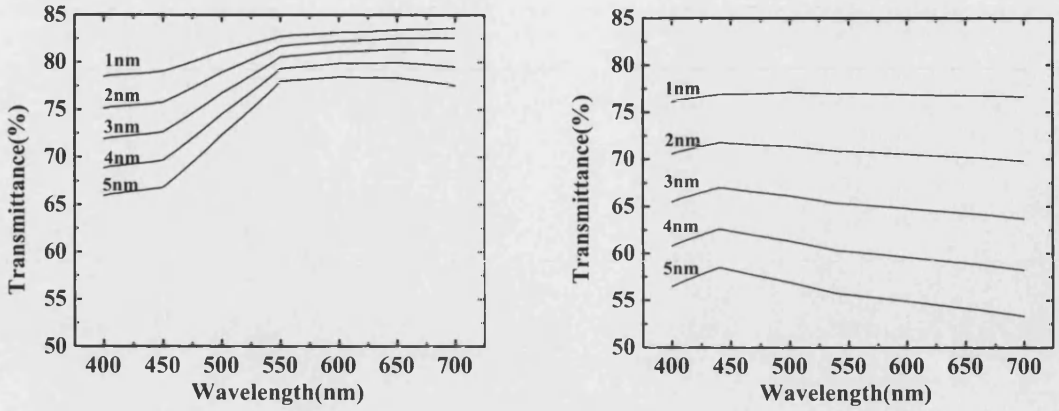

FIGURE 2.12: Simulated light transmittance of (a) Au and (b) Ni film for the thickness 1 – 5nm.

The light transmittance of either single Ni or Au film on the GaN film was simulated for the thickness range 1 – 5 nm. Figure 2.12 demonstrates the simulation results. It is seen that a light transmittance of 69% and 57.7% was obtained for Au and Ni having a thickness of 5 nm, and this decreased with increasing the thickness. According to Eq. 2.27 and Eq. 2.28, the minimum thickness for the presence of interference in the wavelength larger than 400nm has to be 143nm for Au and 133nm for Ni, which is much larger than the thickness of 5nm for the simulation. Based on Eq. 2.26, the contribution to the decrease of light transmission is from the real part, which represents the light absorption. In addition, the light transmission of Ni is lower than that of Au due to the higher extinction coefficient.

In practice, the Ni/Au film can be highly transparent (~80%) after annealing in N_2 atmosphere [19]. During annealing, Au will diffuse through Ni and reach the GaN surface [1]. One simplified simulation which assumed that the Ni/Au = 5nm/5nm film was transformed to Au/Ni/Au/Ni/Au = 1nm/2nm/2nm/3nm/2nm was conducted. According to Eq. 2.25, the reflectance between Au and Ni film is only ~0.4% for the wavelength of 400nm to 700nm, indicating that the absorption is the dominant factor for light transmittance. It implies that the total thickness of Ni/Au film is the main contribution to the light transmission, indicating that the increase of light transmission for the annealed Ni/Au film [19] may be due to the change of the film thickness.

2.2.5 Surface Morphology of Ni/Au After Annealing

In order to examine the change of surface morphology, a Ni/Au = 5nm/5nm film was deposited onto GaN by thermal evaporation. This thickness was chosen because it can be used to compare with the work of Sheu *et al.* [19]. The annealing was conducted in a tube furnace at 500 °C in N_2 ambient for 10 minutes. AFM was used to characterise the surface morphology of the as-grown and annealed Ni/Au film.

Figure 2.13a shows the as-grown Ni film on p-GaN. The RMS surface roughness was measured to be 0.58 nm, indicating continuity of the Ni film. Subsequently, a Au film was deposited on the Ni film (Figure 2.13b). The surface roughness was measured to be 0.55 nm, demonstrating uniform deposition of the Au film. The Ni layer has rounded grains with a typical size of 20 nm. This rounded structure may be due to the initial nucleation process of the Ni film. After the deposition of the Au layer, the surface morphology remained similar. The sample was then annealed at 500 °C in N_2 for 10 minutes (Figure 2.13c). It is seen that the small rounded structure of the as-grown Ni/Au layer has changed to form an island structure.

According to the simulation results, the main contribution to the high light transmission in the Ni/Au contacts is the decrease in thickness of the Ni/Au films. From the AFM image it is seen that the Ni/Au film formed open areas after annealing, indicating the decrease of the thickness in these areas. These results suggested that the high light transmission may be due to the formation of the open areas exposed by the change in the Ni/Au structure.

2.3 Development of Ni/Au/ZnO Transparent Contact for p-GaN

Ni/Au was found to be highly transparent after annealing; the measured transmittance was in the range of 70% – 80% in the visible light range. One anti-reflection coating on top of the Ni/Au can extract even more light from LEDs.

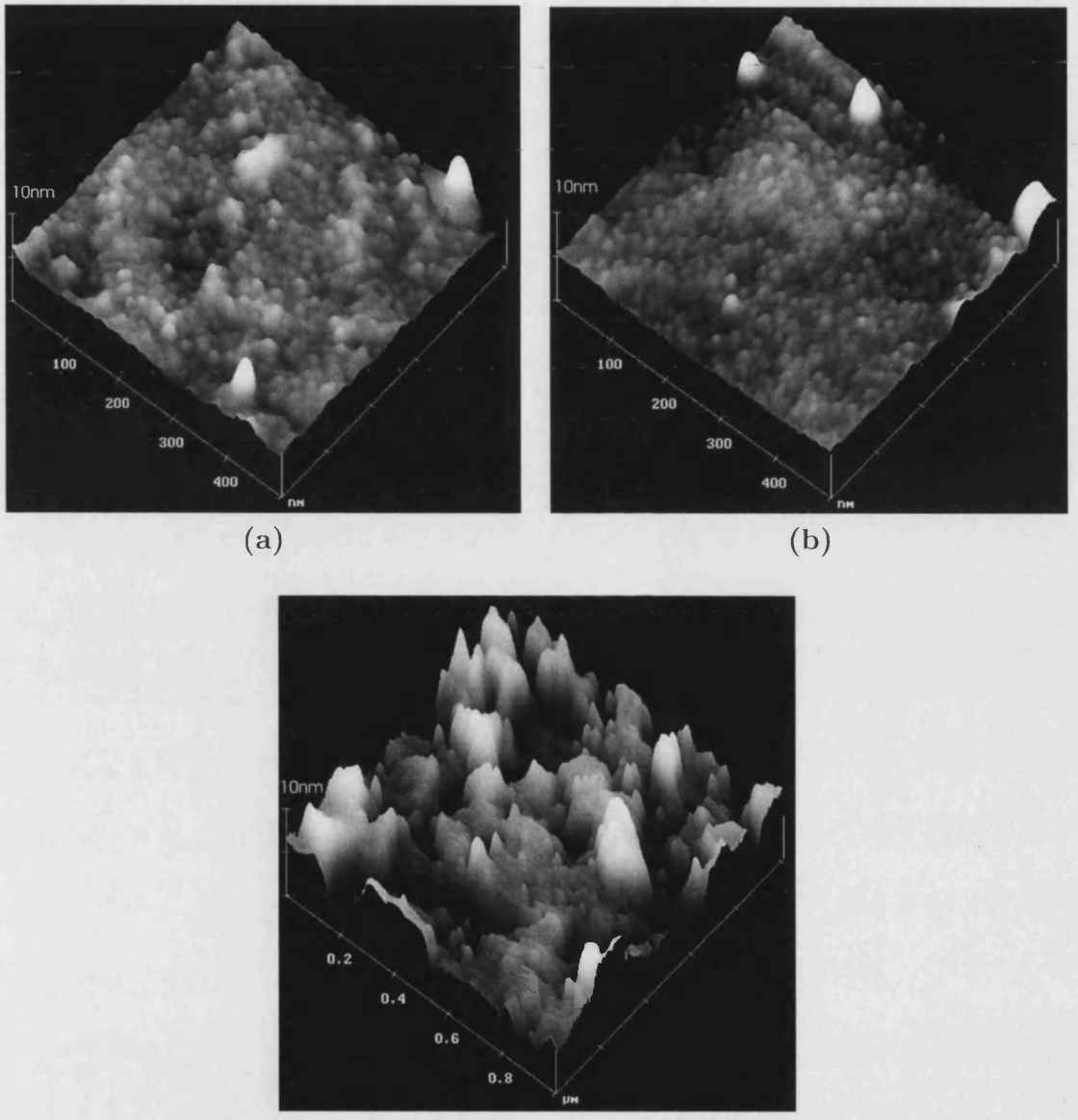

FIGURE 2.13: AFM image of the (a) as-grown Ni (5nm), (b) as-grown Ni/Au (5nm/5nm) and (c) annealed Ni/Au (5nm/5nm) film.

However, this anti-reflection layer itself needs to be highly transparent at the emission wavelength range and also to be electrically conductive.

ZnO is a potential material for the development of transparent contact for p-GaN. The synthesis processes of ZnO can be sol-gel [23], MOCVD [24], ion sputtering [25], or e-beam evaporation [26]. It is a semiconductor with a bandgap of 3.2 eV [63] and both n-type and p-type ZnO are available [62]. The melting point of ZnO is 1800 ^{o}C [31], indicating its thermal stability. In addition, the processing of ZnO is relatively simple since wet or dry etching is possible [52, 53].

2.3.1 ZnO Growth by Ion Beam Sputtering

Introduction

Several techniques allow growth of poly-crystalline ZnO with the preferred orientation (002) [57, 23, 26]. This poly-crystalline film with some additives, *eg.* Bi and Sb, shows non-linear I-V characteristics and has been used to fabricate varistors [55]. The unintentionally doped ZnO itself is an n-type semiconductor and Al has been found to be an effective dopant for increasing the donor concentration and has a minor effect on the optical transmission [54]. The resistivity of the Al-doped ZnO film is normally in the range of 10^{-3} Ω·cm and the optical transmission in the visible range is about 90%. The donor concentration is typically 10^{19} cm^{-3} with a Hall mobility 10 – 20 cm^2/V·s.

It is difficult to dope p-ZnO because the donor level is very deep so that even low thermal energy can excite donors into the valence band. In 1999, Yamamoto *et al.* [56] proposed a codoping method, which use nitrogen atoms to replace two of the 16 sites of the oxygen atoms and one of group III elements to replace one of the 16 sites of the Zn atoms, as a solution for p-ZnO fabrication. In the same year, this method was successfully realised by Joseph *et al.* [57] and a reasonable resistivity (2 Ω·cm) and hole concentration (4×10^{19} cm^{-3}) was obtained by pulsed laser deposition. A Ga-doped ZnO target was used and another dopant N formed by passing N_2O gas through an electron cyclotron resonance plasma source. In this codoping method, both Ga and N dopants are doped at the same time and the

substitution of nitrogen at the appropriate site in the ZnO lattice is stabilised by the formation of N-Ga-N type bonds. It effectively reduces the repulsive interaction of N acceptors, leading to the enhancement of the acceptor doping. In 2000, a ZnO p-n junction was fabricated [58]. A diode I-V characteristic and white-violet electroluminescence at a wavelength range 370 – 380 nm was obtained.

The synthesis process for ZnO film can be varied. The sol-gel processes for the synthesis of ZnO films is attractive because it has the advantage of the elimination of the need for a vacuum, and the potential for preparing large area and non-flat substrates [23]. The resistivity of Al-doped sol-gel film has reached 5×10^{-3} Ω·cm. However, this process involves heating to high temperatures, which involves the possibility of damaging devices. In addition, residual organic constituents and film uniformity are the other issues. E-beam evaporation is well known to be clean and gives a very uniform deposition. Ma *et al.* [26] have studied the Al-doped ZnO film deposited by e-beam evaporation. The resistivity of this Al-doped ZnO film was 5×10^{-3} Ω·cm with a donor concentration of 10^{19} cm^{-3}, which is very close to the values for the film coated by the sol-gel technique.

Much effort has been devoted to the sputtering deposition of ZnO films because this deposition method gives good uniformity for the films and is a simple method for doping. Kim *et al.* [59] have investigated the Al-doped ZnO film prepared by RF magnetron sputtering. The targets used in their study were ZnO sintered with different Al_2O_3 weight percentage additions. Structural analysis showed a preferred ZnO (002) orientation and most of Al atoms were substituted in the Zn sites. This Al-doped ZnO film had a grain size of 0.1 – 0.2 μm when grown at room temperature and ~0.6 μm when grown at 150 – 300 °C. The electrical properties were found to be strongly affected by the substrate temperature and working pressure. Higher substrate temperature resulted in a higher resistivity, whereas the lower working pressure gave a lower resistivity. The electrical measurements demonstrated a low resistivity, 4.7×10^{-4} Ω·cm, with a donor concentration of 7.5×10^{20} cm^{-3} using a 3 wt% Al_2O_3 target. In the optical measurement, it showed a minor effect for the light transmission at the wavelengths, 450 nm.

The oxygen and substrate temperature has a significant effect on the ZnO structural, electrical and optical properties. Subaramanyam *et al.* [63] investigated

these two effects for the ZnO film grown using a DC reactive magnetron sputtering system. A Zn metallic target with a purity of 99.99% and glass substrates were used in their study. The XRD data showed a ZnO (002) preferred orientation for all samples. The samples grown at low oxygen partial pressure had metallic characteristics and the optical transmittance was 50% less in the visible light range. After the Zn signal in XRD data disappeared, a further increase of oxygen partial pressure showed a reduced effect on the optical transmission. At a low substrate temperature, a mixed phase of Zn and ZnO was observed but the intensity of ZnO (002) was increased with increase in the substrate temperature.

Ion beam sputtering deposition is the alternative for thin film coating. It permits the independent control of beam energy, direction, and current flux. However, the operating pressure is very low ($\sim 10^{-4}$ torr), demonstrating the high energy of the sputtered particles. Quaranta *et al.* [60] have studied ZnO films sputtered from a ZnO target by a dual ion beam sputtering system. The possible contamination elements, *e.g.*, molybdenum, argon, or iron, was examined and none of these elements were discovered in the ZnO films. The stoichiometry of the ZnO film was found to be strongly dependent on the oxygen irradiation by the second ion gun. According to the XRD data, the ZnO (002) preferred orientation, with a grain size of $\sim$10 nm, was observed. The (002) peak was shifted to a lower value of 2θ, indicating the presence of compressive stress. These deposited ZnO films had a resistivity in the range of 10^{-3} to 10^{5} Ω·cm. The optical properties were also found to be significantly affected by the oxygen irradiation. The results are similar to those of the ZnO films grown by RF magnetron sputtering. The thermal stability was examined by the authors [61]. After annealing the ZnO films, which were irradiated by hydrogen, at 200 ^{o}C in air, the resistivity of the ZnO films remained identical, indicating high thermal stability .

Recently, Xiong *et al.* [62] reported their ability to fabricate p-ZnO and n-ZnO on a Si (001) substrate by a DC planar magnetron sputtering system. The resistivity of the p-ZnO film has achieved 3 Ω·cm with a hole concentration of 9×10^{17} cm^{-3}. One p-n junction has been fabricated and a turn-on voltage of 1V was observed. The control of p-type and n-type conductivity was achieved simply by controlling the oxygen partial pressure. While increasing the oxygen partial pressure, the carrier concentration of n-ZnO decreased to less than 10^{15} cm^{-3} and the film was then transformed to p-type with further increase of oxygen partial pressure.

However, the formation mechanism of p-ZnO has yet to be explained.

For ZnO thin film fabrication, ion beam sputtering is a good method to control the film thickness, uniformity and flow rate of additional reactive gases. Because substrate temperature and O_2 partial pressure have significant effects on the ZnO film properties, the investigation of these two factors for the ZnO films grown by ion beam sputtering is needed. However, a detailed study for the ZnO film grown by an ion beam sputter system using a Zn metallic target and glass substrate is still absent. The following experiment was undertaken to investigate the effect of substrate temperature and O_2 flow rate on the structural, electrical and optical properties of the ZnO film.

Experiment

The unintentionally doped ZnO films were deposited on glass substrates by a Nordiko Dual Ion Beam Sputtering System (Figure 3.15). Before deposition, the chamber was evacuated to $\sim 10^{-8}$ torr. The purity of the Zn metallic target was 99.99%. The Ar flow rate of the ion gun was kept to 50 sccm. The substrate temperature was maintained at room temperature while growing the ZnO film in a flow rate of 2 – 8 sccm (ZnO [O_2 = 2 – 8 sccm]). The O_2 flow rate was fixed at 6 sccm while growing the ZnO film at a substrate temperature of 20 °C – 400 °C (ZnO [T_s = 20°C – 400°C]). The chamber pressure was maintained at $\sim 2 \times 10^{-4}$ Torr, which varied slightly with any change in the O_2 flow rate. Transmission Electron Microscopy (TEM), X-ray Diffractometry (XRD) and Wavelength Dispersive X-ray Spectrometry (WDX) were employed for the structural studies. The TEM samples were prepared by depositing the ZnO film onto sodium chloride (NaCl) substrates and the ZnO film later removed in water. Hall mobility and carrier concentration were measured by the van der Pauw four-probe method.

Results and Discussion

Structural Properties

The Zn content of the ZnO grown in the different O_2 flow rates and substrate temperatures is shown in Figure 2.14. It is seen that the ZnO films remain nearly stoichiometric until the O_2 flow rate is less than 4 sccm. This may be attributed to the reduced amount of O_2 reacting with Zn metal before deposition. The increase in substrate temperature results in a higher Zn content in the ZnO film. There was a dramatic increase observed as the substrate temperature increased to higher than 220 °C. Similar effects have been discovered in the ZnO film grown by RF magnetron sputtering using a ZnO target [64]. The authors suggested that the higher substrate temperature provides enough energy for the Zn-O bond breaking. In this experiment, the Zn target may also have contributed to this discovery. The majority of the sputtered Zn particles react with oxygen in the chamber and form ZnO particles. However, some Zn particles are directly deposited on the substrate without reacting with oxygen. At high substrate temperature, these Zn particles obtained enough energy to form a large grain before they react with oxygen. Hence, it results in a Zn-rich ZnO film at high substrate temperature.

A preferred orientation (002) ZnO was observed for O_2 flow rates higher than 3 sccm and high substrate temperature samples. This observation is similar to the ZnO films grown by different methods [60, 63]. Figure 2.15 shows the XRD spectra for ZnO prepared at different O_2 flow rates. ZnO crystalline growth was observed when the O_2 flow rates were higher than 3 sccm and the films formed with a preferred (002) orientation. No (002) peak shift was observed with increase of the O_2 flow rate, indicating the absence of induced strain at by higher oxygen flow rates. Figure 2.16 demonstrates the XRD spectra for the samples grown at different substrate temperatures. It is seen that the (002) peak intensity becomes stronger and the ZnO (004) peak is seen to be present and gets stronger when the substrate temperature is increased. However, the ZnO film grown by the DC magnetron sputtering method on a glass substrate using a Zn metallic target showed a different growth pattern [63]. ZnO (102) and (200) XRD peaks were found at low oxygen partial pressure and diminished with further increase of the oxygen partial pressure. A further increase of substrate temperature from

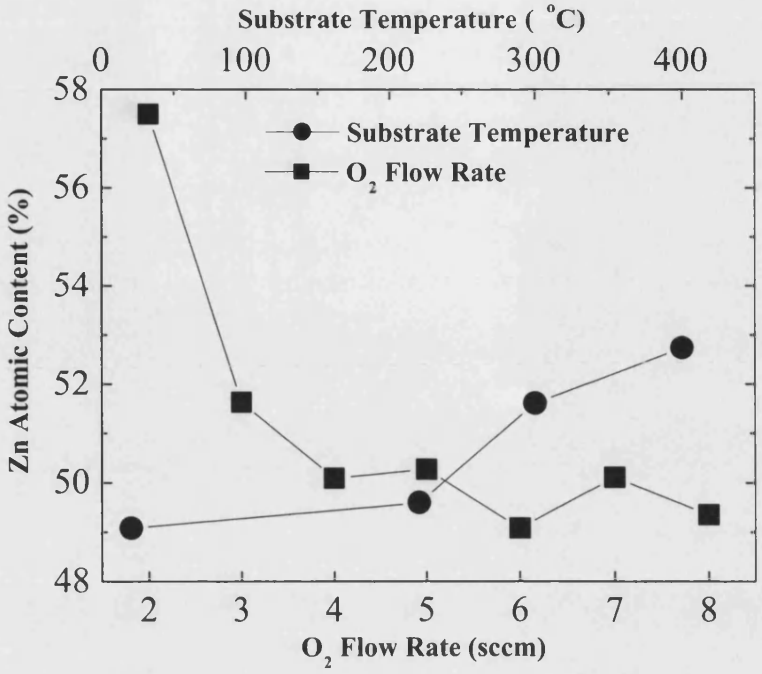

FIGURE 2.14: Zn content measured by WDX for a ZnO film grown at different O_2 flow rates and substrate temperatures.

275 °C to 350 °C gave a diminished ZnO (102) peak which then disappeared at a temperature above 390 °C. The different growth pattern may be due to the different bombardment energy of ZnO and Zn particles toward to the glass substrate. The (002) peak was shifted from 33.82° for ZnO [T_s = 20°C] to 34.2° for ZnO [T_s = 400°C], indicating that a significant compressive strain had been built up when the substrate temperature was increased. This may in fact be due to the thermal mismatch between the substrate and ZnO film as it is grown.

The grain size (D_g) can be estimated by analysis of the XRD peak broadening as:

$$D_g = \frac{0.9\lambda}{\beta \cos\theta} \tag{2.29}$$

where λ is the wavelength of X-ray, β is the FWHM, and θ is the Bragg angle. Figure 2.17 shows the FWHM as a function of substrate temperatures and O_2 flow rates. It implies that the grain size for ZnO [O_2 = 4 sccm] was large but

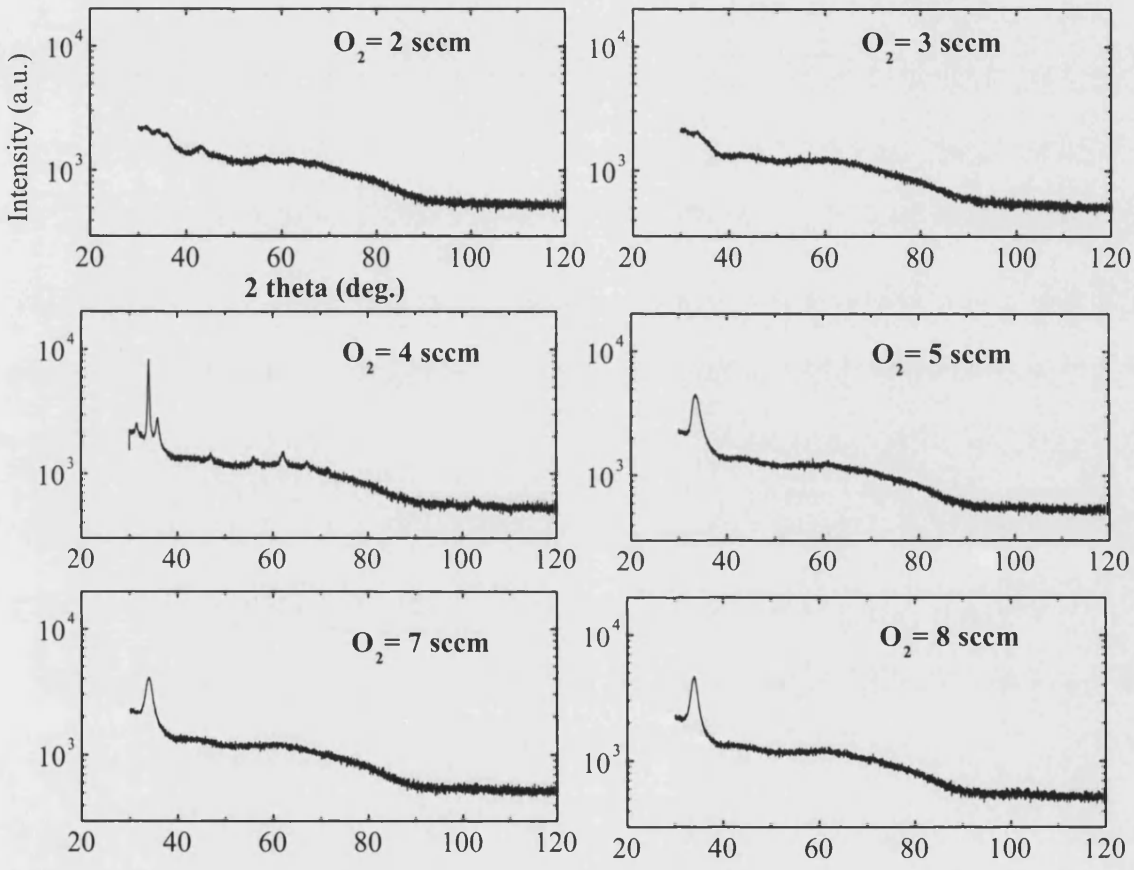

FIGURE 2.15: XRD spectra of ZnO film grown at different O_2 flow rates. Note that T_s = 20 °C.

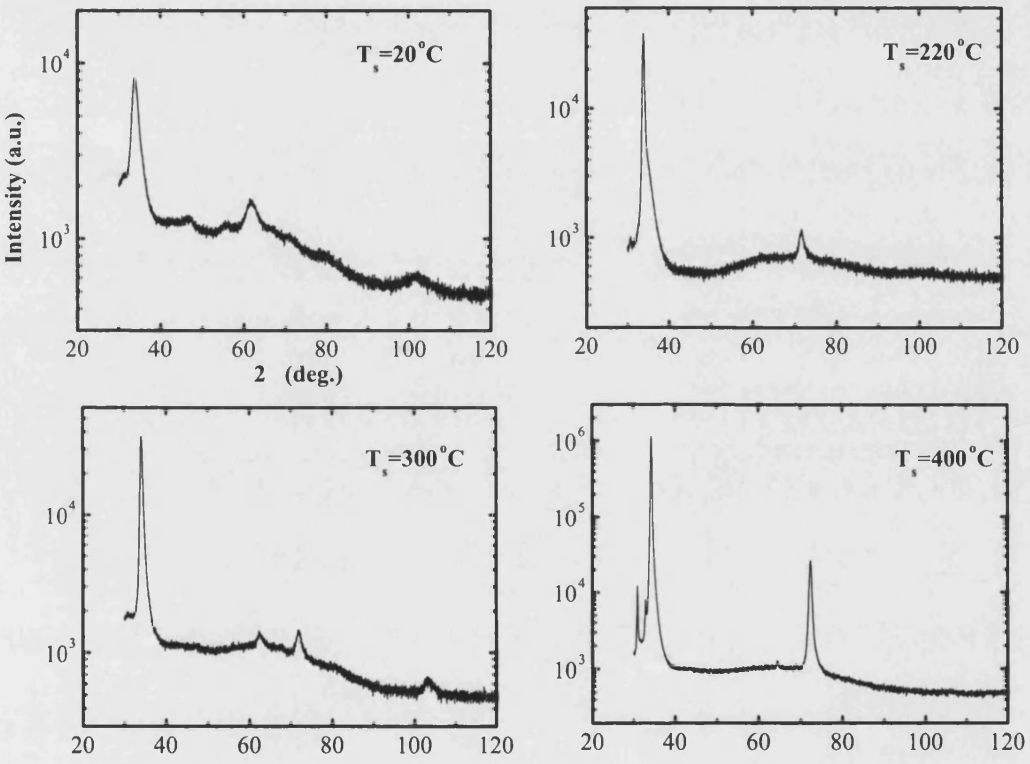

FIGURE 2.16: XRD for Substrate temperature effect. Note that the O_2 flow rate = 6 sccm.

decreased dramatically for ZnO [O_2 = 5 sccm]. The grain size was retained at a similar size while increasing the O_2 flow rate to more than 5 sccm. The FWHM for ZnO [T_s = 20 °C - 400 °C] shows that the increase of substrate temperatures induced the most significant grain growth. It is also worth noting that the stresses generated in the ZnO thin films contribute to X-ray broadening and so to a decrease in **D** values. Thus, the real grain size would be expected to be somewhat larger than the calculated value. Figure 2.18 shows the TEM pictures of ZnO [O_2 = 4 sccm], ZnO [O_2 = 6 sccm] and ZnO [T_s = 400 °C]. The micrographs show crystalline grains with non-crystalline boundaries. ZnO [O_2 = 4 sccm] has a wide amorphous grain boundary, good crystallinity, and rounded and small grains (Figure 2.18a, 2.18b). When the O_2 flow rate was increased to 6 sccm, the amorphous grain boundary region was still present but became narrower, and the grain size was also smaller (Figure 2.18c, 2.18d). No clear growth pattern was apparent for the ZnO [O_2 = 4 sccm]. For the ZnO film grown at high substrate temperatures, narrower amorphous grain boundaries and better crystallinity were observed (Figure 2.18e, 2.18f). The diffraction pattern (Figure 2.19) for ZnO [O_2 = 4 sccm] was spotty but this was not the case for the ZnO [O_2 = 6 sccm], indicating that ZnO [O_2 = 6 sccm] had a much finer grain size and more non-crystalline material present. These observation are consistent with the XRD and its FWHM data. The ZnO [T_s = 400 °C] diffraction pattern was also spotty and Zn (101) was observed to be present, which is consistent with the observed Zn-rich ZnO films in WDX data.

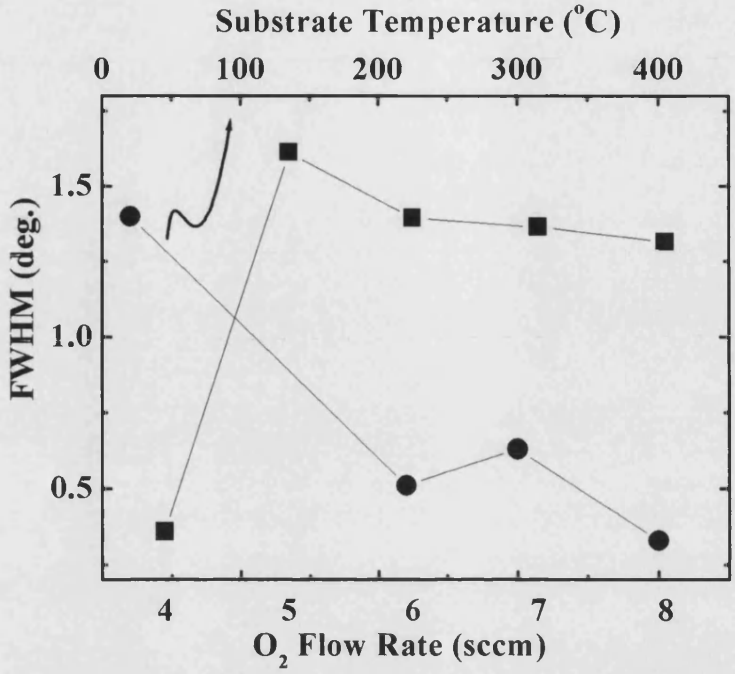

FIGURE 2.17: FWHM as a function of substrate temperature and O_2 flow rate.

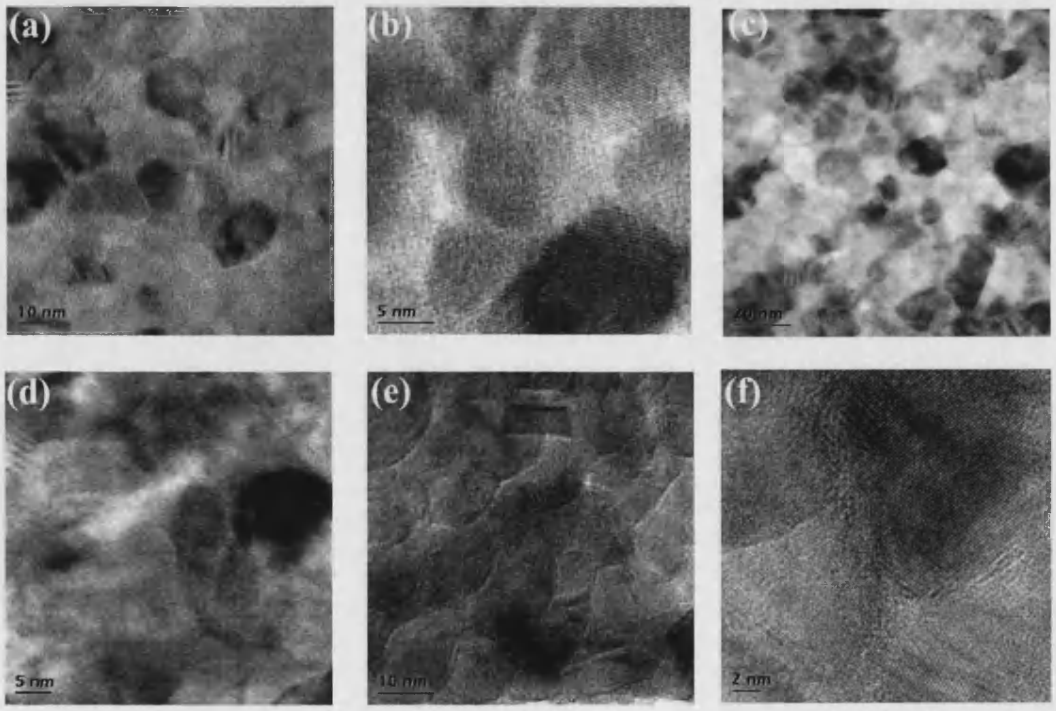

FIGURE 2.18: TEM pictures for the ZnO film (a), (b) for ZnO [O_2 = 4 sccm], (c), (d) for ZnO [O_2 = 6 sccm] and (e), (f) for ZnO [T_s = 400°C].

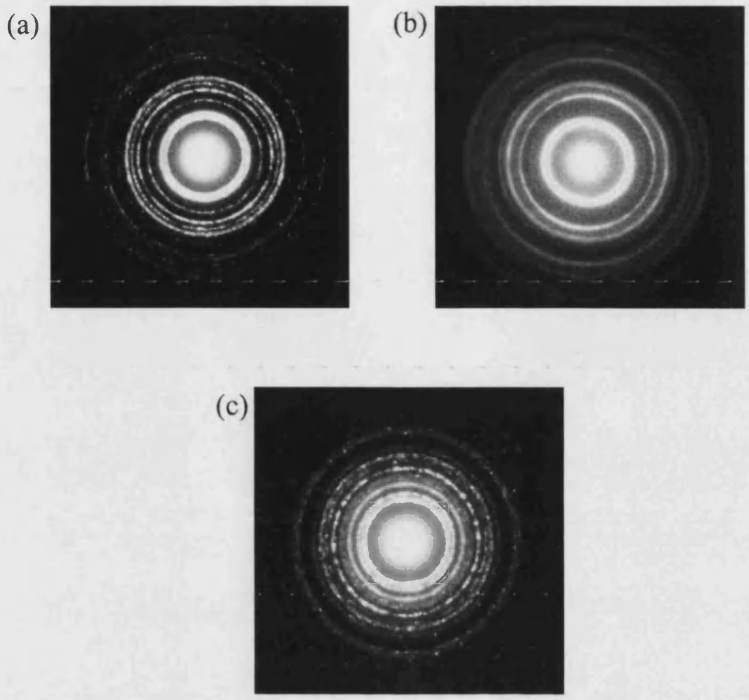

FIGURE 2.19: Diffraction pattern of the ZnO films. (a) ZnO [O_2 = 4 sccm], (b) ZnO [O_2 = 6 sccm], and (c) ZnO [T_s = 400°C].

Electrical Properties

The electrical properties of ZnO [O_2 = 2 – 8 sccm] and ZnO [T_s = 20 °C – 400 °C] are shown in Figure 2.20. The resistivity reached its lowest value 1.6×10^{-3} Ω·cm for ZnO [O_2 = 4 sccm] and increased with higher O_2 flow rates. Higher substrate temperature during sputtering results in higher resistivity of the ZnO film. The Hall mobility measurements indicate that all the ZnO films are n-type. The carrier mobility was found to increase until an O_2 flow rate of 5 sccm was reached and it then decreased with a further increase in the O_2 flow rate. The carrier measurements showed a decreasing trend with increasing substrate temperature and O_2 flow rate. The high substrate temperatures and O_2 flow rates gave higher oxygen contents in the ZnO film. From this observation it implies that the resistivity is dependent on the oxygen content, indicating that the resistivity of n-ZnO in this experiment is dominated by oxygen vacancies [27].

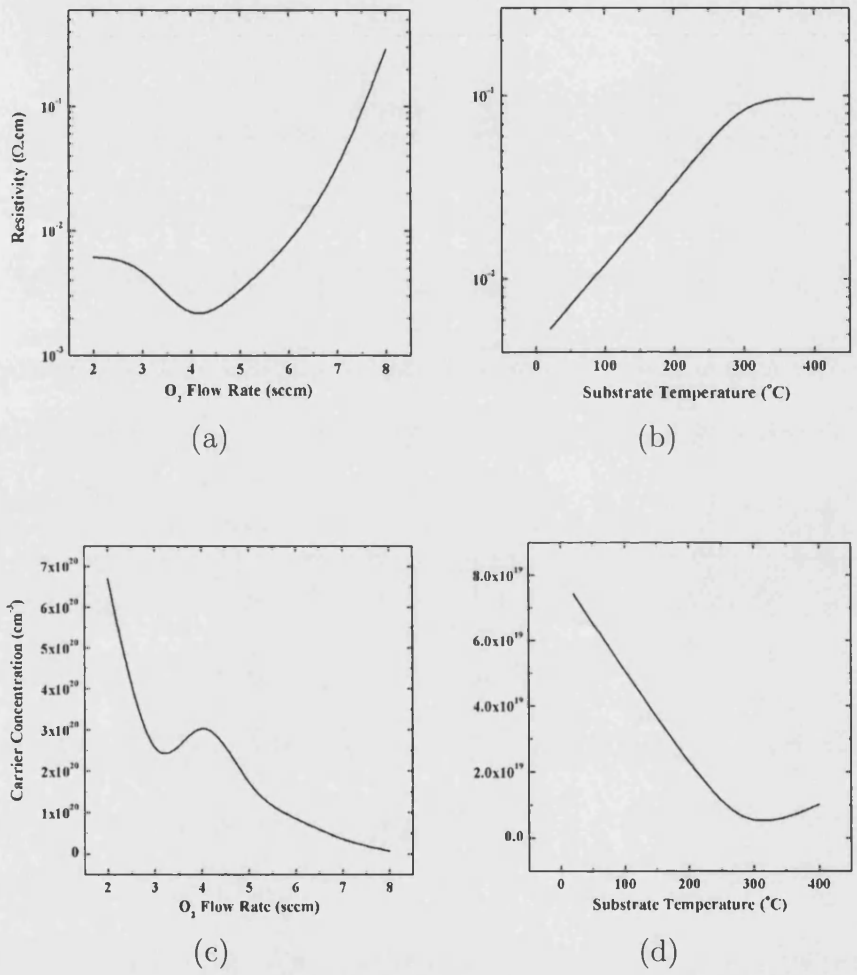

(a) (b)

(c) (d)

FIGURE 2.20: Effect of O_2 flow rate and substrate temperature on ZnO (a)(b) resistivity, and (c)(d) carrier concentration.

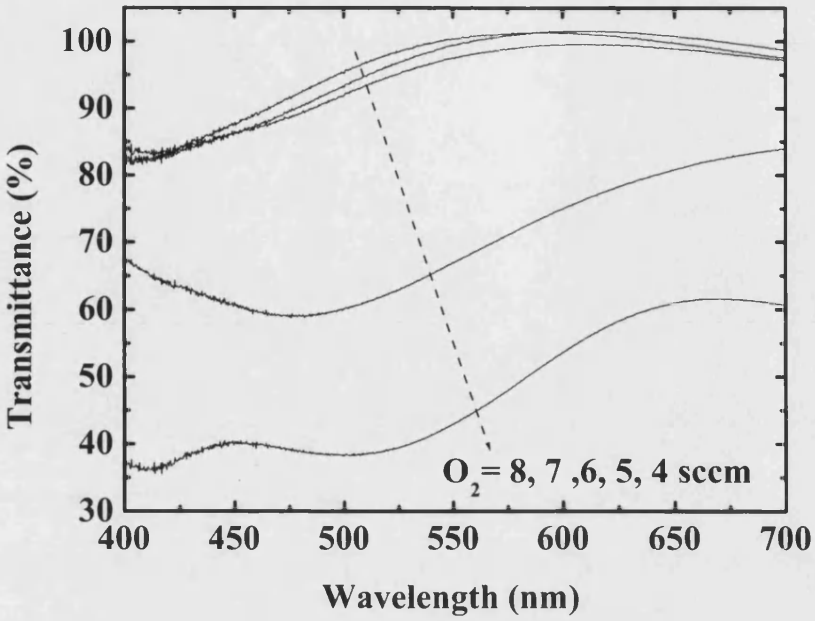

FIGURE 2.21: O_2 flow rate effect on the light transmittance.

Optical Properties

The degree of light transmittance for ZnO [O_2 = 4 – 8 sccm] is shown in Figure 2.21. It can be seen that the light transmittance factor is 40% at a wavelength of 475 nm. When the O_2 flow rate was increased to 5 sccm, the light transmittance was dramatically increased to 60% and 89% light transmittance was observed for ZnO [O_2 = 6 sccm]. These higher values are due to the improvement in homogeneity and stoichiometry of the films which reduce the degree of light scattering and absorption. A further increase of O_2 flow rate resulted in slightly improved light transmittance. The increase of substrate temperatures had little or no effect on light transmittance in the visible light range.

2.3.2 The Importance of Au in Ni/Au Contact

Introduction

According to the simulation results (see Section 2.2.1), the dominant factor for the light transmittance in Ni/Au contacts is the film thickness. In order to obtain a highly transparent contact with a more ohmic I-V characteristic performance, the Ni/Au layer in the Ni/Au/ZnO contact should be thin. Because the interface between p-GaN and Ni is the most important part for the contact, an investigation of the importance of the Au is necessary. If it has only a minor effect on the specific contact resistance and surface morphology, then this layer can be substituted.

Experiment

The Mg-doped p-type GaN was grown on (0001) sapphire substrates using a MOCVD method. Hall measurements showed that the hole concentration and mobility is 1.4×10^{17} cm^{-3}, and 11 $cm^2/V\cdot s$. The CTLM was used to measure the specific contact resistance. The circular pattern was designed with a central contact dot, the radius of which was 150 μm and the gaps between the dot and outer contact were 10, 14, 19, 25, 32, 40, 52, 70, and 100 μm.

Prior to deposition of the metal film, the samples were treated with KOH for 1 min to remove the natural contamination layer. A Ni film (18nm) was coated using a thermal evaporation system at 3×10^{-6} torr, and the samples were then divided into two in order to undergo different processes. Sample A (Figure 2.22a) was annealed at 500 ^oC in high vacuum ($\sim3\times$ 10^{-7} torr) for 10 minutes and then coated with a Au film (18nm). Sample B (Figure 2.22b) was coated with a Au film (18nm) and then annealed at 500 ^oC in high vacuum for 10 minutes. The CTLM patterns were defined by photolithography and a lift-off process. I-V measurements were performed using a KEITHLEY 238 high current source measurement unit. AFM was used for the observation of surface morphology and for the measurement of the thickness of the metal films.

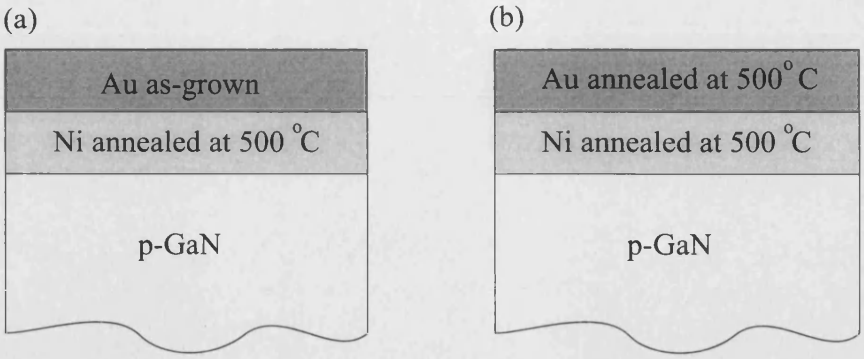

FIGURE 2.22: The structure of samples used in the study of the importance of Au in Ni/Au contacts.

Results and Discussion

The specific contact resistances of samples A and B were measured to be 0.53 $\Omega \cdot$ cm^2 and 0.15 $\Omega \cdot$cm^2, respectively. This result indicates the importance of Au for lowering the specific contact resistance. Chen *et al.* [65] have investigated a Ni/Au and Ni/Pt contact on p-GaN and a similar result was observed. The Ni/Pt showed much higher specific contact resistance than Ni/Au after annealing at 500 ^{o}C in oxygen for 10 minutes.

Figure 2.23 shows the AFM images for the Ni film annealed at 500 ^{o}C for 10 minutes (Figure 2.23a) and for the Au film deposited on this Ni film (Figure 2.23b). It is seen that the Ni grains grew from the average size of 20 nm (Figure 2.13a) to 100 nm. The surface has regular shaped grains with an average height of 5 nm and an average diameter of 100 nm. After the Au film was deposited on the top of this annealed Ni film (Figure 2.23b), the grain boundaries became partially filled by Au and consequently the RMS surface roughness was smoothed from 5.384 nm to 3.197 nm. The surface morphology is clearly seen to be significantly affected by the presence of Au. Figure 2.13c and Figure 2.23a show the dramatic difference. During annealing, the single Ni film transforms to regular larger grains (Figure 2.23a), but in the case of Ni/Au film the Au diffuses into the Ni film via the grain boundaries and then it results in the growth of larger irregular grains (Figure 2.13c).

According to the band diagram (Figure 2.7), the barrier height is dependent on

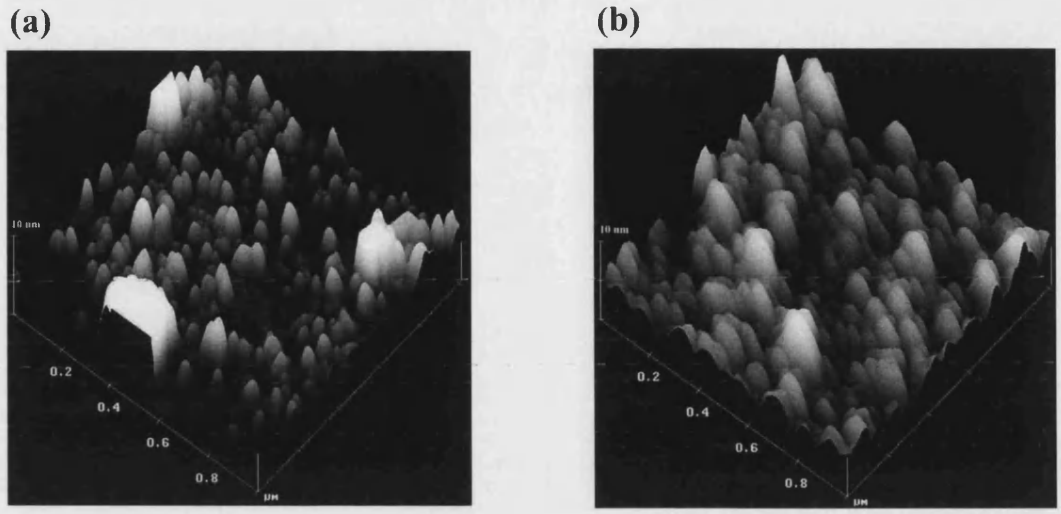

FIGURE 2.23: AFM images for (a) Ni annealed at 500 °C and (b) Au film deposited on this annealed Ni film.

the work function of the metal if no surface states are generated by the annealing process. Many reports showed that the Au in a Ni/Au contact can diffuse through the Ni film and then reach the p-GaN surface. In this experiment, there are no gases involved in the annealing process. The lower specific contact resistance in the Ni/Au contact may be due to modification of the p-GaN surface caused by Au diffusion. Ho *et al.* [38] have demonstrated the formation of GaAu alloy after annealing a Ni/Au contact on p-GaN. This reaction may generate gallium vacancies, which can act as acceptors for the p-GaN. Consequently, a p^+-GaN layer is formed between the Ni/Au contact and p-GaN and then the thickness of depletion layer is reduced. More acceptors can tunnel through the barrier, subsequently lowering the specific contact resistance.

In summary, the presence of Au in a Ni/Au contact for p-GaN is important in order to lower the specific contact resistance and modify surface morphology. The only means for increasing light transmission through a Ni/Au film is to reduce the film thickness.

2.3.3 Ni/Au/ZnO Contact for p-GaN

Introduction

An investigation of the ZnO film growth demonstrates a high value for light transmittance (90%) with a reasonable resistivity (1.6×10^{-3} Ω·cm). Because the Ni/Au contact has to be annealed in order to obtain a lower specific contact resistance, there are two methods for the fabrication of the Ni/Au/ZnO electrode. The first method is to anneal Ni/Au/ZnO layers at 500 °C for 5 minutes in N_2. One quick examination of this method was conducted. Figure 2.24 is the SEM picture of the film. It is apparent that the ZnO film was cracked after annealing. In comparison with the annealed Ni/Au film (see Section 2.2.5), the morphology has been changed dramatically and rounded grains with a typical size 20 nm were formed. Hence, this formation of rough surface will crack the ZnO film on the top of the Ni/Au film. The alternative method is to first anneal the Ni/Au contact and then deposit ZnO film on this annealed Ni/Au contact. The following experiment is based on this process for the fabrication of Ni/Au/ZnO electrode for p-GaN.

Experiment

Ni/Au = 5nm/5nm was deposited on p-GaN by thermal evaporation. According to the Hall measurement, the electron concentration and Hall mobility of this p-GaN was 2.2×10^{17} cm^{-3} and 11 $cm^2/V\cdot s$, respectively. The specific contact resistance measurement was based on the circular transmission line method (CTLM). After annealing at 500 °C for 5 minutes in N_2, unintentional doped ZnO film was deposited on the top of the Ni/Au. The deposition condition is listed in Table 2.2. The O_2 flow rate of 6 sccm was chosen specifically because a low resistivity (7.7×10^{-3} Ω·cm) and a high transmittance (90%) have been achieved for this condition.

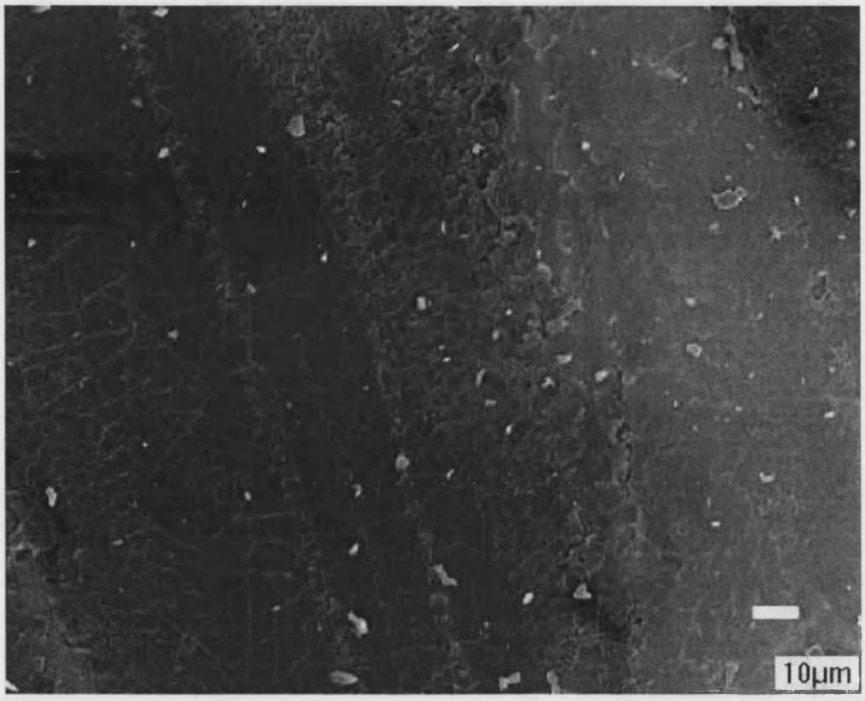

FIGURE 2.24: SEM picture of the Ni/Au/ZnO film annealed at 500 °C for 5 minutes in N_2. Note the cracking in the film.

Parameter	Value
RF Power	140W
Ar Flow Rate (Ion Gun)	50 sccm
Chamber Pressure	2.1×10^{-4} Torr
Screen Grid Voltage	500V
Accelerator Grid Voltage	300V
O_2 Flow Rate	6 sccm
Substrate Temperature	20 °C

TABLE 2.2: ZnO growth condition for the Ni/Au/ZnO electrode.

Results and Discussion

The surface of the Ni/Au/ZnO film showed no cracking when using the process described above; indicating the feasibility of its application to light emitting devices.

The specific contact resistance for the Ni/Au and Ni/Au/ZnO was 1.19×10^{-2} $\Omega\cdot$ cm^2 and 4.81×10^{-2} $\Omega\cdot$cm^2. The measured increased in the specific contact resistance of the Ni/Au/ZnO contact after the ZnO film deposition may be due to physical degradation of the Ni/Au film. This is possibly caused by secondary sputtering during the deposition of the ZnO film. Most of the ZnO particles are formed by the reaction of sputtered zinc particles and oxygen before deposition on to the sample. After formation, the ZnO particles still have sufficient kinetic energy to significantly bombard the Ni/Au surface, consequently some of the Ni/Au film may be sputtered out, partially modifying the surface.

Figure 2.25 shows the simulated and experimental results for Ni/Au and Ni/Au/ZnO films. Note that the transmittance scale has been adjusted for the simulated results in order to demonstrate the close similarity of the simulation data. The simulated transmittance for as-grown Ni/Au films was measured to be 57% at a wavelength of 470nm (Figure 2.25(a)), whereas the measured optical transmittance for the annealed Ni/Au film was 75%, as represented in Figure 2.25(b). This increase is mainly due to the change of the surface morphology. After one ZnO layer was deposited on the annealed Ni/Au, the light transmittance increased to 90%, shown in Figure 2.25(d). According to the simulation the improvement made by the addition of the ZnO film was a 20% increase in the transmittance. However, we actually achieved a 15% improvement in light transmission with our device. It should be noted that the simulation assumed uniform films of Ni/Au on the p-GaN.

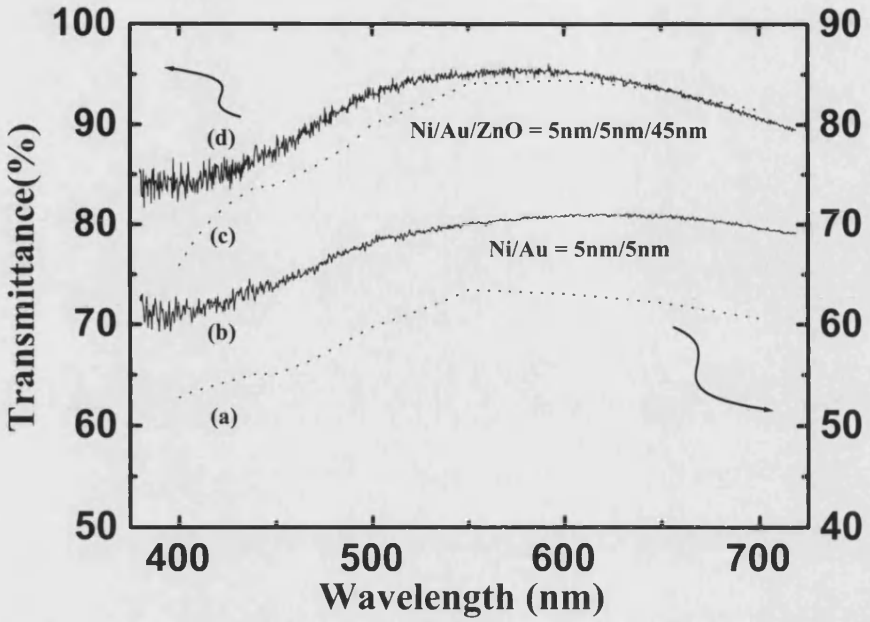

FIGURE 2.25: Light transmittance of (a) simulated Ni/Au = 5/5nm, (b) experimental data of Ni/Au=5/5nm, (c) simulated Ni/Au/ZnO = 5/5/45nm, and (d) experimental data of Ni/Au/ZnO = 5/5/45nm. Note that the dot lines are the simulated data.

2.4 Summary

The mechanism of the increased light transmission for the annealed Ni/Au contact was investigated by optical simulation and by experiment. It was found that the thickness of Ni/Au(5nm/5nm) film is too thin to have the interference in the visible light range, indicating that the dominant factor in the light transmission is the absorption, which depends on the thickness of the films. The observation of surface morphology showed the formation of open areas after annealing due to the formation of Ni/Au island structure. According to these results, it implies that the reason for the transparency could be attributed to the island structure that was formed after annealing and which then left open areas allowing light to pass.

The importance of the presence of Au presence in a Ni/Au contact for a p-GaN

has been studied by vacuum annealing. The specific contact resistance for the sample in which the Ni/Au film was annealed together was measured to be 0.15 $\Omega \cdot cm^2$. For the sample in which one Ni film was deposited on the GaN film, and then annealed, and subsequently one Au film was deposited on this Ni film, the specific contact resistance was measured to be 0.53 $\Omega \cdot cm^2$. Because the difference for these two sets of samples was the diffusion of Au, it indicated that the lower specific contact resistance of the first sample may be attributed to the presence of Au during annealing.

The study of ZnO growth, by means of an argon ion beam sputtering and a Zn metallic target in an oxygen-rich ambient, has been undertaken because it is potentially a good material with which to fabricate conductive and transparent electrodes. The effect of substrate temperature and O_2 flow rate on the structural, electrical and optical properties of ZnO has been investigated. The preferred (002) orientation was found for the ZnO film grown at O_2 flow rates higher than 3 sccm. For the ZnO films grown at the oxygen flow rate less than 4 sccm, the Zn atomic content is higher than 50%, indicating the formation of Zn-rich film. The XRD spectra for the ZnO films grown at different substrate temperature showed that the intensity of the ZnO (002) peak for the film grown at 400 ^oC was $\sim$30 times higher than that grown at room temperature, demonstrating the better crystallinity obtained at high temperature. It is consistent to the diffraction patterns. The FWHM of XRD spectra showed little difference for the ZnO films grown in the O_2 flow rates above 5 sccm, indicating a minor effect on the grain size. The Hall measurement showed that the ZnO films were n-type semiconductors, and the lowest resistivity of 1.6×10^{-3} $\Omega \cdot cm$ was obtained at an O_2 flow rate of 4 sccm. Any increase in substrate temperature during deposition resulted in a higher resistivity. Light transmittance measurements showed little dependance on substrate temperature, whereas an O_2 flow rate in the range of 2 – 5 sccm demonstrated a strong influence.

A highly transparent Ni/Au/ZnO electrode has been fabricated and characterised. The light transmittance was 87% – 90% at a wavelengths in the range 450nm – 500nm. The improvement of the light extraction is 15% compared with a Ni/Au contact. Slight contact degradation was observed, which may be attributed to the secondary sputtering of the Ni/Au contact during the ZnO layer deposition.

References

[1] J. K. Sheu, U. K. Su, G. C. Chi, W. C. Chen, C. Y. Chen, C. N. Huang, J. M. Hong, Y. C. Yu, C. W. Wang, and E. K. Lin, *J. Appl. Phys.* **83**, 3172 (1998).

[2] S. M. Sze, *Physics of Semiconductor Devices*, **2**nd edition(John Wiley & Sons, Inc., Canada, 1981).

[3] G. S. Marlow, and M. B. Das, *Solid State Electron.* **25**, 91 (1981).

[4] G. K. Reeves, *Solid State Electron.* **23**, 487 (1980).

[5] S. J. Pearton, GaN and Related Materials(Gordon and Breach Science Publishers, UK, 1997), p.p185.

[6] N. Koide, H. Kato, M. Sassa, S. Yamasaki, K. Manabe, M. Hashimoto, H. Amano, K. Hiramatsu, and I. Akasaki, *J. Cryst. Growth* **115**, 639 (1991).

[7] M. Hansen, P. Fini, L. Zhao, A. C. Abare, L. A. Coldren, J. S. Speck, and S. P. DenBaars, *Appl. Phys. Lett.* **76**, 529 (1999).

[8] S. Nakamura, M. Senoh, and T Mukai, *Appl. Phys. Lett.* **62**, 2390 (1993).

[9] W. Götz, N. M. Johnson, J. Walker, D. P. Bour, and R. A. Street , *Appl. Phys. Lett.* **68**, 667 (1996).

[10] Yasuo Koide, H. Ishikawa, S. Kobayashi, S. Yamasaki, S. Nagai, J. Umezaki, M. Koike, and Masanori Murakami, *Appl. Surf. Sci.* **117/118**, 373 (1997).

[11] S. Nakamura, T. Mukai, and M. Senoh, *Appl. Phys. Lett.* **64**, 1687 (1994).

[12] H. Ishikawa, S. Kobayashi, Y. Koide, S. Yamasaki, S. Nagai, J. Umezaki, M. Koike, and M. Murakami, *J. Appl. Phys.* **81**, 1315 (1997).

[13] Chul Huh, Sang-Woo Kim, Hyun-Min Kim, Dong-Joon Kim, and Seong-Ju Parka, *Appl. Phys. Lett.* **78**, 1942 (2001).

[14] T. Kim, J. Kim, S. Chae, and T. Kim, *Mater. Res. Soc. Symp. Proc.* **468**,427 (1997).

[15] Masaaki Suzuki, T. Kawakami, T. Arai, S. Kobayashi, Yasuo Koide, T. Uemura ,N. Shibata, Masanori Murakami, *Appl. Phys. Lett.* **74**, 275 (1999).

[16] Ja-Soon Jang, In-Sik Chang, Han-Ki Kim, Tae-Yeon Seong, Seonghoon Lee, and Seong-Ju Park, *Appl. Phys. Lett.* **74**, 70 (1999).

[17] I. S. Grant, and W. R. Phillipes, *Electromagnetism*, **2**nd edition (John Wiley & Sons Ltd, England, 1975), Ch.11.

[18] D. J. King, L. Zhang, J. C. Ramer, S. D. Hersee, and L. F. Lester, *Mater. Res. Soc. Symp. Proc.* **468**, 421 (1997).

[19] J. K. Sheu ,Y. K. Su, G. C. Chi, P. L. Koh, M. J. Jou, C. M. Chang, C. C. Liu, and W. C. Hung, *Appl. Phys. Lett.* **74**, 2340 (1999).

[20] G. Yu, G. Wang, H. Ishikawa, M. Umeno, T. Soga, T. Egawa, J. Watanabe, and T. Jimbo, *Appl. Phys. Lett.* **70**, 3209 (1997).

[21] O. Ambacher, W. Rieger, P. Ansmann, H. Angerer, T.D. Moustakas, and M. Stutzman, *Sol. State Commun.* **97**, 365 (1996).

[22] E. Dumont, B. Dugnoille, and S. Bienfait, *Thin Solid Films* **353**, 93 (1999).

[23] T. Nagase, T. Ooie, and J. Sakakibra, *Thin Solid Films* **357**, 151 (1999).

[24] C. R. Gorla, N. W. Emanetoglu, S. Liang, W. E. Mayo, Y. Lua, M. Wraback, and H. Shen, *J. Appl. Phys.* **85**, 2595 (1998).

[25] E. M. Bachari, G. Baud, S. Ben Amor, and M. Jacquet, *Thin Solid Film* **349**, 165 (1999).

[26] Jin Ma, Feng Ji, Hong-lei Ma, and Shu-ying Li, *Solar Energy Materials & Solar Cells* **60**, 341 (2000).

[27] Fumiyasu Oba, Shigeto R. Nishitani, Seiji Isotani, Hirohiko Adachi,and Isao Tanaka, *J. Appl. Phys.* **90**, 824 (2001).

[28] C. I. Wu and A. Kahn, *Appl. Surf. Sci.* **162-163**, 250 (2000).

[29] B. P. Luther, S. E. Mohney, and T. N. Jackson, *Semicond. Sci. Technol.* **13**, 1332 (1998).

[30] P. Ruterana, G. Nouet, T. Kehagias, P. Komninou, T. Karakostas, M. A. D. Poisson, G. Huet, and H. Morkoç, *Physica Status Solidi A - Applied Research* **176**, 767 (1999).

[31] D. R. Lide (ed.), *Chemical Rubber Company Handbook of Chemistry and Physics*, **77**th edition (CRC Press, USA, 1996.).

[32] A. Zeitouny, M. Eizenberg, S. J. Pearton, and F. Ren, *Mat. Sci. & Eng. B* **59**, 358 (1999).

[33] X. A. Cao, S. J. Pearton, S. M. Donovan, C. R. Abernathy, G. Ren, J. C. Zolper, M. W. Cole, A. Zeitouny, M. Eizenberg, R. J. Shul, and A. G. Baca, *Mat. Sci. & Eng. B* **59**, 362 (1999).

[34] C. F. Lin, H. C. Cheng, and G. C. Chi, *Solid-State Electronics* **44**, 757 (2000).

[35] C. B. Vartuli, S. J. Pearton, C. R. Abernathy, J. D. MacKenzie, E. S. Lambers, and J. C. Zolper, *J. Vac. Sci. Technol. B* **14**, 3523 (1996).

[36] J. Burm, K. Chu, W. A. Davis, and U. J. Schaff, *Appl. Phys. Lett.* **70**, 464 (1997).

[37] D. Qiao, Z. F. Guan, J. Carlton, and S. S. Lau, *Appl. Phys. Lett.* **74**, 2652 (1999).

[38] J. K. Ho, C. S. Jong, C. C. Chiu, C. N. Haung, K. K. Chih, L. C. Chen, F. R. Chen, and J. J. Kai, *J. Appl. Phys.* **86**, 4491 (1999).

[39] L. C. Chen, F. R. Chen, J. J. Kai, L. Chang, J. K. Ho, C. S. Jong, C. C. Chiu, C. N. Huang, C. Y. Chen, and K. K. Shih, *J. Appl. Phys.* **86**, 3826 (1999).

[40] J. C. Jan, K. Asokan, J. W. Chiou, W. F. Pong, P. K. Tseng, M. H. Tsai, Y. K. Chang, Y. Y. Chen, J. F. Lee, J. S. Wu, H. J. Lin, C. T. Chen, L. C. Chen, F. R. Chen, and J. K. Ho, *Appl. Phys. Lett.* **78**, 2718 (2001).

[41] S. Nakamura, N. Iwasa, M. Senoh, and T. Mukai, *Jpn. J. Appl. Phys.* **31**, 1258 (1992).

[42] P. Kozodoy, H. Xing, S. P. Denbaars, U. K. Mishra, A. Saxler, R. Perrin, S. Elhamri, and W. C. Mitchel, *J. Appl. Phys.* **87**, 1832 (200).

[43] A. K. Fung, J. E. Borton, M. I. Nathan, J. M. van Hove, R. Hickman II, P. P. Chow, and A. M. Wowchak, *J. Electron. Mater.* **28**, 572 (1999).

[44] H. Ishikawa, S. Kobayashi, Y. Koide, S. Yamasaki, S. Nagai, J. Umezaki, M. Koike, and M. Murakami, *J. Appl. Phys.* **81**, 1315 (1997).

[45] J. K. Kim, J. L. Lee, J. W. Lee, H. E. Shin, Y. J. Park, and T. Kim, *Appl. Phys. Lett.* **73**, 2953 (1998).

[46] J. L. Lee, J. K. Kim, J. W. Lee, Y. J. Park, and T. Kim, *Solid-State Electronics* **43**, 435 (1999).

[47] J. S. Jang, and T. Y. Seong, *Appl. Phys. Lett.* **76**, 2743 (2000).

[48] P. Sporken, C. Silien, F. Malengreau, K. Grigorov, R. Caudano, F. J. Sánchez, E. Calleja, E. Muoz, B. Beaumont, and P. Gibart, *MRS Internet J. Nitride Semicond. Res.* **2**, 23(1997).

[49] Y. Park, V. Choong, Y. Gao, B. R. Hsieh, and C. W. Tang, *Appl. Phys. Lett.* **68**, 2699 (1996).

[50] C. Huh, S. W. Kim, H. M. Kim, D. J. Kim, and S. J. Park, *Appl. Phys. Lett.* **78**, 1942 (2001).

[51] K. Kumakura, T. Makimoto, and N. Kobayashi, *Appl. Phys. Lett.* **79**, 2588 (2001).

[52] J. G. E. Gardeniers, Z. M. Rittersma, and G. J. Burger, *J. Appl. Phys.* **83**, 7844 (1998).

[53] Ji-Myon Lee,Ki-Myung Chang,Kyoung-Kook Kim,Won-Kook Choi, and Seong-Ju Parka, *J. Electrochemical Soc.* **148**, G1 (2001).

[54] D. Dimova-Malinovska, N. Tzenov, M. Tzolov, and L. Vassilev, *Mat. Sci. & Eng. B* **52**, 59 (1998).

[55] A. Gulino, and I. Fragala, *Chemistry Of Materials* **14**, 116 (2002).

[56] T. Yamamoto, and H. Katayama-Yoshida, *Jpn. J. Appl. Phys. Pt.2* **38**, L166 (1999).

[57] M. Joseph, H. Tabata, and T. Kawai, *Jpn. J. Appl. Phys.* **38**, L1205 (1999).

[58] T. Aoki, Y. Hatanaka, and D. C. Look, *Appl. Phys. Lett.* **76**, 3257 (2000).

[59] K. H. Kim, K. C. Park, and D. Y. Ma, *J. Appl. Phys.* **81**, 7764 (1997).

[60] F. Quaranta, A. Valentini, F. R. Rizzi, and G. Casamassima, *J. Appl. Phys.* **74**, 244 (1993).

[61] A. Valentini, F. Quaranta, M. Penza, and F. R. Rizzi, *J. Appl. Phys.* **73**, 1143 (1993).

[62] G. Xiong, J. Wilkinson, B. Mischuck, S. Tüzemen, K. B. Ucer, and R. T. Williams, *Appl. Phys. Lett.* **80**, 1195 (2002).

[63] T. K. Subramanyam, B. S. Naidu, and S. Uthanna, *Cryst. Res. Technol.* **34**, 981 (1999).

[64] Y. J. Kim, Y. T. Kim, H. K. Yang, J. C. Park, J. I. Han, Y. E. Lee, and H. H. Kim, J. *Vac. Sci. Technol. A* **15**, 1103 (1997).

[65] L. C. Chen, J. K. Ho, C. S. Jong, C. C. Chiu, K. K. Shih, F. R. Chen, J. J. Kai, and L. Chang, *Appl. Phys. Lett.* **76**, 3703 (2000).

[66] Software *Essential Macleod 8.5c* (Thin Film Center Inc., USA, 2002).

Chapter 3

ICP Etching of III-Nitrides

3.1 Introduction

Plasma etching is a commonly used technique for patterning semiconductors because it gives more control for etching profiles than wet etching and has been widely used since the 1960s [1]. A plasma is an ionised gas with equal numbers of free positive and negative charges. The ionisation process is mainly due to collisions between electrons and neutral gas atoms/molecules forming ionised atoms/molecules . The kinetic energy of electrons arises from the electric field or the collisions with other particles. Because the generated ions are more reactive than neutral radicals they can be used as etchants for materials.

Several etching techniques, such as reactive ion etching (RIE) [2], electron cyclotron resonance (ECR) etching [3], and inductively couple plasma (ICP) [5] etching have been developed for patterning group III-nitride materials. Because group III-nitrides have very high bonding energy, 11.52 eV for AlN, 8.92 eV for GaN, and 7.72 eV for InN [4], highly reactive ions with high concentration is desirable. In RIE, power is applied to the substrate, at Radio Frequencies (RF), usually at 13.56 MHz, to generate the plasma. Materials are etched by the chemical and physical interactions between the plasma and the target. The ion density in a RIE system is $\sim 10^9$ cm^{-3} [5]. The RF power maintains the plasma and in-

duces an electric field toward to the substrate, resulting ion bombardment of the target material. Hence, the plasma density and ion bombardment energy is dependent on the RF power. The increase in the plasma density can be achieved by higher RF power, but the resultant higher ion bombardment energy may induce physical and chemical damage, far into the target material, therefore degrading the performance of the device. Hence the ion density and ion energy must be controlled separately to obtain the desired high etch rates with low etch-induced damage. ICP etchers offer nearly independent control for ion flux and ion energy, and the ion density in an ICP system is usually $\sim 10^{11}$ cm^{-3} [5], which is 100 times higher than that of RIE. The dissociation and ionisation efficiency of diatomic gases is much higher than for RIE [6]–[9]. Thus, higher etch rates, with lower bombardment energies and high anisotropic profiles, can be obtained in ICP etch systems. In addition, the ion sputtering yield in ICP systems is higher than for RIE because the operating pressure is within the range 1 – 10 mTorr, compared with 20 – 100 mTorr for RIE systems.

Shul *et al.* [10] first investigated the ICP etching of GaN in a $Cl_2/H_2/Ar$ plasma: an etch rate, for GaN, of 6875 Å/min was obtained. Subsequently, ICP etching of GaN in Cl_2/Ar, Cl_2/N_2 and Cl_2/BCl_3 plasmas has been reported [11]–[14]. Etch rates for GaN as high as 9800 Å/min with smooth and anisotropic profiles have been reported [11], whereas only 170 - 1050 Å/min can be achieved in a RIE etcher [15]–[20].

3.2 The ICP Etcher

Figure 3.1 shows a diagram of the ICP etching unit that was used in this study. The RF power applied to the stage generates an electric field in the z-direction, while RF power applied to the ICP coil generates a magnetic field in the z-direction. A plasma is generated and maintained by either the electric field (RIE mode) or magnetic field, or in the case of the ICP mode, by both.

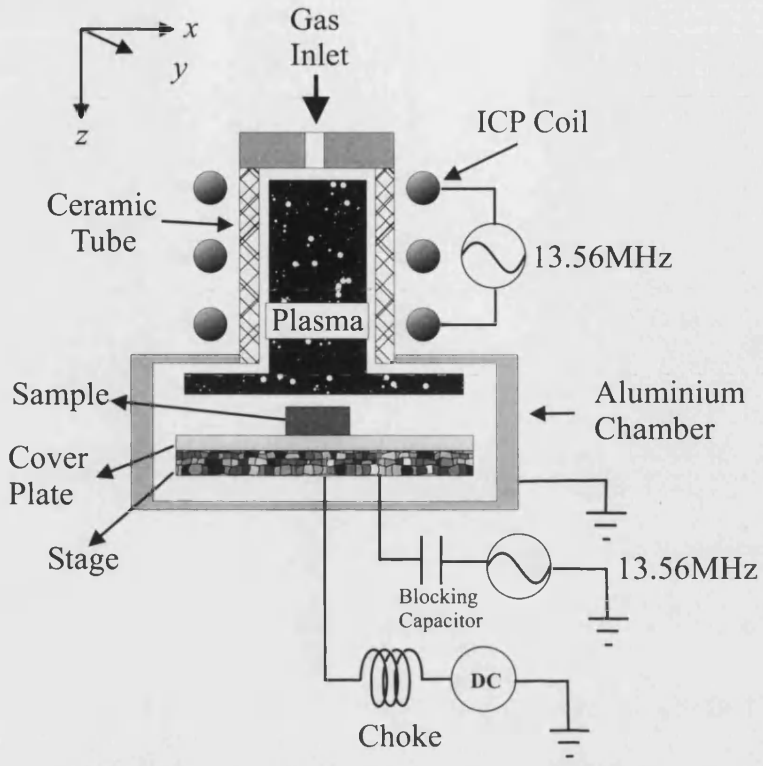

FIGURE 3.1: Schematic of an ICP etching unit.

3.3 Basic Plasma Physics

The collisions of the species inside a plasma determine the characteristics of the plasma. The basic physics including the possible collisions and the motion of a single charge particle is described below.

3.3.1 Collisions of Particles in Plasma

To sustain the plasma the essential condition, according to the definition of a plasma, is to maintain the numbers of electrons and ions. The electrons and ions inside an etching reactor are mainly formed by collisions between electrons, ions and neutral gases.

Collision Frequency

Consider a particle moving with a speed v. If the cross section for interaction of this particle with fixed scatterers is $\mathbf{Q}$, then in a unit time the particle can be thought of as sweeping through a volume $v\mathbf{Q}$. If the number density of the scatterers within this volume of interaction is N, then the number of interactions which take place in a unit time is give by $Nv\mathbf{Q}$. This is the collision frequency ν,

$$\nu = v\mathbf{Q}N \tag{3.1}$$

Main Collision Processes

There are electrons, ions and neutral atoms and molecules inside the reactor, so all possible pair permutations have to be considered. However, some collisions are more important than others in the plasma environments:

Elastic Collisions

An elastic collision is a collision between two particles of mass m_1 and m_2 in which the total kinetic energy is conserved as well as the total momentum. According to these two conditions, the maximum energy transfer ratio, $\frac{4m_1m_2}{(m_1+m_2)^2}$, can be obtained [19]. Considering a collision between an electron and an atom. Because the mass of the electron is much smaller than that of the atom, the energy transfer is negligible; so the electrons just change direction without significantly changing speed. It implies that when the electrons are moving in an electric field, elastic collisions have the effect of restricting their velocity in the direction of the field.

Ionisation

This is the most important type of collision process in the plasma. In this process, a bound electron in an atom is ejected from that atom, producing a positive ion

and two electrons, *e.g.*,

$$e^- + M \rightarrow 2e^- + M^+$$

These two generated electrons can then be accelerated by an electric or a magnetic field and contribute to more ionisation processes. The plasma is generally maintained by this multiplication process.

Excitation

If a electron-atom collision takes place, and if a less dramatic energy transfer of energy to the bound electron, it would enable the electron to jump to a higher energy level within the atom with a corresponding quantum absorption energy. This process is called *excitation.* In an excitation process, the primary electron loses kinetic energy equal to the excitation potential and also may be deflected.

Relaxation

One of the most obvious features of a plasma to an observer is the plasma 'glow'. This glowing process is due to the relaxation, or de-excitation, of electronically excited atoms and molecules. Thus, the various species present in the plasma may be determined by the emitted spectrum.

Recombination

The recombination process is when an electron combines with a positive ion to form a neutral atom. There are three types of the recombination process.

(1) A third body takes part in the collision process to satisfy the conservation requirements of energy and momentum.
(2) An electron attaches to a neutral atom to form a negative ion. The negative ion then collides with a positive ion. Subsequently the electron transfers and two neutral atoms are formed.
(3) The excess energy in the recombination process is transferred to radiation.

Dissociation

The dissociation process is the breaking apart of a molecule. The reaction can be express as

$$e^- + AB \rightarrow e^- + A + B \tag{3.2}$$

3.3.2 Motion of Single Charged Particles

The motion of a single charged particle is mainly determined by the forces induced by electric or magnetic fields. Consider a particle of charge q, mass m, and velocity $\mathbf{v}$ situated in a static, uniform electric field $\mathbf{E}$, and a static, uniform magnetic field $\mathbf{B}$. Newton's second law can be expressed thus,

$$m\frac{\mathrm{d}\mathbf{v}}{\mathrm{d}t} = q\mathbf{E} + q\mathbf{v} \times \mathbf{B} \tag{3.3}$$

Assume the magnetic field $\mathbf{B}$ is only acting in the z-direction and the electric field $\mathbf{E}$ only acting in the y- and z- directions, and denote $\Omega = -\frac{qB_z}{m}$. Eq. 3.3 becomes [1]

$$\begin{bmatrix} \dot{v}_x \\ \dot{v}_y \\ \dot{v}_z \end{bmatrix} = \frac{q}{m}\begin{bmatrix} 0 \\ E_y \\ E_z \end{bmatrix} - \begin{bmatrix} v_y\Omega_z \\ -v_x\Omega_z \\ 0 \end{bmatrix} \tag{3.4}$$

Integrating Eq. 3.4 the velocity of the particle in each orthogonal direction is given by [1]

$$\begin{aligned} v_x &= \left(v_x^0 + \frac{qE_y}{m\Omega_z}\right)\cos\Omega_z t - v_y^0 \sin\Omega_z t - \frac{qE_y}{m\Omega_z} \\ v_y &= \left(v_x^0 + \frac{qE_y}{m\Omega_z}\right)\sin\Omega_z t + v_y^0 \cos\Omega_z t \end{aligned}$$

$$v_z = v_z^0 + \frac{q}{m} E_z t \tag{3.5}$$

where v_x^0, v_y^0 and v_z^0 are the initial velocities in the x-, y- and z-directions, respectively.

Case 1: Electric Field Only – RIE Etching

In the reactive ion etching, only an electric field in the z-direction is introduced to the reactor. Based on Eq. 3.5 the velocity of a single charged particle is given by

$$\begin{aligned} v_x &= v_x^0 \\ v_y &= v_x^0 \\ v_z &= v_z^0 + \frac{q}{m} E_z t \end{aligned} \tag{3.6}$$

It is seen that the particle motion only responds to the electric field E_z in the z-direction. The velocity in the x- and y-direction remains identical to the initial velocity. In the ionisation process, electrons gain the energy from the electric field only in the z-direction.

Case 2: Electric Field Parallel to Magnetic Field – ICP Etching

In the inductively-couple plasma etching, the electric field is parallel to the magnetic field, *e.g.*, $E_x = E_y = 0$. The velocity of a single charged particle, based on Eq. 3.5, is given by

$$\begin{aligned} v_x &= v_x^0 \cos \Omega_z t - v_y^0 \sin \Omega_z t \\ v_y &= v_x^0 \sin \Omega_z t + v_y^0 \cos \Omega_z t \\ v_z &= v_z^0 + \frac{q}{m} E_z t \end{aligned} \tag{3.7}$$

According to Eq. 3.1, Eq. 3.6, and Eq. 3.7, one can see that the collision frequency of charged particles in a space consisting of an electric and magnetic field is larger than that of a space consisting of only electric field because its velocity in x- and y-directions is larger. The higher collision frequency result in a higher plasma density in the ICP mode.

3.3.3 Electron and Ion Temperature

An operational definition of temperature is that it is a measure of the average translational kinetic energy associated with the disordered microscopic motion of particles. The ions in the plasma can only absorb a little energy from the electrons because the large difference in mass between them, so ion energies are determined by the collisions between other ions and neutral species. It implies that the concept of temperature is applicable for ions in the plasma and the kinetic energy (E_k)is given by

$$E_k = \frac{3}{2} k_B T \tag{3.8}$$

where k_B is Boltzmann constant and T is the temperature.

It is reasonable to apply the concept of temperature to the electrons in the plasma using the same form of Eq. 3.8 since the electron-electron collision results in a disordered microscopic motion.

3.3.4 Plasma Potential

Assuming that one small electrically isolated substrate is suspended in the plasma, then it will be initially struck by electrons and ions. Because of the higher speed of the electrons the current density of electrons impinging the substrate is much larger. Consequently the substrate immediately starts to build a negative charge and hence negative potential with respect to the plasma. Since the substrate is charged negatively, electrons are repelled and positive ions are

attracted. We can treat plasmas as conductors because of the large number of free electrons inside plasmas. It implies that plasmas are electric field free, similar to other conductors, *i.e.* metals; so the potential of the substrate is equal to the plasma potential (V_p). For an insulated substrate, a zero steady state net flux is required so the potential, or floating potential V_f, is relative to V_p. In the absence of a reference, only the potential difference $V_p - V_f$ is meaningful.

3.3.5 Sheath Formation

In the case described before, electrons can be repelled by the potential difference ($V_p - V_f$). It follows that the space between the substrate and the plasma acquires a net positive charge, resulting in a decrease in the electron density (Figure 3.2). The 'glowing' of the plasma originates from the relaxation of atoms excited by electron impact (see Section 3.3.1); thus the glowing intensity is lower in this space because of lower electron density, resulting in a characteristic darker area. This dark space is called the *sheath.* The potential difference, or sheath potential, can be obtained from Poisson's equation [19]:

$$\nabla^2 V = \frac{\mathrm{d}^2 V}{\mathrm{d}x^2} = -\frac{\rho}{\epsilon_0} \tag{3.9}$$

The ion energy in the vicinity of the substrate is then given by

$$E_{ion} = q(V_p - V_f) \tag{3.10}$$

3.3.6 Development of DC Bias of RF Electrodes

When the RF power applied to the stage is initially switched on the number of electrons collected during the positive half of the cycle is much greater than the number of ions collected during the negative half, because of the large difference in their masses. Thus the stage acquires a net negative charge through each cycle and an average negative voltage, which increases until charge capture is balanced

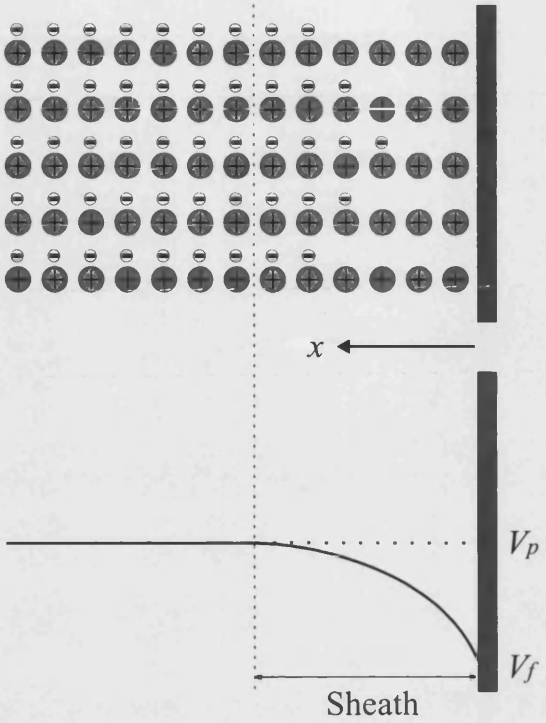

FIGURE 3.2: Schematic of a space charge sheath developed in front of a floating substrate.

through each RF cycle. This voltage is known as the DC bias. The voltage at the surface of the stage or sample is sinusoidal, offset by the DC bias. Electrons, being light, respond to the instantaneous potential, and are collected only during the small phase when the electrode potential nears the plasma potential. Ions, being relatively heavy, respond to the time averaged potential (DC bias) and are collected uniformly throughout the RF cycle.

This DC bias is measured by connecting a choke in series with the DC voltage meter. Note that a 7 mm thick quartz plate was placed on top of the stage because small samples are normally used to study etching behaviour and this quartz cover plate protects the stage from damage. This effectively introduces another capacitor into the circuit so that the DC bias voltage measured during experiments is not the voltage at the sample surface. A more accurate indication of the DC bias at the sample surface is given by removing the quartz cover plate, running the process briefly, and recording the stage DC bias, although of course the sample itself acts as a relatively small capacitor in the circuit.

The measured DC bias voltage represents the potential between the stage and ground. According to Eq. 3.10, the precise ion energy can be obtained by measuring the plasma potential referring to the ground and then minus the DC-bias. For a given plasma, the variation of plasma potential induced by changing the etch parameters is much lower than the substrate potential [29]. Therefore, the DC bias can be used as an indication of ion energy even if the plasma potential is not measured *in-situ*.

3.3.7 Etch Chemistry of Group III-Nitrides

Determination of the Etch Chemistry

The main consideration in selecting suitable etch chemicals is the nature of the etch products ,which are produced by the reactions between the reactive species and materials to be etched, and the reactivity between target materials and etchants. Table 3.1 lists the possible etch products from the reactions between halogen radicals and GaN, AlN and InN [4, 23]. It is seen that the boiling points of the possible etch products from the fluorine radical are ~1000 °C. Hence, the fluorine radical is not ideal for the etching of group III-nitrides. In contrast, the chlorine radical is attractive because of the low boiling points of the etching products (~200 °C). For bromine and iodine radicals, the boiling points of the etching products are in the range of 250 °C to 380 °C, and it is possible to sputter or evaporate quickly. In general, chlorine, bromine and iodine are used as the chemical radicals to etch group III-nitrides [5][24]. The following section will discuss ICP etching for group III-nitrides in Cl_2-based plasmas.

Species in Cl_2 Plasmas

Cl_2 is the gas most commonly used to etch III-nitrides. The dissociation and ionisation processes are described below.

Radicals	Etch Product	Melting Point(^{o}C)	Boiling Point(^{o}C)	Appearance
F	GaF_3	sublime 800	950	Crystalline Solid
	AlF_3	sublime 760	1275	Crystalline Solid
	InF_3	1170	>1200	Crystalline Solid
Cl	Ga_2Cl_6	78	201	Crystalline Solid
	$AlCl_3$	sublime 177.8	180	Crystalline Solid
	$InCl_3$	586, sublime 300	Volatile 600	Yellow Crystalline Solid
Br	$GaBr_3$	122	279	Crystalline Solid
	Al_2Br_6	97.5	255	Crystalline Solid
	InBr	285	656	Crystalline Solid
I	GaI_3	212	340	Crystalline Solid
	Al_2I_6	188.32	382	Solid
	InI_3	207	no data	Crystalline Solid

TABLE 3.1: The physical properties of possible etch products of AlN, GaN and InN reacting with F, Cl, Br and I radicals.

The dissociation and ionisation reactions of Cl_2 are

$$e^- + Cl_2 + 2.475eV \rightarrow 2Cl^{\cdot} + e^- \tag{3.11}$$

$$e^- + Cl_2 + 11.48eV \rightarrow Cl_2^+ + 2e^- \tag{3.12}$$

$$e^- + Cl^{\cdot} + 13.0eV \rightarrow Cl^+ + 2e^- \tag{3.13}$$

The dissociation energy of the reaction shown in Eq. (3.11) is 2.475 eV [21]. Ionisation energies in Eq. (3.12) and Eq. (3.13) are 11.48 eV and 13.0 eV, respectively [21]. Because of the higher ionisation energy in reaction Eq. (3.13), the higher power obtained in the ICP mode is required. Malyshev *et al.* [8] used a transformer-coupled plasma reactor for the measurement of ions and neutral species density. The ICP mode was achieved by applying the RF power to a transformer-coupled plasma antenna, while RIE mode is operated by applying the

RF power to the stage. The results gave the number density ratio of ions/radical $\left(\frac{Cl^{\cdot}}{Cl_2^+ + Cl^+}\right)$ ~1000 for a pressure of 2 – 10 mTorr in either RIE or ICP mode. For the number density of ion species, it was found that the dominant ion in the ICP mode is Cl^+, while Cl_2^+ is the dominant ion in the RIE mode [9]. According to Eq. 3.6 and Eq. 3.7, one can see that the kinetic energy of electrons in the ICP mode is higher than that in RIE mode. In addition, the collision frequency, based on Eq. 3.1, in the ICP mode is higher than that in the RIE mode. These facts result in a higher degree of dissociation and subsequently the ionisation for the dissociated $Cl^{\cdot}$ radicals in the ICP mode. Because the Cl^+ ions have higher reactivity than Cl_2^+ ions, it is expected that ICP etching can achieved a higher rate in chemical etching than that offered by RIE etching.

3.3.8 Redeposition of Etch Products

Ideally the etch products should be evaporated or sputtered and then pumped out from the chamber, or deposited on the chamber wall. However, for particles which accumulate in the vicinity of the sample surface it is possible that they redeposit themselves on the etch substrate, thus contaminating the sample surface. In this manner, redeposited etch products can act as a mask to obstruct further etching. In addition, the products will possibly contaminate the material surface and then affect either or both the contact adhesion and conductivity of a post-coated film. This has been a crucial issue in processing particularly with the reduction in physical size of devices.

The etch products may accumulate to form larger particles in the vicinity of the target material. The growth process follows the steps: [36]

(1) formation of clusters,
(2) growth to a critical nucleus size (~ 10 nm) by chemical vapour deposition or by cluster-cluster interactions,
(3) agglomeration of the nuclei.

The particles formed in the vicinity of the target materials are normally electric insulators. An electron with high energy in the sheath region can easily charge up

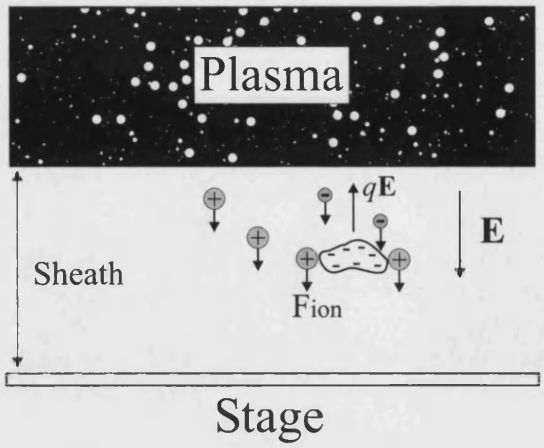

FIGURE 3.3: Illustration of electrical forces acting on a negative-charged particle.

the particles, resulting in negatively charged particles. They are usually charged to a level of several hundreds, to thousands, of negative elementary charges [34]. Figure 3.3 shows the possible forces acting on a negative-charged particle. The energy transfer of collisions between neutral species and the particle is small because the momentum of the neutral species is much smaller compared with that of ions. Since the particle will be trapped at the position where the net force $\mathbf{F}_{net}$ is zero, this condition is given by

$$\mathbf{F}_{net} \approx \Sigma \mathbf{F}_{ion} - \Sigma q\mathbf{E} \tag{3.14}$$

where $\mathbf{E}$ is the electric field in the sheath, which is induced by the sheath potential $(V_p - V_f)$, and $\Sigma \mathbf{F}_{ion}$ is the total ion drag force acting on the charged particles.

In ICP etching without applying RF power on the stage, the electric field in the sheath region is small. According to Eq. 3.14 the ion drag forces dominate the movement of the particles. Hence, the particles tend to be dragged down to the surface of the target materials, and subsequently contaminate the surface [37]. Applying sufficient RF power to the stage to increase the sheath potential can compensate the ion drag forces and then reduce the contamination [37].

3.4 ICP Etching Parameters

The densities and energies of reactive and inert species are a function of ICP power, RF power, chamber pressure, gas flow rates and concentrations, and species of additive gases. The following sections will discuss the influences of the parameters on the operation of the ICP etcher.

3.4.1 RF Power

According to the theories discussed before, the RF power applied to the stage contributes to the increase in the sheath potential, which then affects the ion bombardment energy. In the RIE mode, the electric field induced by the applied RF power maintains the plasma and the ion bombardment energy. In order to obtain higher plasma densities, a further increase in the RF power is required. However, this induces an increase in the ion bombardment energy, which may result in damage to the target materials.

3.4.2 ICP Power

According to Eq. 3.6, the electrons in the sheath region can be accelerated by this electric field. The electrons inside the plasma have very little response to the electric field because it can be treated as a conductor. When the ICP power is applied to the coil, it induces a magnetic field, which penetrates the plasma region. Eq. 3.7 has shown that the velocity of electrons have components in the x- and y-directions, indicating a higher collision frequency in the plasma region. It results in an increase of the ionisation processes, and thus increases the plasma density.

The stage voltage V_f is mainly dependent on the movement of electrons in the z-direction. According to Eq. 3.7, it is seen that the induced magnetic field only contributes to the x- and y-direction; so little effect on V_f is expected when the magnetic field is applied. It implies that the plasma density and the ion

bombardment energy can be effectively decoupled, which gives more control of the etching in both the vertical and horizontal direction.

3.4.3 Chamber Pressure

According to the ideal gas equation, chamber pressure is proportional to the number of species in the chamber, hence also the mean free path. The resulting effects are listed as follows:

(1) the sheath potential and energy of ions bombarding surface,
(2) the electron energy,
(3) the ion-to-neutral abundance ratio and fluxes of these species to surfaces,
(4) the relative rate of higher to lower order chemical kinetics,
(5) surface coverage by absorption,
(6) the relative rates of mass transport processes.

According to Eq. 3.9 the sheath potential is related to the charge density in the sheath region. The higher pressure results in a smaller mean free path. Because the electron density and energy is lower in the sheath region, the ionisation is not the dominant collision process. Instead, the recombination of ions and electrons is highly possible, resulting in a lower ion density in sheath region. This effect directly applies to the decrease of sheath potential. In the etching process, it implies that the etching mechanism is dominant by chemical reactions.

The electron energy is related to the electron speed. Because of the increase in the mean free path of neutral species at low pressure the collision frequency between them is reduced, resulting in a higher speed of electrons. Hence, the electron energy, or electron temperature, is increased. It is consistent with the measurement of electron temperature in an ICP reactor [38].

For low pressure, *e.g.*, 1 – 50 mTorr, the effects of (3) – (6) may be minor because high ion bombardment energy can contribute to the sputtering of species covered on the surface and the reaction between reactive ions and target materials is

much violent than that with neutral species.

3.5 ICP Etching for III-Nitrides LED

From published reports, previous studies of etching parameters for etch rate, DC bias, etching profile and surface roughness have been fragmented. A statistical experimental design is suitable for a more comprehensive study. Full factorial experimentation is frequently used to study the effects and interactions of important experimental parameters for the given levels. However, it is a time-consuming process when there are many factors involved. In order to minimise the number of tests, several methods of experimental design have been developed. In this study, the experimental design chosen was based on the Taguchi method [31]. The effect plots of etching parameters were then established. These plots enable comprehensive understanding of the etching parameter effects on etch rate, DC bias, etching profile and surface roughness.

3.5.1 Taguchi Method

G. Taguchi has developed a method which uses only a portion of the total number of possible tests to estimate the effect of the main variables and their possible interactions [31]. His method often gives the qualitative result required for the chosen parameters and levels. It assumes that the output of the experiment is continuous so that the optimum value can be obtained via statistical analysis. In this study, the outputs were chosen to be: Etch rate, DC bias, sidewall angle and surface roughness. According to published reports [11][12]–[14], these assumptions are reasonable.

The steps of Taguchi method are

(1) to identify the parameters,
(2) to identify the levels of each parameter,
(3) to select an appropriate orthogonal array (OA),
(4) to assign the parameters to columns of the OA,
(5) to analyse data and determine the optimum levels, and
(6) to confirm the optimum levels.

3.5.2 Experiment

The GaN LED structure used in this study was grown by MOCVD. After the nucleation process and buffer GaN growth, a 500 nm n-GaN, 10 nm InGaN, and 5 nm InGaN and 6 nm/9 nm $Al_{0.1}Ga_{0.9}N$/GaN superlattice was subsequently grown on the surface (Figure 3.4). A 260 nm-thick SiO_2 film which was patterned and used as the mask for GaN etching was then deposited on the GaN LED sample by ion beam sputtering. Standard photolithography and CHF_3/Ar plasma etching was employed to pattern the SiO_2 film. After the SiO_2 etching, wet cleaning and O_2 plasma dry cleaning were conducted to remove any fluorine residue. Subsequently, GaN etching was performed, based on the experimental layout gave in Table 3.3. After GaN etching, a stylus profilometer was used to measure the etch depth and surface roughness. The etch profile was evaluated by scanning electron microscopy (SEM), and the etch products were examined by XRD.

Based on a Taguchi experimental design, the etching parameters of RF power, ICP power, stage temperature, Cl_2 flow rate, Ar flow rate, and chamber pressure were chosen as the study factors. All factors contain two levels (Table 3.2). A two-level orthogonal matrix was employed in the experimental layout (Table 3.3). The etch rate, DC bias, sidewall angle and surface roughness were evaluated by effect plots of etching parameter.

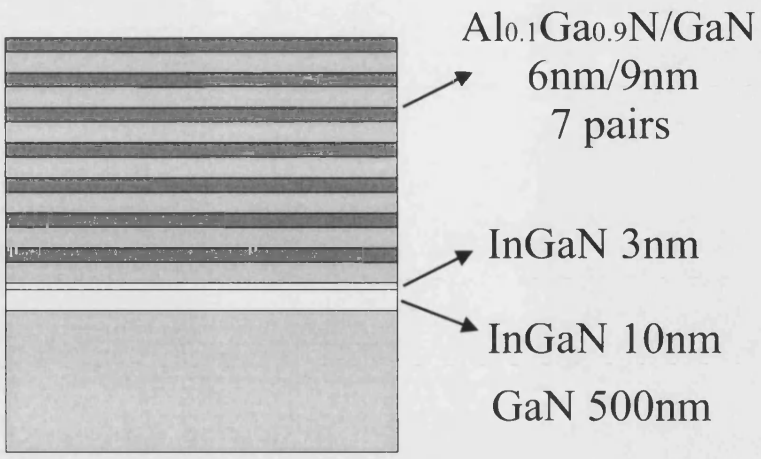

FIGURE 3.4: Schematic of the LED structure.

	Symbols and Parameters	Level 1	Level 2
A	RF Power (W)	150	300
B	ICP Power	300	500
C	Stage Temperature (°C)	20	50
D	Cl_2 Flow Rate (sccm)	20	30
E	Ar Flow Rate (sccm)	5	10
F	Chamber Pressure (mTorr)	9.5	15.5

TABLE 3.2: Parameters and levels used in this study.

No	A	B	C	D	E	F
1	150	300	20	20	5	9.5
2	150	300	20	30	10	15.5
3	150	500	50	20	5	15.5
4	150	500	50	30	10	9.5
5	300	300	50	20	10	9.5
6	300	300	50	30	5	15.5
7	300	500	20	20	10	15.5
8	300	500	20	30	5	9.5

TABLE 3.3: Experimental matrix for the investigation of ICP etching for GaN.

3.5.3 Results and Discussion

DC Bias

The effect plot of etch parameter for DC bias is demonstrated in Figure 3.5. It is obtained by the analysis of means. In this case, for example, the effect of RF power on the DC bias for level 1 (150W) is the average of DC bias for experiment No. 1 – 4, while the average of the DC bias for experiment No. 5 – 8 represents the effect of level 2 (300W). For RF power equal to 150W (level 1), experiment No. 1 – 4 consists of the same value RF power, but the other parameters mix level 1 and 2 in order to lower the contribution to the average of the etch rates. The difference of the average values of a given parameter represents the significance of this parameter. The analysis of other etch results follows the rules described above.

It is clear that RF power was the dominant parameter for the DC bias. The DC bias was increased from -298V for RF = 150W to -526V for RF = 300W. This result was consistent with theoretical predictions and other published experimental data [27].

ICP power, stage temperature, Cl_2/Ar flow rate and chamber pressure have only a small effect on the DC bias in the given level. The explanation of the ICP power effect can be seen in Section 3.4.2. Stage temperature in the given level cannot change the charge density in the sheath region. Cl_2/Ar flow rate may have little effect on the plasma potential, resulting in a minor effect on the DC bias. Chamber pressure at the given levels is very low and the difference is small, indicating the effect on the recombination processes in the sheath region may be minor.

Etch Rate of GaN

Figure 3.6 shows the effect plot of etching parameter for the etch rate. It shows that ICP power is the most significant parameter for this process. Consider the

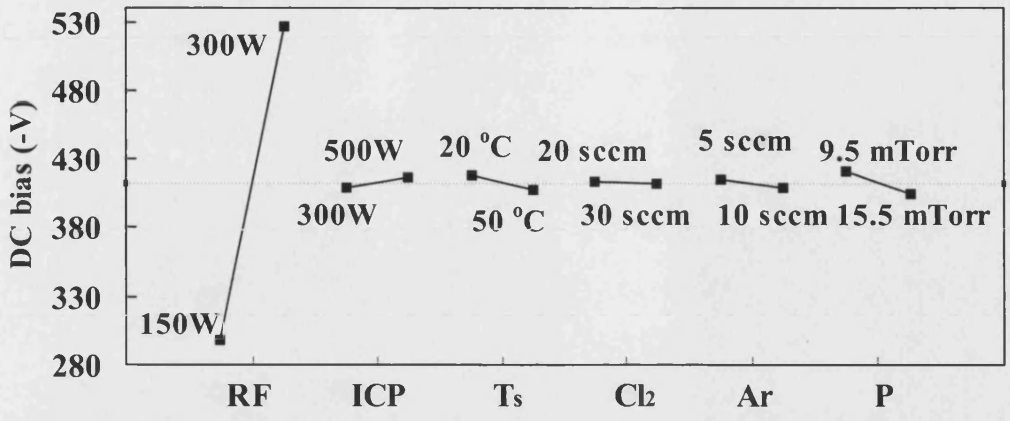

FIGURE 3.5: Effect plot of etch parameter versus DC bias.

effect of RF power, which contributes to the ion bombardment energy, on the etch rate. The etch rate of GaN is less sensitive to the change in RF power for the given levels. These two results suggest that the GaN etching is more sensitive to the increase in plasma density, indicating that the dominant etching mechanism is chemical reaction. A similar conclusion was drawn in ICl, IBr, and other Cl-based plasma ICP etching experiments [10, 11, 12, 26, 27].

RF power is the second most significant parameter on the etch rate of GaN – it affects the electric field in the sheath region. Hence, the ions, including Cl^+ and Ar^+, will be accelerated in this region. Ar^+ ions only contribute to the physical sputtering, while Cl^+ may react with the GaN on the surface. The condition for this reaction is that the time Cl^+ can stay on the surface must be longer than the chemical reaction. It has been found that the etch rate of GaN in the Ar^+ ion milling is $\sim$ 10 times lower than that in ICP etching [22]. Thus, the high etching rate is mainly from the chemical reaction between Cl^+ and GaN.

Chamber pressure had the same significance with RF power to the GaN etch rate. Because the etch rate of GaN is dominated by chemical reaction, indicating that the Cl^+ density in the plasma is important. Malyshev *et al.* [9] have measured the Cl^+ density over the pressure range 2 mTorr to 20 mTorr. It was found that the Cl^+ density remained nearly identical at the measuring pressure range. Thus, the

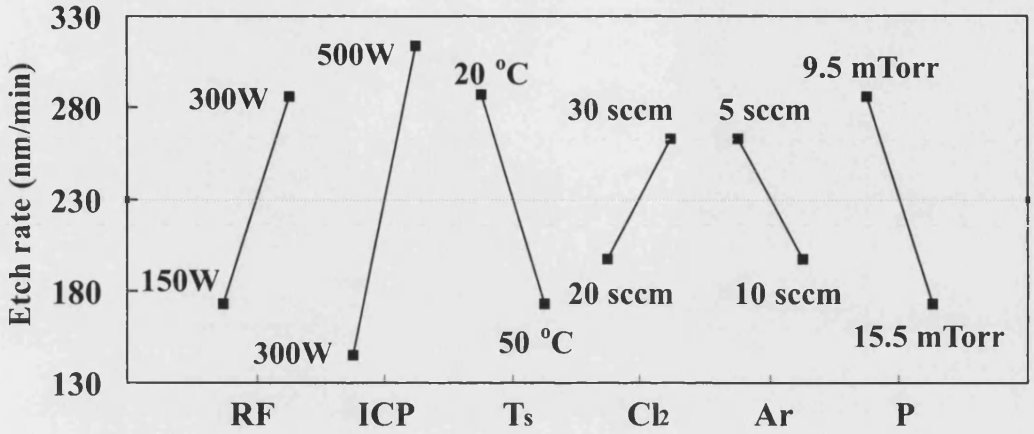

FIGURE 3.6: Effect plot of etch parameter versus etch rate.

higher etch rate at lower pressure found in this experiment may be not be directly related to the increase in the Cl^+ density. Sheu *et al.* [25] have found that the etch rate of GaN increased in the Cl_2/Ar plasma with an increase in the chamber pressure. This contradicts these results. Thus, the decrease in GaN etch rate at higher chamber pressure may be due to the redeposition of the etch products. At higher chamber pressure, the etch products may accumulate to form a cluster and then redeposit on the surface. These can act as micro-masks: preventing further etching. As a result of the process, a possible etch product was thought to be gallium chloride and sputtered SiO_2 particles by ions because a SiO_2 cover plate was used in this study. The specimen stage temperature is in the range 20 °C– 50 °C, which is not high enough to evaporate gallium chloride. Thus, the redeposition of gallium chloride is possible. One sample which was etched for 5 minutes was examined by XRD (Figure 3.7). The peak positions (1) – (3) were identified as beta gallium chloride (0 3 2), (2 1 $\bar{3}$) and (3 1 2), respectively. Higher stage temperatures may result in the growth of larger clusters, resulting in more extensive passivation of etching.

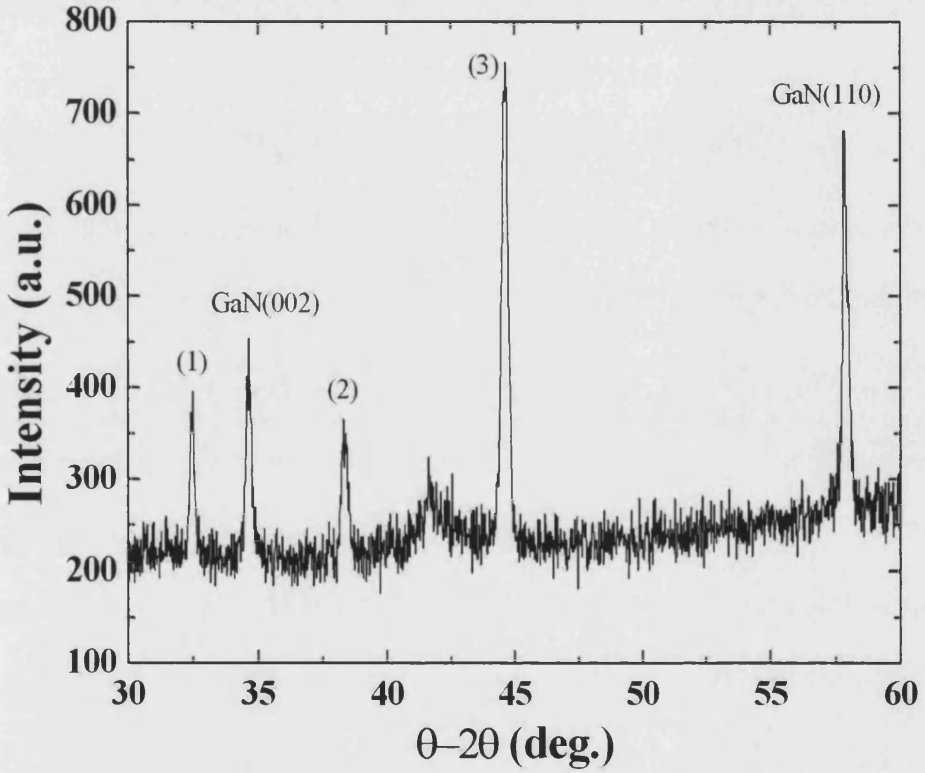

FIGURE 3.7: XRD spectrum of the GaN LED etched using the conditions listed in Table 3.5 for 5 minutes. The XRD peak (1), (2) and (3) are identified as beta gallium chloride (0 3 2), (2 1 $\bar{3}$) and (3 1 2), respectively.

Sidewall Angle

In order to achieve a high rate of anisotropic etching, the etch rate in the vertical direction has to be much higher than that of the transverse direction. High ion bombardment energy and the formation of inhibitors at the sidewall are possible mechanisms which enhance anisotropic etching. In this present study, the ion bombardment energy may be the most important factor for satisfactory vertical sidewall formation.

The effect plot of sidewall angle (Figure 3.8) shows that RF power was the most significant parameter for sidewall angle. It has been seen that the Cl^+ ions can contribute to the chemical etching in the z-direction. In addition, a higher velocity in the z-direction, based on Eq. 3.6, can be obtained by higher RF power. Hence, it is claimed that an increase in RF power results in an anisotropic etching.

Higher chamber pressure and lower stage temperatures degraded the anisotropic etching profile. This may well be due to the redeposition of etch products. Figure 3.9 shows the SEM pictures of these eight experiments. It is seen that lower RF power resulted in non-vertical sidewalls (Figure 3.9a –3.9d). The substrate temperature effect can be seen by comparing Figure 3.9a, 3.9b and Figure 3.9c, 3.9d which were etched at stage temperatures of 20 °C and 50 °C, respectively. The drag forces from neutral species in the vicinity of the sidewall may drag the etch products back to the sidewalls and then act as etching masks, inhibiting further etching of the sidewall.

Surface Roughness

High surface roughness is generated by a large difference in etch rate between the vertical and transverse directions. The large etch rate difference may be induced by using high RF power. In the plot of peak-to-peak surface roughness (Figure 3.10), the RF power was shown to be less significant. It can be deduced that the dominant factor for surface roughness was the redeposition of etch products. The size and quantity of etch products are the most important issues. The effect plot showed that the chamber pressure was the most significant parameter for surface

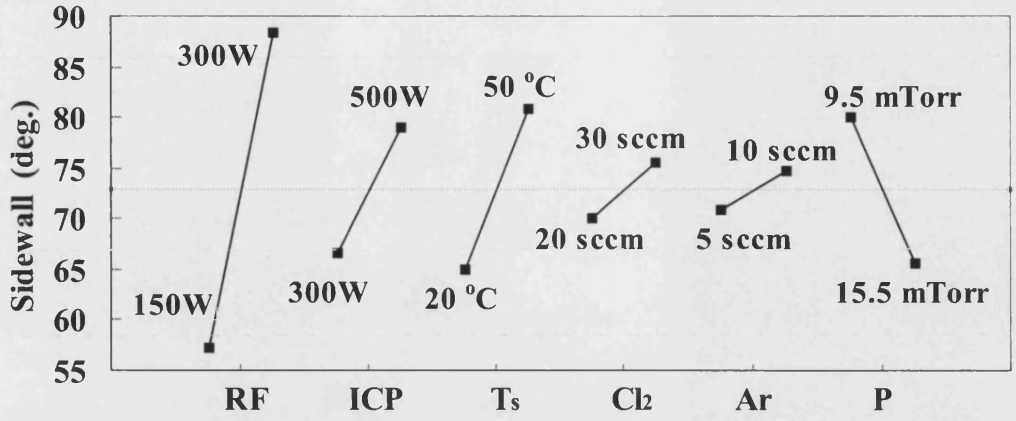

FIGURE 3.8: Effect plot of etch parameter versus sidewall angle.

roughness. It has been found that the particle size drops significantly with the increase of electron temperature [39]. In addition, a higher electron temperature can be obtained at lower pressure (see Section 3.4.3). Thus, the results show that a smaller particle size may be formed at lower pressure. The collisions between electrons and smaller particles are less, resulting in a less negative charge density of the particles. Thus, the drag forces from neutral species have to take into account; Eq. 3.14 becomes

$$\mathbf{F}_{net} \approx \Sigma \mathbf{F}_{ion} - \Sigma q\mathbf{E} + \Sigma \mathbf{F}_{neutral} \tag{3.15}$$

where $\Sigma \mathbf{F}_{neutral}$ is the total drag force from neutral species. Because of a lower negative charged density in smaller particles $\Sigma \mathbf{F}_{ion}$ and $\Sigma q\mathbf{E}$ is relatively smaller, indicating the forces acting in the z-direction may be relatively large. This may increase the possibility of redeposition. Moreover, higher ICP power was found to result in a rough surface. Higher ICP power generates higher ion density, consequently increasing the total ion drag force $\Sigma \mathbf{F}_{ion}$. Hence, more deposition of etch products is expected.

Ar flow rate has a strong effect on the surface roughness. The increase in Ar flow rate can increase the Ar^+ ions in the plasma, thus reducing the Cl^+ concentration. It implies that the vertical etching is reduced. In addition, the Ar^+ ions may

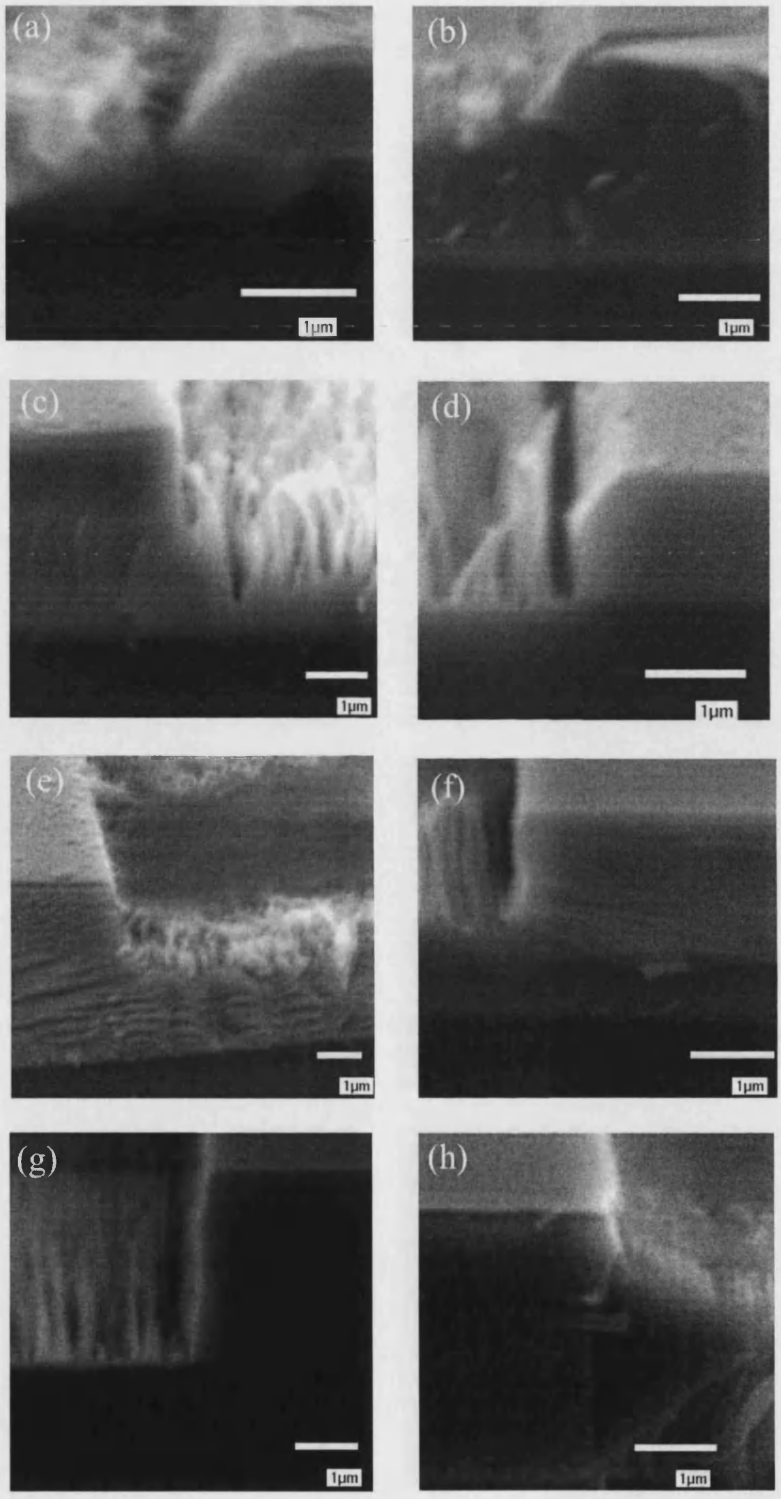

FIGURE 3.9: SEM images of sidewall profile for experiments No. 1 - 8. Note that the white line in the pictures represents 1 μm and the SiO_2 mask has not been removed.

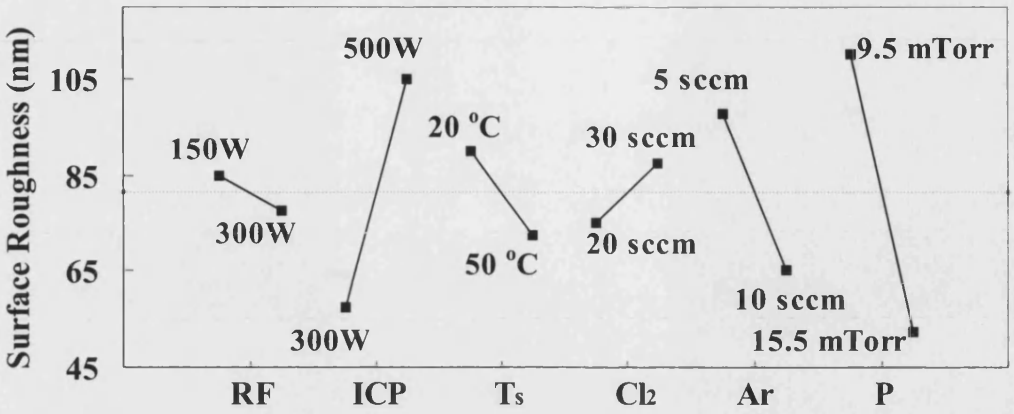

FIGURE 3.10: Effect plot of etch parameter versus surface roughness.

sputter the particles on the surface, which facilitate the formation of a smoother surface.

Possible etch products are listed below:

Etch Products	Description
$GaCl_3$, $AlCl_3$, $InCl_3$	Cl^+ + (GaN, AlGaN, InGaN)
O_2, $SiCl_4$	Cl^+ + SiO_2 cover plate
Ga_2O_3, Al_2O_3, In_2O_3	O_2 + (GaN, AlGaN, InGaN)
SiO_2 particles	Physical sputtering for SiO_2 cover plate

The boiling point of $SiCl_4$ is 58 °C and the stage temperature can be increased to ~160 °C without backside helium cooling [49]; thus, the $SiCl_4$ tends to be evaporated and has little effect on the redeposition of etch products. The boiling point of $GaCl_3$, $AlCl_3$ and $InCl_3$ is higher than 160 °C (see Table 3.1), indicating the possibility of the contribution to redeposition. For the metal oxides and sputtered SiO_2 particles, because the cover plate is 8 inch in diameter, which is comparatively much larger compared than the 1 cm^2 sample, the contribution tends to be larger. Yoshida *et al.* [50] observed a similar structure after RIE etching for GaN. Different cover plates, Si, SiO_2 and Ge, were used to clarify the re-deposition effect [51]. A smooth surface was obtained by using Ge and Si

cover plates, indicating that the improvement in surface roughness is due to the formation of more volatile etch products. However, chlorine ions have a higher reaction rate with Si or Ge; most of the reactive chlorine ions are consumed by Si or Ge, resulting in a lower etch rate of GaN.

Relative Effect Table of ICP Etching Parameters

Based on the effect plots of etch rates, DC bias, sidewall angle and surface roughness, a single relative effect table was established (Table 3.4). The difference in level one and two for the most significant parameter is 100%. The differences of level one and two for the other parameters are normalised to this base value.

From this relative effect table one can clearly see that RF power is the most significant parameter affecting sidewall angle and DC bias, but has less effect on surface roughness. ICP contributes the most to GaN etch rate and surface roughness, but demonstrates less influence on DC bias. Stage temperature has a large effect on GaN etch rate, a medium effect on sidewall angle, and a lesser effect on DC bias. Cl_2 flow rate showed a low effect on all results. Ar flow rate had a medium effect on surface roughness and less influence on etch rate, sidewall and DC bias. Chamber pressure showed the most significant effect on surface roughness, a strong effect on etch rate, a medium effect on sidewall angle but a lesser effect on DC bias.

This relative effect table is a useful tool for the optimisation of the required etch rate, sidewall angle, DC bias and surface roughness in these two levels. However, because the same etching parameter may have different relative effects on the outputs, the weighting has to be set. The following section is an example of optimisation.

Optimisation of Sidewall Angle, Surface Roughness and Etch Rate

Assume that one process is required to produce a vertical sidewall, a smooth etched surface and a high etch rate. The most critical result is the vertical

	Etch Rate	Sidewall	DC Bias	Roughness
RF	67%	**100%**	**100%**	13%
ICP	**100%**	40%	12%	82%
T_s	67%	51%	21%	30%
Cl_2	38%	18%	3%	21%
Ar	38%	12%	13%	56%
Pressure	66%	47%	14%	**100%**

TABLE 3.4: The relative effect table of ICP etching parameters on etch rate, sidewall angle, DC bias and Surface roughness.

Parameter	Value
RF Power	300W
ICP Power	500W
T_s	50°C
Cl_2 Flow Rate	30 sccm
Ar Flow rate	10 sccm
Chamber Pressure	9.5 mTorr

TABLE 3.5: The optimised conditions for the GaN LED structure.

sidewall, less importantly the surface roughness and also the etch rate. The weighting for these three outputs are set 70%, 20% and 10%, respectively. By multiplying these weighting with the relative effect, a single weighted effect table is obtained. It is seen that RF power has the most significant effect on sidewall angle. According to the effect plot of sidewall angle, the optimised RF power for larger sidewall angle is 300W. Determination of the other etching parameters follows the same method. The optimised etching conditions are listed in Table 3.5.

Figure 3.11 shows the SEM image after etching. It is seen that a vertical sidewall has been obtained. The GaN etch rate was 4570 Å/min. There was a column structure of height ~ 1 μm formed on the surface. This may have been induced by the re-deposition of etch products.

	Etch Rate	Sidewall	Roughness
RF	6.7%	**70%**	2.6%
ICP	10%	**28%**	16.4%
T_s	6.7%	**35.7%**	6.0%
Cl_2	3.8%	**12.6%**	4.2%
Ar	3.8%	8.4%	**11.2%**
Pressure	6.6%	**32.9%**	20%

TABLE 3.6: The weighted effect table of ICP etching parameters on etch rate, sidewall angle, and surface roughness.

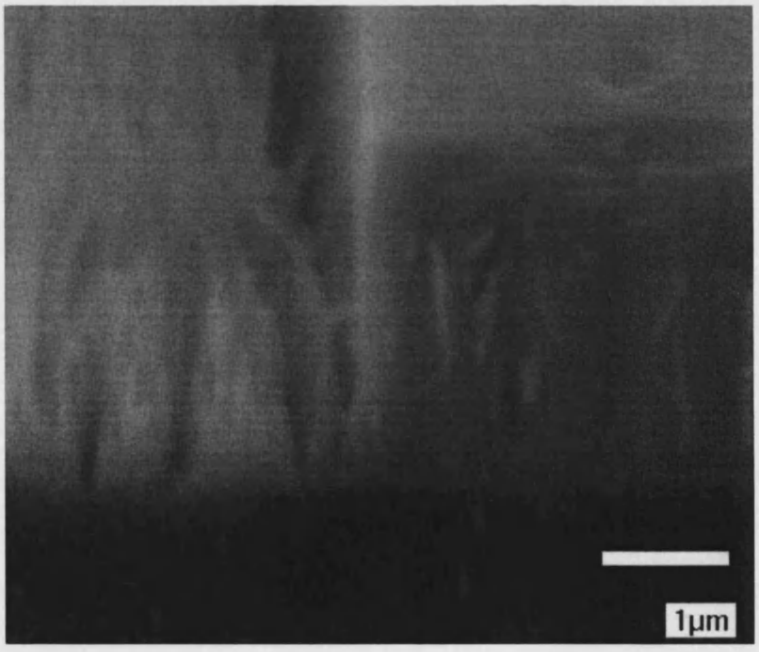

FIGURE 3.11: SEM image of sidewall profile of the sample etched by optimised conditions.

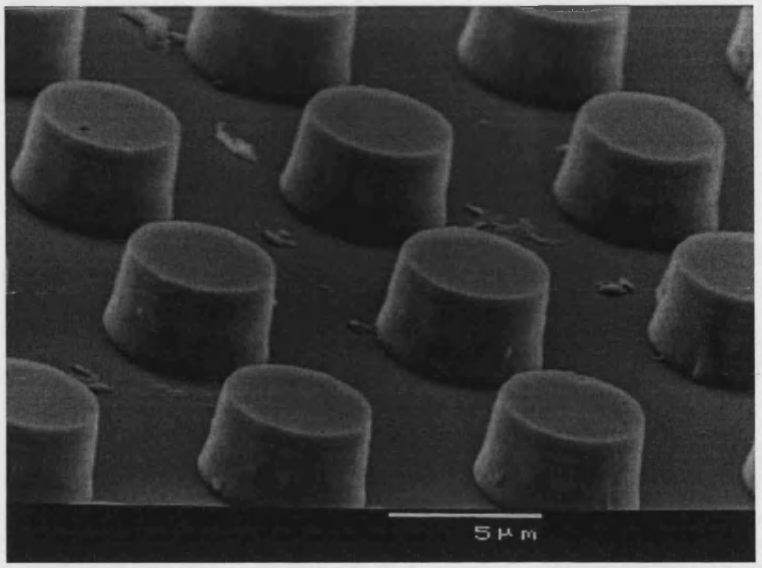

FIGURE 3.12: SEM image of etched bulk GaN.

Formation of Column Structure after Etching

In the ICP etching for the GaN LED used in this study, a column structure was observed for all cases after etching. In order to extinguish the effect of the AlGaN and InGaN layers on the etching surface, one ICP etching experiment for a thick GaN layer (3.8 μm) was conducted using the optimised condition described above. Figure 3.12 shows the SEM image of the etched features. It is seen that no column structure formed after ICP etching, indicating the significant effect of the AlGaN and InGaN layers. The etch products, $AlCl_3$,$InCl_3$, Al_2O_3, and In_2O_3, may be attributed to the formation of the column structure.

3.6 Damage Induced by SiO_2 Sputter Deposition

SiO_2 has been an important material in the semiconductor industry since it is an abundant and dielectric material. For GaN-based device processing, SiO_2 can be used as a passivation layer or an etch mask for ICP etching. However, it has been found that the oxygen in SiO_2 can possibly diffuse into GaN [40, 43], and it may induced damage in GaN electronic devices.

Oxygen is an important residual impurity in GaN. It is generally believed that the oxygen residue contributes to the n-type conductivity in unintentionally doped GaN [44]. The source of oxygen may be from the growth or post-growth process. Wang *et al.* [40] deposited a SiO_2 film on an unintentionally doped GaN film by e-beam evaporation and then removed it by buffered HF wet etching, and found that the oxygen concentration in the 3 μm thick GaN was increased $\sim$10 times. A photoluminescence (PL) measurement showed that the intensity was dramatically decreased. This decrease may be attributed to the non-radiative recombination centres induced by the incorporated oxygen [40]. After annealing this sample in a rapid thermal annealing (RTA) system at 1100 °C in nitrogen for 50 seconds, the PL intensity was increased in comparison with the as-grown sample. It implies that both of the removal of defects and the improvement of crystal quality [45] contributes to the increase in the PL intensity.

SiO_2 deposition on p-GaN was also investigated [43], and oxygen diffusion into GaN was observed. The path for this diffusion is suggested to be the threading dislocations. There was no measurable change in the hole concentration for the sample annealed at 900 °C for 5 minutes. However, Lee *et al.* [46] discovered that annealing SiO_2-capped p-GaN at 850 °C to 900 °C for 30 minutes increased the hole concentration. Because the quantity and depth of the diffused oxygen atoms are proportional to the annealing time, higher oxygen concentration inside the p-GaN may change the material properties. The authors proposed that the improvement of hole concentration may be due to SiO_2 preventing the out-diffusion of cracked Mg from the Mg–H complex during annealing.

Light emitting devices usually consist of quantum wells sandwiched between n-type and p-type semiconductors and the main emission of light originates in these quantum wells. According to Wang *et al.* [40], the diffusion depth of oxygen from the capping layer was measured as high as 3 μm , indicating the possibility of inducing damage by the oxygen diffusion process. Thus, it is essential to study the damage induced by SiO_2 deposition. In the experiment presented in the following section, the photoluminescence intensity of the quantum well was measured to determine the significance of sputtering parameters for the damage induced by SiO_2 sputtering deposition.

3.6.1 Basics of Ion Beam Sputtering

Ion Beam Source

A multi-aperture electron bombardment ion source was invented in 1961 by H. R. Kaufman as an ion thruster for space propulsion, and generates collimated, well-characterised ion beams from a wide choice of gas species [41]. When the ion energy is increased to a value higher than the threshold of bond-breaking for a given material, it can be used as a technique to dry etch and sputter this material.

Figure 3.13a shows an ion source with a dual-grid extraction system. In a novel ion source, the plasma is normally generated by applying RF or microwave power into the chamber, which is similar with the etching chamber described in Section 3.2. The first grid of the extraction system is called the screen grid and is directly bolted to the body of the source, while the second grid, or the accelerator grid, is floated and connected to a negative voltage source.

The potential distribution along the direction of ion projection is shown in Figure 3.13b. Because the screen grid is connected to the reactor, the ion energy is determined by the potential difference between sheath potential and screen grid potential.

The maximum current density in the extraction system can be obtained by solving

Poisson's equation (Eq. 3.9). For parallel plates, the maximum current density is given by [42]

$$J = \frac{4}{9}\epsilon_0 \left(\frac{q}{m}\right)^{1/2} \frac{V_t^{3/2}}{l^2} \tag{3.16}$$

where ϵ_0 is the permittivity of free space, q/m is the charge-to-mass ratio of the accelerated ions, $V_t = (V_s - V_{acc})$ and l is the potential difference and distance between the two grids, respectively, and V_s and V_{acc} is the voltage of the screen grid and accelerator grid, respectively. According to this equation the maximum current is related to the potential difference between two grids in the extraction system. However, the increase in the voltage of accelerator grid enables only slight increase in the maximum current density because the space charges outside the accelerator grid tend to be decelerated by the accelerator grid, resulting in a screening effect for further incoming ions. Because the deceleration process occurs while ions are leaving the extraction region, the accelerator grid can act as a defocusing lens.

The RF power applied to the ion gun determines the plasma density. Hence, the increase in the RF power resulting in the increase in the extracted ion density. This effectively decouples the control of ion current and energy.

Ion Beam Sputtering Deposition

For a given material and ion energy, the deposition rate is given by

$$R_{dep} = \frac{\text{Film Thickness}}{\text{Time}} = \eta \left(\frac{N_{mat} M}{D A_{sub} t}\right) \tag{3.17}$$

where η is the fraction of the particles deposited on the substrate, which is a function of the collision processes along the path from the target material to the substrate, N_{mat} is the number of the particles, M is the mass of the particles, D is the density of the material, A_{sub} is the substrate area, and t is time. Define a

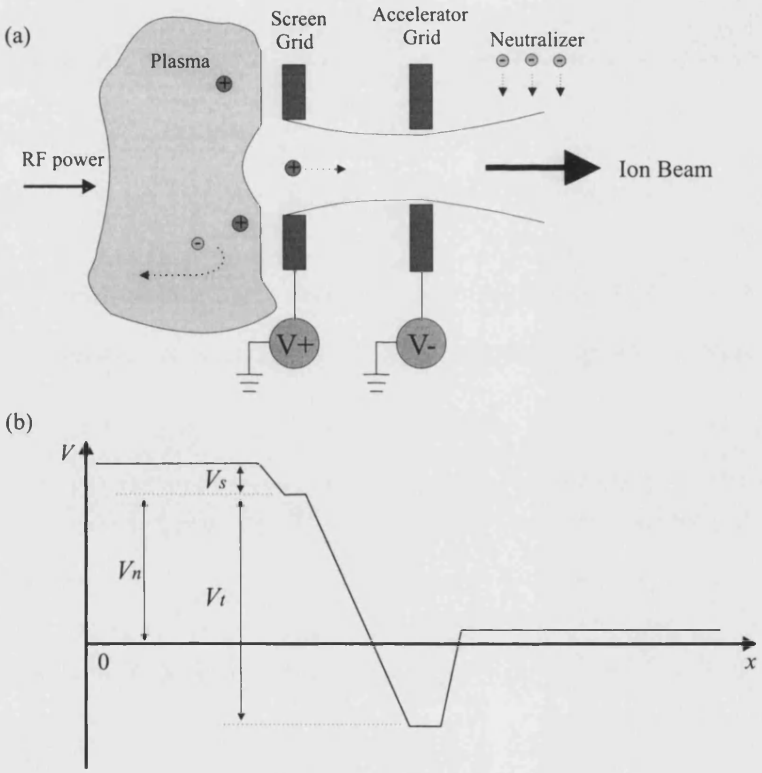

FIGURE 3.13: Schematic of (a) an ion beam source and (b) the potential distribution in the direction of ion injection.

sputtering yield (Q) for a given material and ion energy:

$$Q \equiv \frac{N_{mat}}{N_{ion}} = \frac{N_{mat}}{I_{ion}t} \tag{3.18}$$

where N_{ion} is the number of ions, I_{ion} is the ion current. Combining Eq. 3.16, Eq. 3.17 and Eq. 3.18 gives

$$R_{dep} = \eta \left(\frac{4}{9}\epsilon_0\right)\left(\frac{q}{m}\right)^{1/2}\left(\frac{QA_{grid}V_t^{3/2}M}{DA_{sub}l^2}\right) \tag{3.19}$$

3.6.2 Photoluminescence

Photoluminescence (PL) spectroscopy is a contactless, nondestructive method of probing the electronic structure of materials. Light with energy higher than the bandgap of the material is directed onto the material, where it is absorbed and imparts excess energy into the material by a photo-excitation process. One way this excess energy can be dissipated by the sample is through the emission of light, or luminescence. In the case of photo-excitation, this luminescence is called "photoluminescence" [47]. The intensity and spectral content of this photoluminescence is a direct measure of various important material properties.

Specifically, photo-excitation causes electrons within the material to move into permissible excited states. When these electrons return to their equilibrium states, the excess energy is released and may include the emission of light (a radiative process) or may not (a nonradiative process). The energy of the emitted light, or photoluminescence, is related to the difference in energy levels between the two electron states involved in the transition – that is, between the excited state and the equilibrium state. The number of photons emitted is related to the relative contribution of the radiative process.

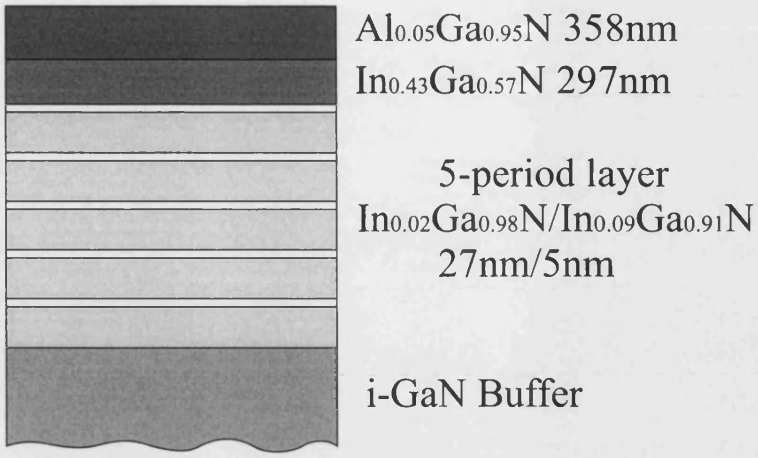

FIGURE 3.14: Structure of InGaN MQW.

3.6.3 Experiment

The sample used in the experiment was an InGaN multiple quantum well (MQW) grown by MOCVD. After the growth of the undoped GaN buffer layer, 5 layers of $In_{0.02}Ga_{0.98}N$/ $In_{0.09}Ga_{0.91}N$ MQWs were grown with thicknesses of 269Å/53Å. Subsequently, an $In_{0.43}Ga_{0.57}N$ and $Al_{0.05}Ga_{0.95}N$ layer was grown with a thickness of 297 nm and 358 nm, respectively (Figure 3.14). This sample was then cut into 9 pieces and PL measurements were performed at room temperature for each piece using a 325 nm He-Cd laser. The PL intensity was measured by means of a power meter. A SiO_2 layer was coated onto each sample by a Nordiko dual ion beam sputtering system. The deposition rate was measured by a stylus profilometer. The SiO_2 film was then removed by dipping the samples into 10% HF for 3 minutes. Subsequently, a PL measurement was performed again to measure the change of PL intensity.

The configuration of the Nordiko dual ion beam sputtering system is illustrated in Figure 3.15. Ar^+ ions are generated by applying 13.56 MHz RF power into the ion gun which is 10 cm in diameter. One neutraliser is installed in front of the ion gun to neutralise the emitted Ar^+ ions, which eliminates the charging of the target. One 6-inch fused SiO_2 target was used for SiO_2 thin film deposition. O_2 and Ar sources are introduced to the chamber from gun 2.

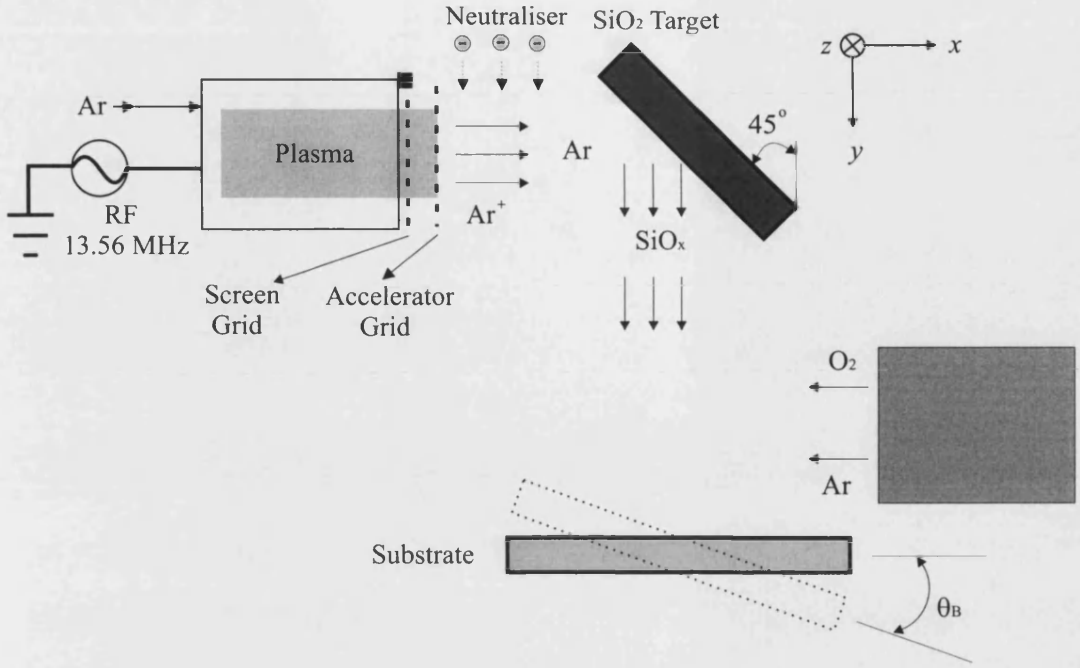

FIGURE 3.15: Schematic of Nordiko dual ion beam system.

	Symbols and Parameters	Level 1	Level 2
A	Screen Grid Voltage (V)	400	500
B	Accelerator Grid Voltage (V)	200	300
C	RF Power (W)	100	140
D	O_2 Flow Rate (sccm)	12	20
E	Ar Flow Rate (sccm)	10	0
F	Substrate Angle θ_B (degrees)	0	25

TABLE 3.7: Parameters and levels used in this study.

The experiment is based on the Taguchi method (see Section 3.5.1) such that it is possible to minimise the number of experiments. Parameters used in this study are the screen grid voltage, the accelerator grid voltage, RF power, O_2 flow rate, Ar flow rate, and substrate angle. All parameters contain two levels (Table 3.7) and an two-level orthogonal matrix was employed in the experimental layout (Table 3.8). The goal of this set of experiments is to obtain a high SiO_2 deposition rate with a small decrease of PL intensity.

No	A	B	C	D	E	F
1	400	200	100	12	10	0
2	400	200	100	20	0	25
3	400	300	140	12	10	25
4	400	300	140	20	0	0
5	500	200	140	12	0	0
6	500	200	140	20	10	25
7	500	300	100	12	0	25
8	500	300	100	20	10	0

TABLE 3.8: Experimental matrix of the SiO_2 ion beam sputtering deposition tests, according to the Taguchi experimental method.

3.6.4 Results and Discussion

SiO_2 Deposition Rate

The effect plot of sputtering parameters for the deposition rates of SiO_2 is shown in Figure 3.16. It is seen that the screen grid voltage was the most significant parameter for the SiO_2 deposition rate. In practice, the sputtering yield for the ion energy less than 1 keV can be expressed as [19]

$$Q = b\frac{4mM}{(m+M)^2}\frac{E_{ion}}{U_0} \tag{3.20}$$

where b is a constant, E_{ion} is the ion energy and U_0 is the surface binding energy of the material being sputtered. According to Eq. 3.19 and Eq. 3.20 the deposition rate for a given material and ion in this experimental setup is given by

$$R_{dep} \propto \eta E_{ion} V_t^{3/2} \approx aqV_s(V_s - V_{acc})^{3/2} \tag{3.21}$$

This equation indicates that V_s is the dominant factor for the deposition rate, which is consistent with the experimental results.

The increase in RF power can induce a larger sheath potential, resulting in a decrease in the ion energy. However, the increase in RF power can also increase the ion current because the plasma density has been increased. These results imply that the ion energy may be the dominant factor for the deposition rate of the SiO_2 film.

The accelerator grid voltage has minor effects on the deposition rate. The increase of the accelerator grid voltage only slightly increases the ion current and it may decelerate the ions that are just leaving the extraction region and subsequently reduce the ion energy.

Eq. 3.21 shows the factor η, which is the function of the collision process between sputtered SiO_2 particles and Ar/O_2 from gun 2, is proportional to the deposition rate. O_2 has little effect on the deposition rate; O_2 molecules can contribute to the scattering of SiO_2 and reaction of the non-stoichiometric SiO_x. However, according to the momentum conservation law, the scattering effect of SiO_2 particles is less than that in Ar because the mass of Ar is larger than that of oxygen. In addition, the reaction of O_2 and SiO_x is an attachment of oxygen atoms to the SiO_x. This process maintains the ion energy but only slightly changes the impinging angle to sample. Hence, the contribution of the O_2 flow rates is less.

Altering the substrate angle showed much less effect on the deposition rate. It implies that the scattering of the impinging SiO_2 particles on the sample is nearly independent of the substrate angle.

Decrease in PL Intensity

The PL intensity is determined by the number of excited electrons and the number of radiative and non-radiative recombination process. The former one is related to the excitation power, *i.e.* the power of 325nm He-Cd laser transmitted to the samples, while the latter one depends on the number of radiative centres. These two possible factors are examined below.

The first consideration is the change of laser power due to the surface modification

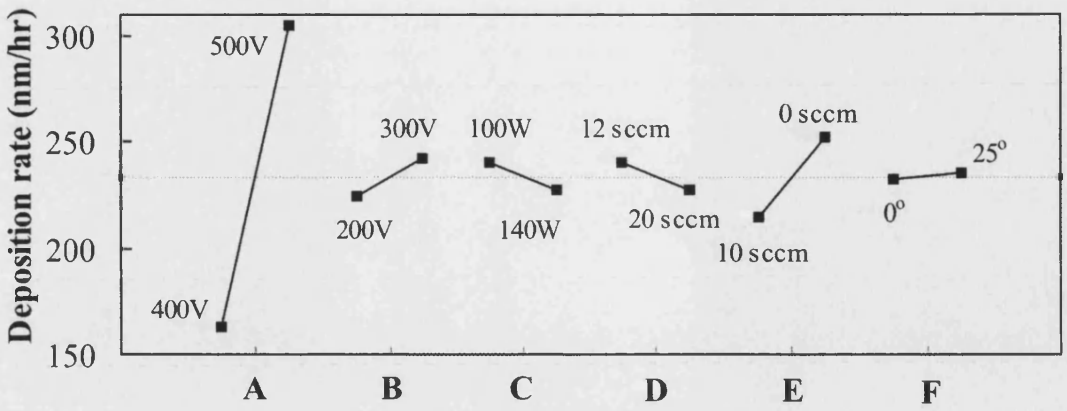

FIGURE 3.16: Effect plot of sputtering parameters for SiO_2 deposition rate.

induced by the SiO_2 particles, which depends on the bonding energy of the sample material when the energy and flux of impinging particles are constant. Mitani *et al.* [48] have studied the effect of sputter deposition of SiO_2 on GaAs surface. They reported that the thickness of the surface–modified layer was 7 – 9 nm as measured by TEM. Because the surface damage is strongly related to the material bonding energy and the bonding energy for GaAs is 6.5 eV in comparison with that of GaN 8.9 eV, InN 7.7 eV, and AlN 11.5 eV, the damage to the surface of GaN may be less than that in the case of GaAs. According to Eq. 2.28, the modification of light transmittance in GaN is estimated to be in the range 30 – 50 nm for wavelengths 325 nm and 490 nm. Hence, this effect in GaN would be reduced.

Assuming that the total number of excited electrons (N_{All}) is identical at the same materials and excitation power and all excited electrons undergo the recombination process, the PL intensity then is given by

$$P_{PL} = N_{rad}P_{rad} = (N_{All} - N_{non-rad})P_{rad} \tag{3.22}$$

where P_{rad} is the power from one single radiative recombination process, N_{rad} and $N_{non-rad}$ is the number of radiative and non-radiative centres, respectively. To change P_{PL} either N_{rad} or $N_{non-rad}$ has to be changed. The decrease in the number of radiative centres may be due to the damage of MQW, while the increase of non-radiative centres may be achieved by newly introduced non-radiative centres

in the bandgap.

The effect plot of sputtering parameters for the decrease in PL intensity is shown in Figure 3.17. The Ar flow rate is the most significant parameter.

According to the results of deposition rate experiments, the increase in Ar flow rate can reduce the deposition rate, indicating the presence of collisions between the sputtered SiO_2 particles and the Ar atoms in the path to the substrate. Because Ar is an inert gas, the collisions with SiO_2 particles are only physically energy transfer. The effect plot of sputtering parameter versus the decrease in PL intensity (Figure 3.17) shows that Ar flow rate is the most significant parameter, indicating that the reduction for the kinetic energy of sputtered SiO_2 particles is larger using higher Ar flow rate.

The screen grid voltage and RF power, which contribute to the change of ion current and ion energy, are the second most significant parameters responsible for the decrease of PL intensity. It implies that the total bombardment energy change for these two parameters is similar, and the change in the bombardment energy for the given levels is less than that induced by changing Ar flow rate for the given levels.

The substrate angle has less effect on the decrease of PL intensity. The bombardment momentum of SiO_2 particles can be decreased by tilting sample; 25° tilting has decreases the bombardment momentum ~10% though the bombardment energy is nearly identical because most of the impinging SiO_2 particles are deposited on the substrate, *i.e.* ~100% energy transfer. It implies that the bombardment energy is the dominant factor instead of bombardment momentum.

Optimisation of SiO_2 Deposition Rate and Decrease of PL Intensity

A high SiO_2 deposition rate with low decrease in PL intensity is required for device processing. According to the method developed in ICP etching, one relative effect table was established (Table 3.9).

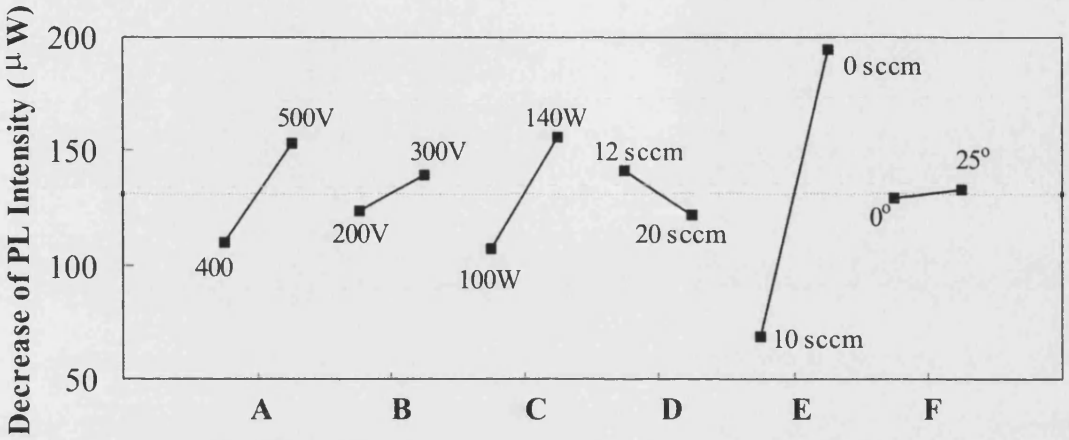

FIGURE 3.17: Effect plot of sputtering parameters versus PL intensity decrease.

	Deposition Rate	Decrease of PL Intensity
Screen Grid Voltage	**100.0%**	34.5%
Accelerator Grid Voltage	12.3%	12.4%
RF Power	8.8%	38.9%
O_2 Flow Rate	8.8%	14.8%
Ar Flow Rate	26.3%	**100.0%**
Substrate Angle	1.8%	3.0%

TABLE 3.9: The relative effect table of sputtering parameters on SiO_2 deposition rate and the decrease of PL intensity.

Parameter	Value
Screen Grid Voltage	500V
Accelerator Grid Voltage	200V
RF Power	100W
O_2 Flow Rate	20 sccm
Ar flow rate	10 sccm
Substrate Angle	0^o

TABLE 3.10: The sputtering parameters used in the optimisation.

	Deposition Rate	Decrease of PL Intensity
Screen Grid Voltage	**40.0%**	20.7%
Accelerator Grid Voltage	4.9%	**7.5%**
RF Power	3.5%	**23.3%**
O_2 Flow Rate	3.5%	**8.9%**
Ar Flow Rate	10.5%	**60.0%**
Substrate Angle	0.7%	**1.8%**

TABLE 3.11: The weighted effect table of sputtering parameters on SiO_2 deposition rate and the decrease of PL intensity.

In this optimisation, the weighting of the SiO_2 deposition rate and the decrease of PL intensity was chosen to be 40% and 60%, respectively. The weighted effect table is given in Table 3.11. It is seen that the value of accelerator grid voltage, RF power, O_2 flow rate, Ar flow rate and substrate angle which gives lower decrease in PL intensity should be chosen, while the value of screen grid voltage which gives higher deposition rate has to be used. The sputtering parameters used in the optimisation are listed in Table 3.10. This condition has given a high SiO_2 deposition rate, 290nm/hr, and a low decrease of PL intensity 54 μW.

3.7 Summary

A comprehensive study of ICP etching of GaN LED structures has been undertaken based on a Taguchi experimental design. ICP power appeared to be the most significant parameter for determining the etch rate of GaN. The observed

domination of the chemical etching for GaN etching was consistent with earlier reports. RF power, chamber pressure and stage temperatures had a similar effect on the etch rates. This may be due to the effect of redeposition of the etch products. Higher RF power stimulates desorption of the etch products and partially contributes to the direct physical sputtering. A lower chamber pressure increases the electron temperature, resulting in the formation of more etch products and partially contributes to the low scattering of ions. Lower stage temperatures result in less etch products, resulting in less obstruction to further etching. Cl_2 and Ar flow rate showed only a minor effect on etch rate.

RF power demonstrated the dominant role for DC bias because of the induced strong electric field in the sheath region. Other parameters had a minor effect on the DC bias.

Sidewall angle has been found to be sensitive to the ion bombardment and the redeposition of the etch products. The dominant parameter was RF power which controls the ion bombardment energy. The stage temperature and chamber pressure had a similar effect. These last two parameters are related to the size of the etch products. Higher ICP power induced more etch products deposited on the sample surface due to the increase in ion density, degrading the etching profile. Cl_2 and Ar flow rates showed a minor effect on the sidewall angle.

Surface roughness was found to be more dominated by the re-deposition of the etch products. ICP power and chamber pressure indicates this significance. Lower chamber pressure increases the electron temperature and then reduces the size of etch products. Higher ICP power mainly contributes to a higher ion drag force, resulting in more re-deposition of the etch products. Ar flow rate is the third most important parameter for this issue. The higher Ar flow rate contributes to a higher physical sputtering. This reduces the redeposition of etch products and then a smooth surface can be obtained.

The effect plots of etching parameters and relative effect table for the GaN LED structures were established. One method was constructed for optimisation of the required etching results. An optimisation experiment was conducted and this showed a vertical sidewall with etch rate 4570 Å/min.

A column structure was observed for all the samples after etching. In order to distinguish the effect induced by AlGaN and InGaN, one bulk GaN was etched used the optimised condition. A smooth etching surface and vertical sidewalls were obtained, indicating the additional AlGaN and InGaN have introduced the formation of the column structure. The etch products, $AlCl_3$,$InCl_3$, Al_2O_3, may act as micro-masks for the etching process.

The study of the decrease in PL intensity induced by SiO_2 deposition has been undertaken, again by a Taguchi experimental design. The decrease in the PL intensity may be due to either the damage of the MQW or the introduction of newly non-radiative centres, or both.

The results of the SiO_2 deposition rate experiments showed that the screen grid voltage is the most significant parameter affecting the SiO_2 deposition rate. Theoretical calculation, based on the current density of ion gun and sputtering yield, shows agreement with the experimental results. However, the increase in RF power, which contributes to the increase in ion density, showed a minor effect on the deposition rate. It implies that the dominant factor for the deposition rate of SiO_2 in this experiment is the ion energy. The substrate angle is nearly independent of the deposition rate. It is because the cross section of the impinging SiO_2 particles in the plane of the substrate angle (equal to zero) is only changed 9% when the substrate rotates 25^o.

The Ar flow rate was the most significant parameter in the decrease of PL the intensity. Because the deposition rate was decreased when increasing Ar flow rate, it indicates the presence of collisions between the sputtered SiO_2 particles and the Ar atoms in the path to the substrate. Therefore, increasing Ar flow rate is the most effective method in the experiments for reducing the kinetic energy of sputtered SiO_2 particles by collisions.

An optimisation experiment was carried out to obtain a high SiO_2 deposition rate with a low decrease of PL intensity. A 500V screen grid voltage, 200V accelerator grid voltage, 100W RF power, 20 sccm O_2 Flow Rate, 10 sccm Ar flow rate, and 0^o substrate angle were the optimised conditions for these two given levels. A high SiO_2 deposition rate, 290nm/hr, with a small decrease in PL intensity, 54 μW, was achieved.

References

[1] D. M. Manos, and D. L. Flamm, *Plasma Etching An Introduction* (Academic Press, Inc., London, 1989).

[2] H. Lee, D. B. Oberman, and J. S. Harris, *Appl. Phys. Lett. 67* ,1754 (1995).

[3] S. J. Pearton, C. R. Abernathy, F. Ren, J. R. Lothian, P. W. Wisk, and A. Katz, *J. Vac. Sci. Technol. A* **11**, 1772 (1993).

[4] D. R. Lide (ed.), *Chemical Rubber Company handbook of chemistry and physics* **77th edition**, CRC Press, Boca Raton, Florida, USA, , 1996.

[5] S. J. Pearton, *Mat. Sci. & Eng. B* **40**, 101 (1996).

[6] M. V. Malyshev, V. M. Donnelly, A. Kornblit, and N. A. Ciampa, *J. Appl. Phys.* **84**, 137 (1998).

[7] H. Cho, C. B. Vartuli, S. M. Donovan, C. R. Abernathy, S. J. Pearton, R. J. Shul, and C. Constantine, *J. Vac. Sci. Technol. A* **16**, 1631 (1998).

[8] M. V. Malyshev, N. C. M, Fuller, K. H. A. Bogart, V. M. Donnelly, and I. P. Herman, *J. Appl. Phys.* **88**, 2246 (2000).

[9] M. V. Malyshev, and V. M. Donnelly, *J. Appl. Phys.* **88**, 6207 (2000).

[10] R. J. Shul, G. B. McClellan, S. A. CasaInuovo, D. J. Rieger, S. J. Pearton, C. Constratine, C. Barratt, R. F. Karlicek, Jr., C. Tran, and M. Schurman, *Appl. Phys. Lett.* **69**, 1119 (1996).

[11] S. A. Smith, C. A. Wolden, M. D. Bremser, A. D. Hanser, R. F. Davis, and W. V. Lampert, *Appl. Phys. Lett.* **71**, 3631 (1997).

[12] R. J. Shul, L. Zhang, C. G. Willison, J. Han, S. J. Pearton, J. Hong, C. R. Abernathy, and L. F. Lester, *MRS Internet. J. Nitride Semicond. Res.* **4S1**, G8.1 (1999).

[13] K. Remashan, S. J. Chua, A. Ramam, S. Prakash, and W. Liu, *Semicond. Sci. Technol.* **15**, 386 (2000).

[14] H. S. Kim, D. H. Lee, J. W. Lee, T. I. Kim, and G. Y. Yeom, *Vacuum* **56**, 45 (2000).

[15] D. Basak, M. Verd, M. T. Montojo, M. A. Snchez-Garca, F. J. Snchez, E. Munoz, and E. Calleja, *Semicond. Sci. Tech.* **12**, 1654 (1997).

[16] H. Lee, D. B. Oberman, and J. S. Harris Jr, *Appl. Phys. Lett.* **67**, 1754 (1995).

[17] I. Adesida, A. Mahajan, E. Andideh, M. A. Khan, D.T. Olson, and J. N. Kuznia, *Appl. Phys. Lett.* **63**, 2777 (1993).

[18] A.T. Ping, I. Adesida, M. A. Khan, and J.N. Kuznia, *Electron. Lett.* **30**, 1895 (1994).

[19] B. Chapman, *Glow Discharge Processes* (John Wiley & Sons, Inc., USA, 1980).

[20] M. E. Lin, Z. F. Fan, Z. Ma, L. H. Allen, and H. Morkoç, *Appl. Phys. Lett.* **64**, 887 (1994).

[21] Carl Nordling, *Physics handbook: elementary constants and units, tables, formulae and diagrams and mathematical formulae* 4th edition (Chartwell-Bratt, Bromley, 1978).

[22] S. J. Pearton, C. R. Abernathy, F. Ren, and J. R. Lothian, *J. Appl. Phys.* **76**, 1210 (1994).

[23] S. Budavari (ed.), *The Merck index: an encyclopedia of chemicals, drugs, and biologicals, Whitehouse Station* **12**th edition (Merck & Co. Inc., USA, 1996).

[24] Hyun Cho, J. Hong, T. Maeda, S.M. Donovan, C.R. Abernathy, S.J. Pearton, and R.J. Shul, *Mat. Sci. & Eng. B* **59**, 340 (1999).

[25] J. K. Sheu, Y. K. Su, G. C. Chi, M. J. Jou, C. C. Liu, C. M. Chang, and W. C. Hung, *J. Appl. Phys.* **85**, 1970 (1999).

[26] B. C. Cho, Y. H. Im, J. S. Park, T. Heong, and Y. B. Hahn, *J. Korean Phys. Society* **37**, 23 (2000).

[27] Y. B. Hahn, D. C. Hays, H. Cho, K. B. Jung, C. R. Abernathy, S. J. Pearton, and R. J. Shul, *Applied Surface Science* **147**, 207 (1999).

[28] H. Cho, J. Hong, T. Maeda, S. M. Donovan, J. D. Mackenzie, C. R. Abernathy, S. J. Pearton, R. J. Shul, and J. Han, *MRS Internet. J. Nitride Semicond. Res.* **3**, 5 (1998).

[29] H. Kurosawa, S. Hasegawa, and A. Suzuki, *J. Appl. Phys.* **90**, 3713 (2001).

[30] G. A. Hebner, and C. B. Rleddermann, *J. Appl. Phys.* **83**, 5102 (2000).

[31] G. Taguchi, *Introduction to Quality Engineering* (Asian Productivity Organization, Tokyo, 1987).

[32] H. S. Kim, G. Y. Yeom, J. W. Lee, and T. I. Kim, *Thin Solid Films* **341**, 180 (1999).

[33] S. M. Rossnagel and J. R. Sites, *J. Vac Sci. Technol. A* **2**, 376 (1984).

[34] S. J. Choi and M. J. Kushner, *J. Appl. Phys.* **74**, 853 (1993).

[35] G. S. Selwyn, J. E. Heidenreich, and K. L. Haller, *Appl. Phys. Lett.* **57**, 1876 (1990).

[36] M. Schabel, T. Peterson, J. Sinclair, and D. Lynch, *J. Appl. Phys.* **86**, 1834 (1999).

[37] H. H. Hwang, and M. J. Kushner, *Appl. Phys. Lett.* **68**, 3716 (1996).

[38] M. V. Malyshev, and V. M. Donnelly, *J. Appl. Phys.* **87**, 1642 (2000).

[39] F. Y. Huang, and M. K. Kushner, *J. Appl. Phys.* **81**, 5960 (1997).

[40] X. C. Wang, S. J. Xu, S. J. Chua, K. Li, X. H. Zhang, Z. H. Zhang, K. B. Chong, and X. Zhang, *Appl. Phys. Lett.* **74**, 818 (1999).

[41] H. R. Kaufman, *Nasa Tech. Note TN*, D-585 (1961).

[42] H. R. Kaufman, *J. Vac. Sci. Technol.* **15**, 272 (1978).

[43] S. J. Pearton, H. Cho, J. R. Laroche, F. Ren, R. G. Wilson, and J. W. Lee, *Appl. Phys. Lett.* **75**, 2939 (1999).

[44] B-C. Chung, and M. Gershenzon, *J. Appl. Phys.* **72**, 651 (1992).

[45] M. W. Cole, F. Ren, and S. J. Pearton, *Appl. Phys. Lett.* **71**, 3004 (1997).

[46] C. R. Lee, J. Y. Leem, and B. G. Ahn, *J. Cryst. Growth* **216** ,62 (2000).

[47] K. D. Mielenz, *Optical Radiation Measurement* Vol. 3 (Academic Press, Inc., London, 1982).

[48] K. Mitani, and T. Kawano, *Jpn. J. Appl. Phys., Part 1* **34** ,4649 (1995).

[49] C. Gabriel, and E. Yeh, *Solid State Technol* **42**, 99 (1999).

[50] H. Yoshida, T. Urushido, H. Miyake, and K. Hiramatsu, *Jpn. J. Appl. Phys.* **40**, L1301 (2001).

[51] T. Urushido, H. Yoshida, H. Hiyake, and K. Hiramatsu, *Jpn. J. Appl. Phys.* **41**, L31 (2002).

Chapter 4

GaN Nanotube Formation and Application

4.1 Introduction

After the discovery of carbon nanotubes (CNTs) in 1991 [1], considerable efforts have been made to fabricate them and investigate their properties and potential applications. The synthesis processes for the fabrication of CNTs include chemical vapour deposition (CVD) [2], electric arc [3], and laser ablation [4]. They can be used as nano-templates for making small structures of other materials [5]. They can be modified for catalytic purposes [6] and used for gas storage [7]. In 1995 their use as a field emitter was studied and a very low turn-on electric field was obtained [8]. Because of their high strength and light weight, these nanotubes are an excellent candidate for the reinforcement of particular materials [9]. Moreover, applications for the tips for the use as atomic force microscopes [10, 11] and emitters for field emission displays [12, 13] have been developed. Many studies for these tubes are still ongoing.

The structure of CNTs is the conformal mapping of a finite number of two-dimensional layers of graphite sheet onto themselves [31]. The typical diameter of these tubes is 1.2 - 25 nm and the length can reach several microns [31] (Fig-

ure 4.1). Two distinct types of CNTs exist, depending on whether the tube walls are made of one layer (SWNT) (Figure 4.1a) or more than one (MWNT) (Figure 4.1b). The SWNTs consist of tubes made of single layers of graphene cylinders with a very narrow distribution in size range (1 – 2 nm) [14]. For the MWNTs, they consist of two or more concentric cylindrical shells of graphene sheets coaxially arranged around a central hollow with a constant separation between the layers which is nearly equal to that of the graphite-layer spacing (0.35nm) [1, 31]. Theory and experiments show that their Young's moduli are at least as high as graphite (~1 TPa) and can be even higher for small SWNTs [32]. For the MWNTs, the Young's moduli are dependent on the degree of order within the tube walls. Different growth methods for these tubes demonstrates different mechanical properties. For example, the arc-grown MWNTs have a Young's modulus close to the value of graphite, but this drops by about an order of magnitude for MWNTs grown by catalytic methods because of the presence of defects.

Carbon atoms in the carbon nanotubes are held together by strong sp^2 bonds. The rigidity of these systems, combined with the virtual absence of atomic defects, may make them very good candidates for efficient thermal conductors. Hone *et al.* [33] have measured the thermal conductivity of SWNTs and the room temperature thermal conductivity of an as-grown SWNTs is measured to be 0.35 W/cm-K.

Another interesting property of CNTs is their resistivity. A measured resistivity for a SWNT is 0.016 Ω·cm, and the value can be made as low as 0.001 Ω·cm by the addition of potassium or by bromine doping [34]. With a temperature increase from 200 K to 500 K, the resistivity maintains nearly the same value, indicative of metallic behaviour.

Oxidation of CNTs has been performed [35] and the nanotube tips were found to be much more reactive compared with the tube body. However, this reaction demonstrates less effect on a bio-compatibility experiment. Britto *et al.* [36] found that the bio-specimens in the bio-electrochemical reactions using the nanotube microelectrodes which is made by mixing nanotubes and binders do not get fouled in contrast to fouling when conventional graphite electrodes are used. This result demonstrates that CNTs are indeed bio-compatible. The major dif-

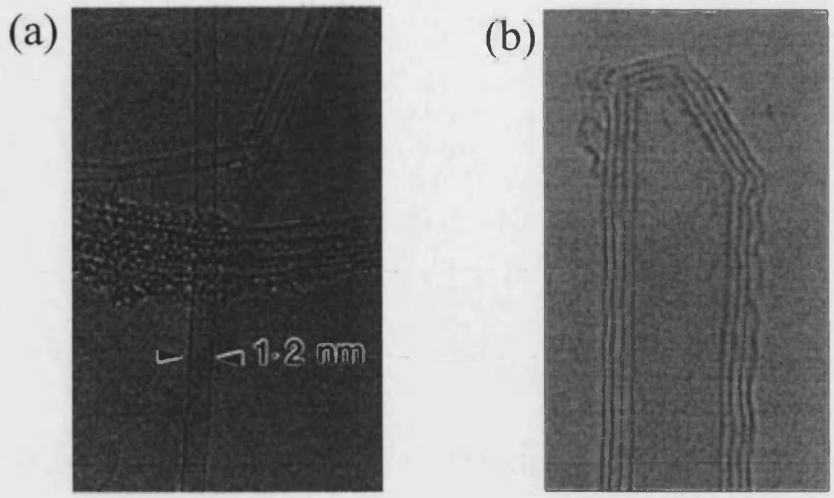

FIGURE 4.1: TEM picture for a (a) single-wall and (b) multi-wall CNT [31].

	Young's Modulus	Thermal Conductivity	Resistivity	Chemical Activity
GaN	288.1GPa [38]	1.3W/cm-K [21]	0.01 Ω·cm (n-GaN) 2 Ω·cm (p-GaN)	Inert to most of chemicals
CNTs	1000GPa [32]	0.35W/cm-K [33]	0.15 Ω·cm [34]	Oxidise [35]

TABLE 4.1: Comparison of properties of GaN and CNTs

ference between graphite and nanotube electrodes may be that the nanotubes mono-selectively expose the graphite basal planes where as all other graphitic and carbon materials have other planes exposed as reacting surfaces and thus changes the reaction kinetics [36].

GaN is a wide bandgap semiconductor with interesting physical, chemical and electrical properties. Table 4.1 demonstrates the comparison of some properties of GaN and CNTs. n-type and p-type GaN are both available and the resistivity is 0.01 Ω·cm and 2 Ω·cm, respectively, indicating the potential applications in nano–electronic devices. It is seen that the stiffness of GaN is lower than CNTs but its thermal conductivity is 4 times higher. In addition, GaN is inert to most chemicals, even most of acids and bases. This may enable GaN nanotubes to be applied in biological and chemical systems. Therefore, synthesis of GaN

in the form of nanotubes is an attractive process for future nano-engineering components.

4.2 Dislocations in GaN

The substrate of GaN epilayers grown by MOCVD is normally sapphire. Due to the lattice and thermal expansion coefficient mismatch, the quality of the GaN epilayer is not ordinarily good enough for electronic applications. An AlN buffer layer between sapphire and GaN was reported by Akasaki *et al.* [15] to dramatically improve the GaN epilayer quality, but the dislocation density was still in the range of 10^{10} cm^{-3}. It has been found that the most dislocations are of the pure edge type [16]. The other kind of defect is nano-pipe which are long faceted empty pipes threading the entire thickness of the GaN epilayer [17]. The radius of these pipes is in the range 35 – 500 Åand they appear to propagate along the *c*-axis of the film [17].

The rapid evaluation of the dislocation density in GaN film is important for the further improvement of crystal growth. TEM is the most promising method for determining the dislocation density. However, the sample preparation is very time consuming. Photo-enhanced wet etching in a KOH solution was found to rapidly reveal dislocations in GaN [18]. This is because after etching n-GaN films in diluted KOH solution with the irradiation of 325 nm Hg arc lamp, the formation of whiskers was observed (Figure 4.2). The whiskers are approximately 50 nm thick and 1 μm tall and the 1 μm height corresponds to the removal of 1 μm of the GaN material. The authors suggested that the formation of the whiskers is located around the threading dislocations.

Hino *et al.* [39] investigated the formation of etching pits after HCl vapour-phase etching. Figure 4.3 shows the TEM pictures of the etching pits and dislocations were found at the centre of these pits. The density of the etching pits is consistent with the dislocation density measured by TEM, indicating that it is an alternative method for revealing dislocations. Visconti *et al.* [19] confirmed that the number of etch pits after exposure to H_3PO_4 and molten KOH was very close to the dislocation density.

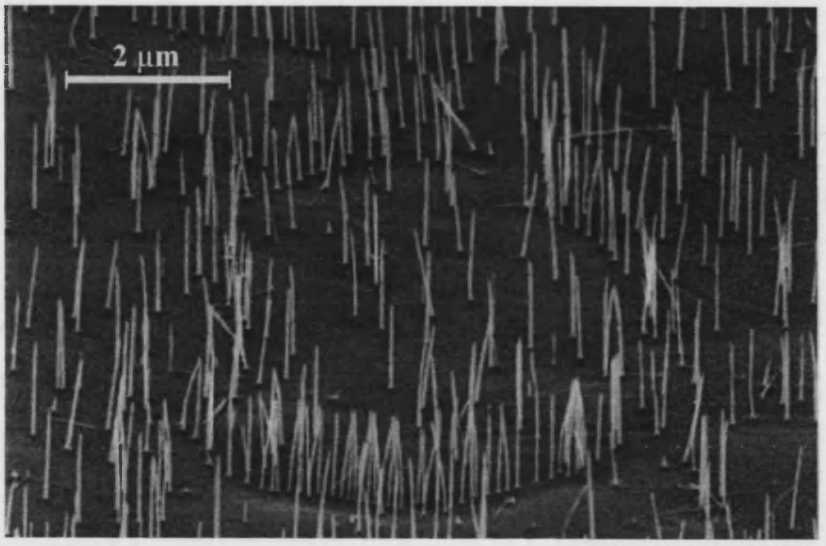

FIGURE 4.2: SEM pictures of whiskers produced by selective etching of dislocations [18].

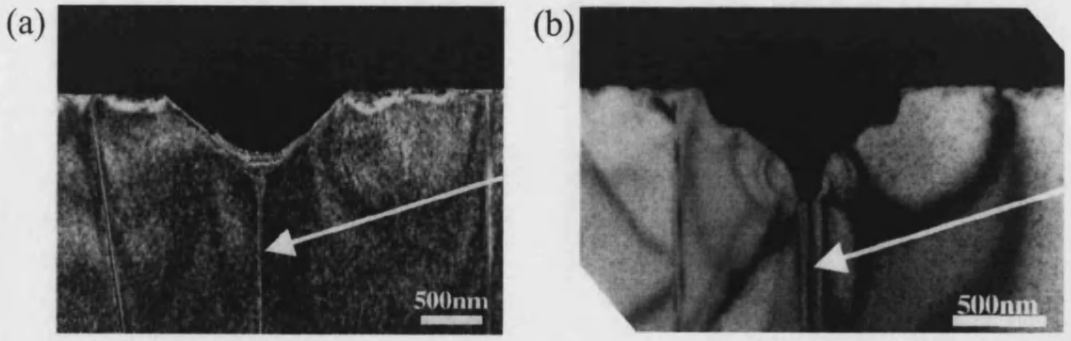

FIGURE 4.3: TEM pictures for a (a) screw dislocation and (b) mixed dislocation [39].

4.3 Piezoelectric Effect in Dislocations of GaN

The piezoelectric effect has been known to be strong in group III-nitrides [20]. The strain distribution associated with the dislocations may contribute to vary the surface potential through the piezoelectric effect. The piezoelectric effect associated with screw dislocations, which may be revealed after etching, in GaN [24] is described below.

Consider a right-hand screw dislocation with Burger vector $\mathbf{b} = (0, 0, b_s)$ (Figure 4.4), which is defined as the dislocation–displacement vector. It is seen that the displacement u_x=u_y=0 and u_z is discontinuous at the cut surface defined by y=0, x>0: [22]

$$\lim_{\xi \to 0,\ x>0} u_z(x, -\xi) - u_z(x, \xi) = b_z \qquad \xi > 0 \tag{4.1}$$

Assume that in an isotropic medium the displacement u_z increases uniformly with the angle θ to give the discontinuity,

$$u_z(r, \theta) = b\frac{\theta}{2\pi} = \frac{b}{2\pi}\tan^{-1}\frac{y}{x} \tag{4.2}$$

The distribution of displacement, u_s, can be written as column vectors

$$u_s = (u_{sx}, u_{sy}, u_{sz})^T = \left(0, 0, \frac{b_s}{2\pi}\tan^{-1}\frac{y}{x}\right)^T \tag{4.3}$$

The strain, S_s, is calculated and expressed in contracted matrix notation:

$$S_s = \frac{b_s}{2\pi}\frac{1}{x^2 + y^2}(0, 0, 0, x, y, 0)^T \tag{4.4}$$

Consider a screw dislocation in GaN, which is parallel to the c-axis of GaN. The

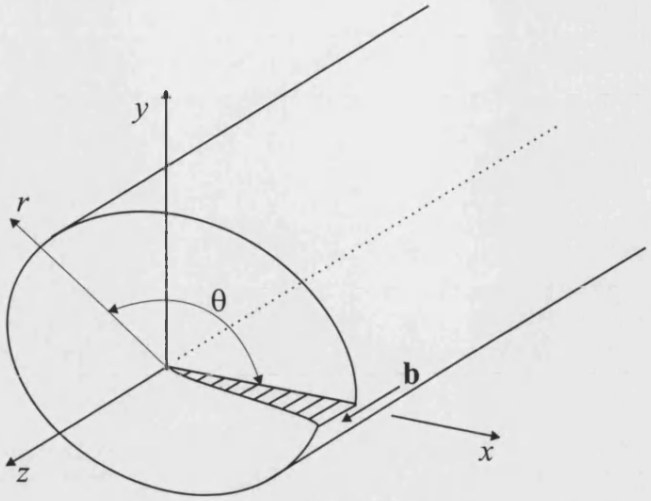

FIGURE 4.4: Illustration of a screw dislocation.

piezoelectric tensor is given the form [23],

$$e = \begin{pmatrix} 0 & 0 & 0 & 0 & e_{15} & 0 \\ 0 & 0 & 0 & e_{15} & 0 & 0 \\ e_{31} & e_{31} & e_{33} & 0 & 0 & 0 \end{pmatrix} \tag{4.5}$$

so that the piezoelectric polarisation ($\mathbf{P}_s$) can be written as

$$\mathbf{P}_s = e \times S_s = \frac{b_s e_{15}}{2\pi} \frac{1}{x^2 + y^2} \begin{pmatrix} -y \\ x \\ 0 \end{pmatrix} = \frac{b_s e_{15}}{2\pi} \frac{1}{r} \hat{\theta} \tag{4.6}$$

4.4 GaN Nanotube Formation

The results of photo-enhanced etching for GaN demonstrates the ability to selectively etch down through the dislocations. It therefore may be applicable to a dry etching process. Furthermore, the reactive ions in a dry etching chamber can enhance this selective etching in dislocations because as has been shown there is a strong piezoelectric field around the dislocations. Therefore, the following experiment has been designed to investigate the fabrication of GaN nanotubes.

4.4.1 Experiment

The GaN samples used in this study were grown on (0001) oriented sapphire by an Aixtron metalorganic chemical vapour deposition (MOCVD) reactor. After the nucleation process was completed, an undoped GaN epitaxial layer was grown at 1100 °C to a thickness of 3.8 μm. Inductively coupled plasma (ICP) etching was then used to treat the samples. The gases employed in this process were Cl_2 and H_2 with a flow rate of 50 sccm and 12 sccm, respectively. During etching the chamber pressure was maintained at 15 mTorr. The power for the ICP and RF power was set at 200W and 250W, respectively. The stage temperature was set to 29 °C with a ramp-up rate of 2.6 °C/min. The etch rate on the sample surface was subsequently measured by use of a stylus profilometer. In order to investigate the transition of the etched surface, different etching times were used and the surface changes studied by atomic force microscopy (AFM) and scanning electron microscopy (SEM). After etching for 10 minutes, the protruding remnant surface structures of this sample were removed from the etched surface by scraping and the product placed in de-ionised water. Several drops of the water containing the specimen were then dripped onto a copper grid which supported a thin electron transparent carbon film. The microstructures of the specimen were then examined by transmission electron microscopy (TEM). Energy dispersive X-ray micro-analysis (EDX) was used to study composition of the samples.

4.4.2 Results and Discussion

The etch rate for the GaN film, using ICP etching under the conditions described above, was 234 nm/min. The shape of the nanotubes is of a regular cylinder on the outside (Figure 4.5). A more complex structure was observed inside the nanotubes. It is cylindrical at the top open end. At some distance inside the cylinder the inner radius begins to reduce and diminishes until the base of the GaN becomes solid. More detailed structural information was obtained in the TEM image (Figure 4.6). The gradual decrease in intensity from the centre towards the edge of the column demonstrates that the edge was thicker than the central part and hence it was deduced that structure is in the form of a tube. The hollow part extends 1 μm from the top of the tube and then becomes narrower.

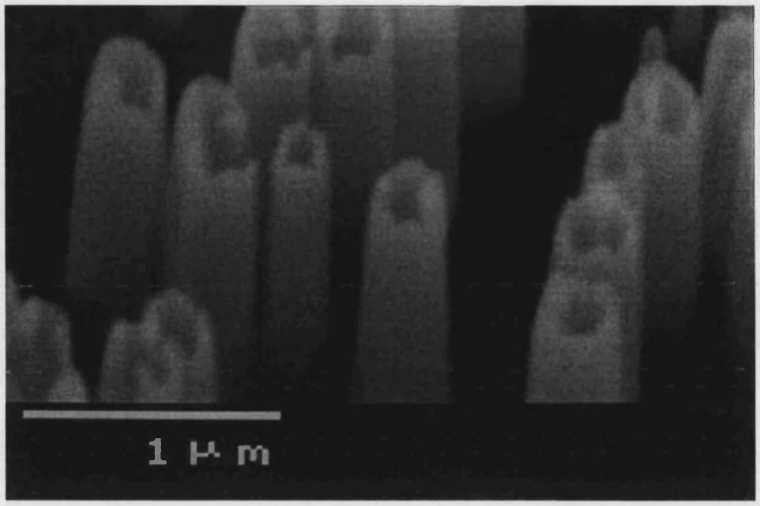

FIGURE 4.5: SEM picture of a GaN nanotube.

The inner and outer diameter for the uniform part of the nanotube is ~160 nm and ~200 nm, respectively.

The composition of the material making up the nanotubes was established by XRD, EDX and TEM electron diffraction patterns, which were obtained by focusing the electron probe at the top and bottom of the nanotube. The diffraction pattern obtained from the top and bottom part of the nanotube was the same, giving the identity of the material. A distinct GaN (0002) peak was found in the XRD trace of the sample and the diffraction pattern was consistent with GaN. Gallium and nitrogen peaks were found using EDX, confirmation that the material making up the nanotubes is GaN.

Figure 4.7 shows the AFM images of the effect of etching time at the surface. For the as-grown GaN (Figure 4.7a), the surface was smooth and flat with an RMS roughness 0.8 nm and a small pit was observed with a diameter ~50 nm. There are two lines terminated at the pit and the height of the steps is on the atomic scale. This suggested the association of a dislocation terminating at the surface [25]. After etching in a Cl_2/Ar plasma for only 5 seconds (Figure 4.7a), the surface morphology was dramatically changed. Many etch pits were observed and may be due to the presence of dislocations [19, 39]. The rough surface may be due to the preferential etching of defects and dislocations. Figure 4.7c and 4.7d illustrates the surface after etching for 10 seconds and 30 seconds. The

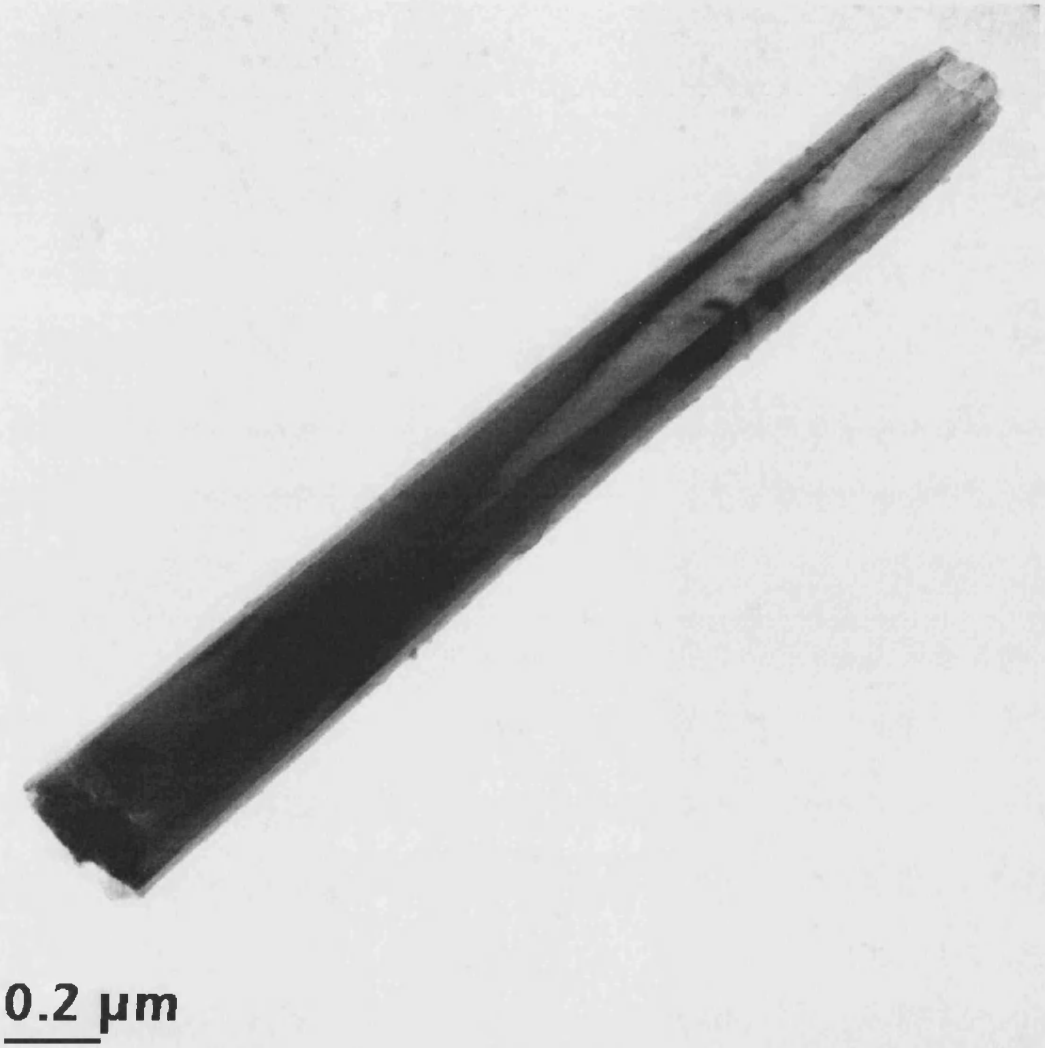

FIGURE 4.6: TEM picture of a GaN nanotube.

surface morphology remained similar but more etch pits were observed in Figure 4.7d. More and more etch pits were revealed after etching for 50 seconds and 100 seconds (Figure 4.7e, 4.7f). The observed etch pits were similar to that seen after wet etching [18, 19, 39].

AFM measurement results showed that the surface density of the etch pits for the sample etched for 50 seconds was 3.2×10^7 cm^{-2}. Note that the density of GaN nanotubes is 3.8×10^7 cm^{-2}, very close to the etch pit density. On the basis of the association of etch pits and dislocations, it implies that a dislocation is still present in the centre of the nanotube at the bottom end, which has not been etched out. Results from diffraction patterns for GaN nanotubes revealed further evidence of structural defects. The TEM diffraction pattern (Figure 4.8) showed a GaN (0002) diffraction spot associated with an extra spot adjacent to it, with an indication of streaking in the spot, indicating the existence of both twins or stacking faults and elastic strain within the structure. There are linear contrast features in the TEM image of the nanotubes which are indicative of stacking faults or micro-twins. These occur at an angle of $\sim60^o$ to the (0002) axis of the nanotube.

Masking effect of nanometre-scale etch products was first considered to explain the formation mechanism of the GaN nanotubes. This effect was first introduced in Section 3.5.3. The GaN nanotips have diameters between 10nm and 30nm and the density is approximately 8×10^9 cm^{-2}. For the GaN nanotubes presented in this chapter, the structure and the density are significantly different to the nanotips. Being a nanotube, not a nanotip, it has a hollow core and the outer diameter is 200nm, which is much larger than the nanotips, and the number density was measured to be 3.8×10^7 cm^{-2}, which is much lower than that of nanotips. In addition, the distribution of the GaN nanotubes can be aligned to certain directions (Figure 4.10). Yoshida *et al.* [37] observed structures similar to the nanotips shown in Section 3.5.3. Numerical simulation calculations for the formation of the GaN nanotips was performed by the authors and a random distribution of the nanotips was suggested. Furthermore, no GaN nanotips or nanotubes were observed for the GaN film etched in the Cl_2/Ar_2 plasma under certain etching conditions (Figure 3.12). These results suggested that the formation of GaN nanotubes may be sensitive to the etching conditions and the masking effect of nanometre-scale etch products may not be a valid explanation

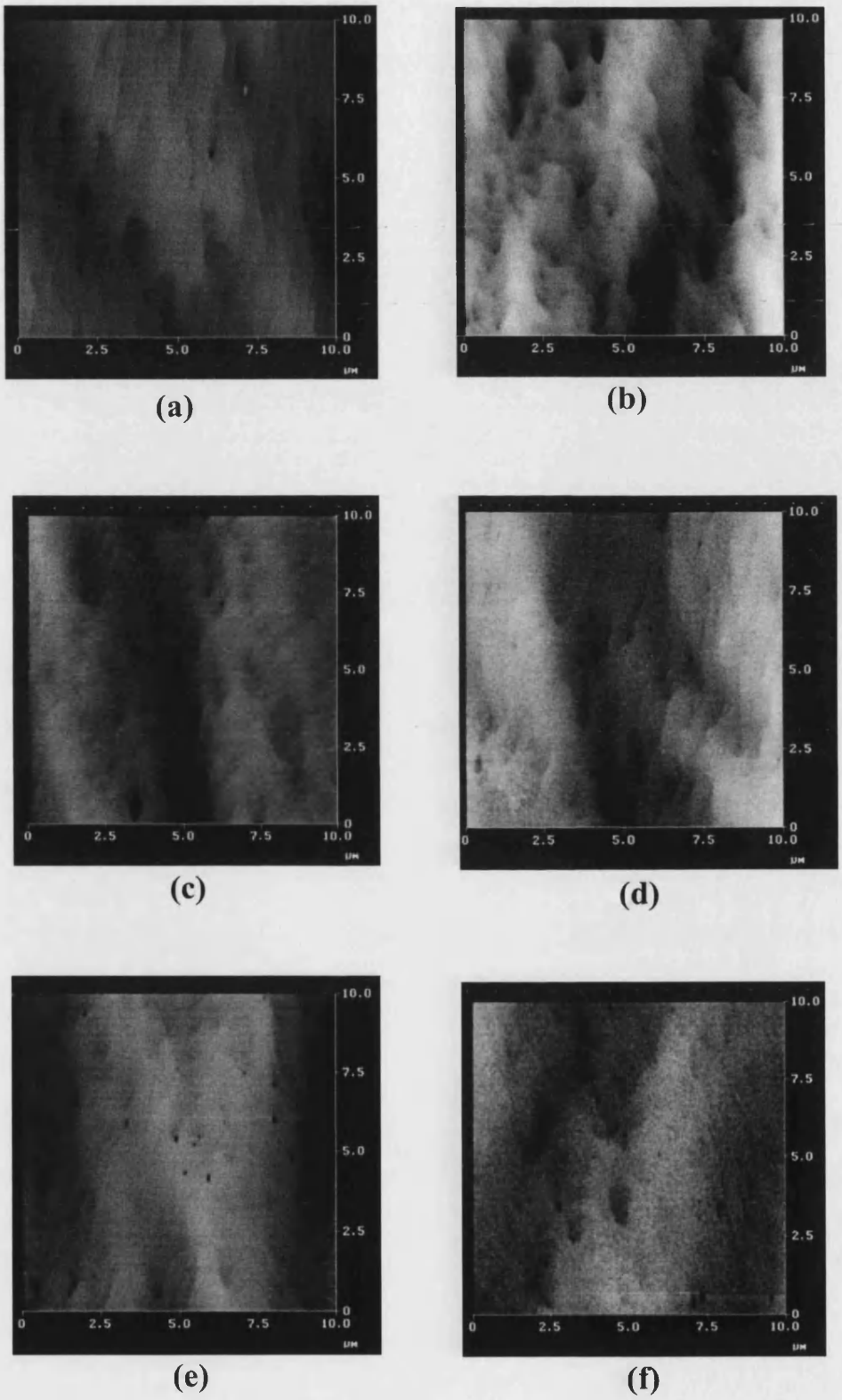

FIGURE 4.7: AFM images of a 3.8μm-thick GaN film before and after ICP etching for (a) 0 second, (b) 5 seconds, (c) 10 seconds, (d) 30 seconds, (e) 50 seconds and (f) 100 seconds. Note that the black to white scale is 15 nm.

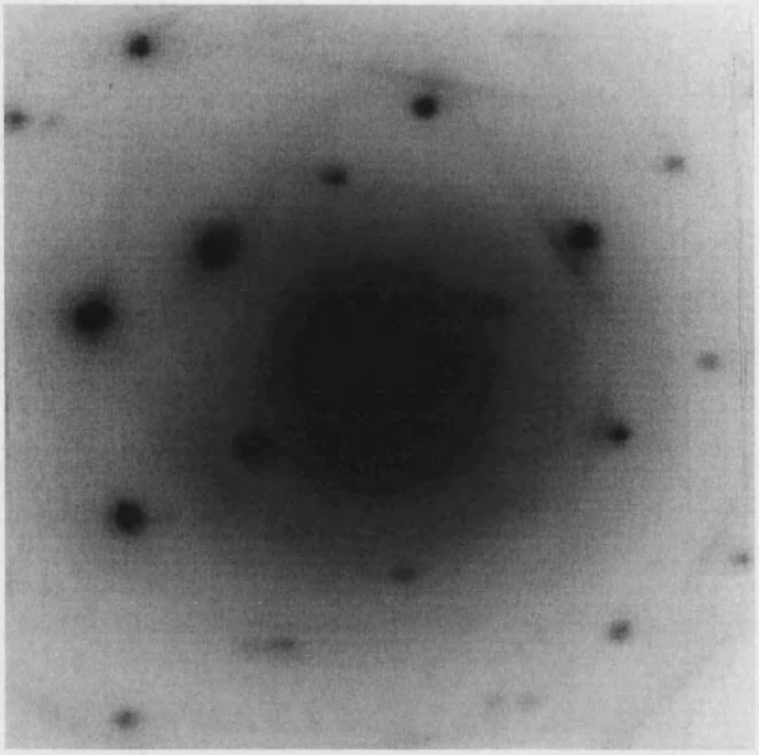

FIGURE 4.8: X-ray diffraction pattern of a GaN nanotube.

for the GaN nanotube formation. An explanation which is considered to be more feasible in this case is given below.

During the ICP etching of GaN, the etch rate appeared to be more affected by the chemical reaction (see chapter 3). It implies that the Cl^+ species contributed significantly to the etching because it is very reactive and is the dominant ion in the Cl_2 plasma [40]. The electric field, $\mathbf{E}_{DC}$, built up by the sheath potential in the sheath region extracts and accelerates the Cl^+ ions from the plasma region to bombard the sample surface (Figure 4.9a). When the Cl^+ ions approach the sample surface, they preferentially etch screw dislocations because the atoms around the dislocations are weak-bonded and there is a strong piezoelectric polarisation, $\mathbf{P}_s$, along the screw dislocations (Figure 4.9a) [24]. In Section 4.3 it was demonstrated that there is a piezoelectric polarisation inside the screw dislocations of GaN. The impinging Cl^+ ions tend to follow the piezoelectric polarisation, re-

sulting in circular motions. According to Eq. 4.6 one can deduce

$$\mathrm{div}\mathbf{P}_s = 0 \tag{4.7}$$

which is in the same form of Maxwell's equation div $\mathbf{B} = 0$. It implies that the piezoelectric polarisation has the same form as that of a magnetic field surrounding a conducting line. Based on the continuum approximation, there is no piezoelectrically induced effective charge density associated with the dislocation, either at the core or in the surrounding bulk material. It implies that the Cl^+ ions which react with the GaN surface are only affected by the piezoelectric field. The consequent circular motion may contribute to the formation of the cylindrical shape of the GaN nanotubes.

The Cl^+ ions accumulated in the vicinity of the individual dislocations will bend the path of incoming Cl^+ ions. When the depth of the etched out hollow core of the dislocation reaches a certain value, the etch rate would gradually degrade because of repelling electrical force due to the accumulated charges residing within the core of the nanotube on the incoming Cl^+ ions and redeposition of etching products. The curved top of the nanotubes may be due to the shape of the etching ion path from a certain point a short distance above the top of the nanotubes. In addition, the formation of the wall of the nanotubes was the result of much lower horizontal etch rate. It was possibly due to the repelling force from the Cl^+ ions inside the nanotubes and anisotropic etching in this process. The piezoelectric polarisation in the original dislocations contributed to the cylindrical shape of the nanotubes.

To confirm the mechanism of nanotube formation, artificially introduced dislocations were generated by scratching along the GaN slip plane $(10\bar{1}0)$. Subsequently, the sample was etched for 300 seconds under the conditions specified above. It is clear that large populations of nanotubes are generated protruding from the sites of these newly introduced dislocations (Figure 4.10). The result provides strong support to our explanation that the formation of the nanotubes is due to the presence of the original dislocations.

The formation of column structures after ICP etching has been observed (see

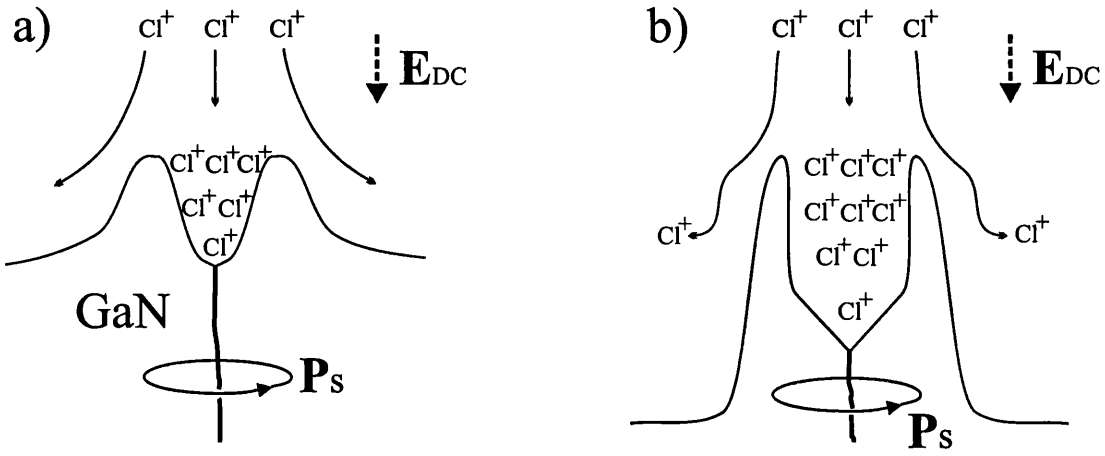

FIGURE 4.9: Etching at different times: (a) etching at an early stage, and (b) etching at the final stage.

Section 3.5.3). It may be attributed to the re-deposition of the sputtered SiO_2 particles on the GaN surface .

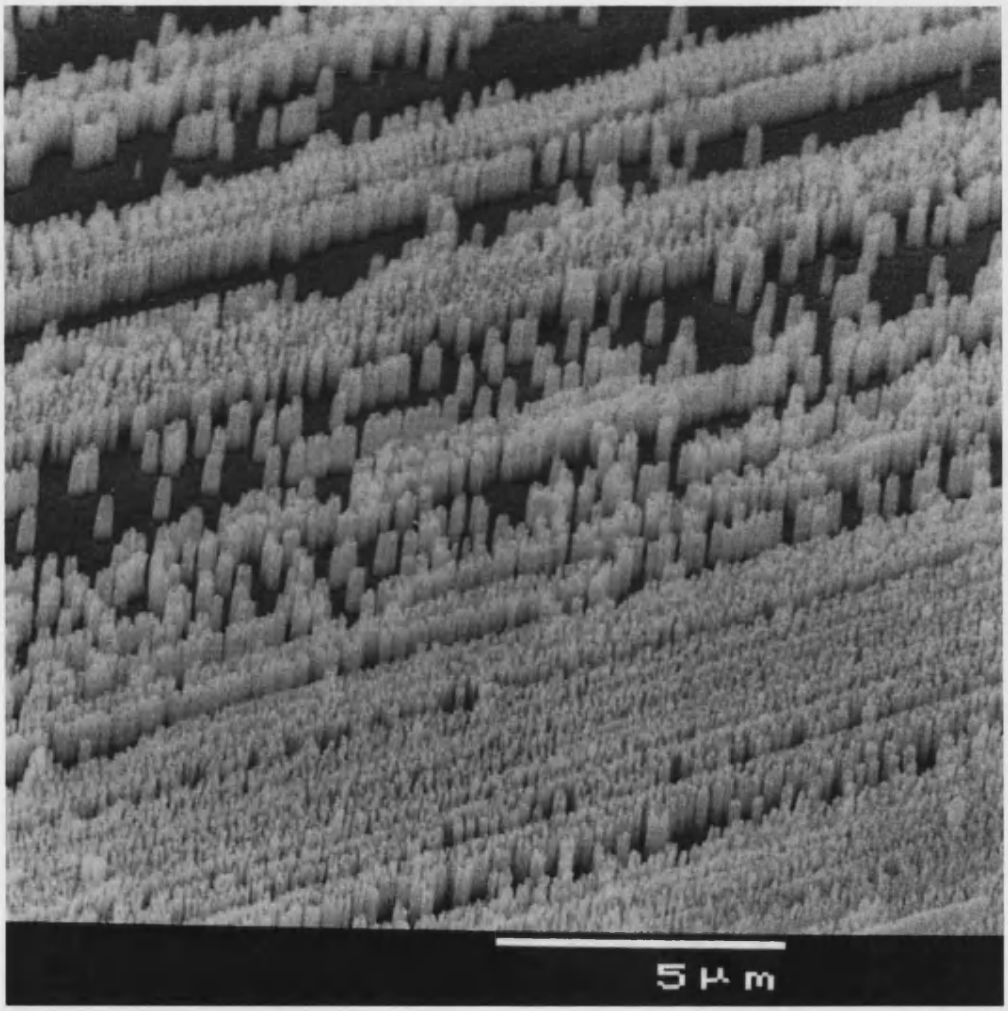

FIGURE 4.10: SEM image of GaN nanotubes protruding from the GaN film, aligned along the $(10\bar{1}0)$ scratch direction.

4.5 Characterisation of Field Emission from GaN Nanotubes

4.5.1 Introduction

Field emission is the process whereby electrons tunnel through a barrier in the presence of an electric field which is high enough to penetrate the barrier. The theory of field emission from metals was first derived by Fowler and Nordheim [30] in 1928, who assumed that most of the emitted electrons originate from a small energy interval around the Fermi level of the metal if the temperature is not too high. According to their theory, the barrier height between the material and vacuum and the electric field acting on the material determines the characteristics of the field emission process for this material. The barrier height is related to the electron affinity and Fermi level, which are determined by the nature of materials, while the electric field acting on the electrons inside the material determine the thickness of the barrier. Because tunnelling processes of electrons is the main mechanism for the field emission, the applied electric field has to be high enough to reduce the barrier thickness to stimulate the tunnelling processes. In addition, it is well-known that a sharper surface has a higher electric field according to Gauss's law. This effect, or geometric field enhancement effect, can increase the field emission current. Hence, it is of interest to have sharp emission surface, *e.g.*, nanotubes, for field emission tips.

III-V nitrides are of interest for the fabrication of cold cathode field emitters because they exhibit the property of low electron affinity. The electron affinity of GaN was reported to be 3.3 eV [26]. Negative electron affinity was found in caesiated GaN [26]. An alternative method to 'engineer' a decrease in the turn-on electric field can be achieved by modifying the surface microstructure. Forming a network of upstanding whiskers or nanotubes on the semiconductor surface provides sites for geometric field enhancement to occur. The field enhancement present at the tip of a single whisker compared with a smooth surface can increase the value of an externally applied electric field at which electrons are extracted from the conduction band. This occurs because the field enhancement induces very strong band bending at the semiconductor-vacuum interface, this causes a

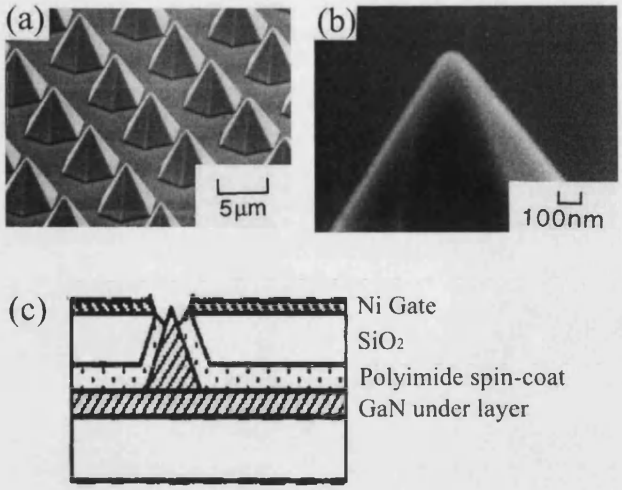

FIGURE 4.11: (a) GaN pyramid array, (b) tip of GaN pyramid, and (c) Gated GaN pyramid structure [27].

narrowing of the vacuum barrier allowing electrons to tunnel more easily from the conduction band into the vacuum.

Kozawa *et al.* [27] have fabricated gated GaN and $Al_{0.1}Ga_{0.9}N$/GaN pyramidal field emitter arrays using a self-aligned process (Figure 4.11). The sharp pyramidal emitters were obtained by selective growth techniques. SiO_2 and polyamide were used as the insulating layer between the GaN under layer and the top Ni gate. A low onset gate voltage of 42V was obtained for a gate-tip spacing of 0.4 μm. This achievement is mainly due to the geometric field enhancement and the short distance between gate-tip spacing. Sugino *et al.* [28] used H_2 plasma etching to roughen the GaN surface from RMS surface roughness 1nm to 17.9nm. There is no current measured for the as-grown GaN sample for the voltage of anode 4000V, while the roughened sample gave the threshold voltage 1550V. The improvement was considered to be the geometric field enhancement induced by the rough surface.

Nanotubes are an exciting new development of materials and many varied applications are foreseen in mechanics [9], chemistry [6, 7] and electronics [12, 13]. They are of particular interest for cold cathode emitters because of the high geometric field enhancement factor. The fabrication of GaN nanotubes has been successfully demonstrated by the technique described in this chapter. In the fol-

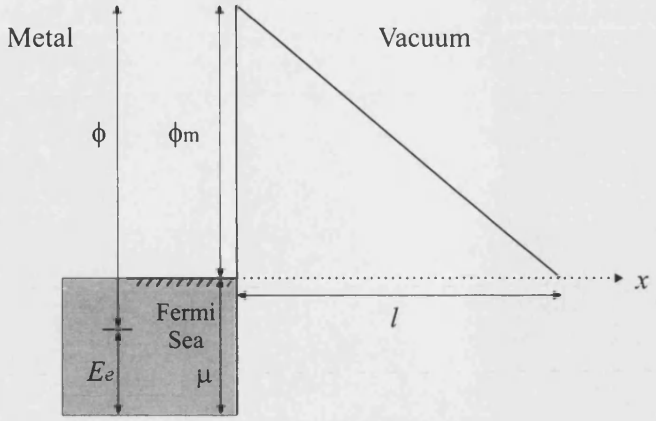

FIGURE 4.12: Schematic of an energy diagram for a metal–vacuum interface. Note that the barrier height (ϕ) for the electrons of kinetic energy E_e is $\phi = \phi_m + \mu - E_e$.

lowing experimental work, n-GaN nanotubes were produced and the field emission properties were characterised.

4.5.2 Basics of Field Emission

When an electric field F is applied to the surface of a metal, electrons of kinetic energy E_e, which depends on the energy level the electrons situated, along the emission direction see a barrier of height $\phi = \phi_m + \mu - E_e$ (Figure 4.12), where ϕ_m and μ are the work function and the energy of Fermi level of the metal, respectively. If the barrier is thin enough, tunnelling of electrons will occur with finite probability. Heisenberg's uncertainty principle may be applied to the electrons near the Fermi level because tunnelling is a quantum mechanism. The electron momentum corresponding to a barrier height ϕ is given by $\sqrt{2m\phi}$ and the barrier width is $\left(\frac{\phi}{eF}\right)$. Placing these two values into the uncertainty expression gives

$$\begin{aligned} \left(\frac{\phi}{eF}\right)\sqrt{2m\phi} &\cong \frac{\hbar}{2} \\ 2\sqrt{\frac{2m}{\hbar^2}}\frac{\phi^{3/2}}{eF} &\approx 1 \end{aligned} \tag{4.8}$$

This gives the condition required for field emission through the triangle potential barrier. Solving the one-dimensional Schrödinger equation $\frac{d^2\Psi}{dx} + \frac{2m}{\hbar^2}[E - V]\Psi = 0$ where V and E are the electron's potential and kinetic energies, respectively. The penetration coefficient *D(E,V)*, which is the probability that an electron travelling to the right will not be turned back at the barrier but proceed through it, can be obtained:

$$D(E,V) = f(E,V)\exp\left[-2\sqrt{\frac{2m}{\hbar^2}}\int_0^l (V-E)^{1/2}dx\right] \tag{4.9}$$

Assuming that there is no image force induced band bending, the term $\int_0^l (V-E)^{1/2}dx$ is close to the area of a triangle with base $l = \frac{(\phi_m + \mu - E_e)}{FE}$ and height $(\phi_m + \mu - E_e)$. Substituting the integral Eq. 4.9 becomes

$$D(E,V) = f(E_e,V)\exp\left[-\left(\frac{2m}{\hbar^2}\right)^{1/2}\frac{(\phi_m + \mu - E_e)^{3/2}}{eF}\right]$$

which is a similar form to that calculated by Fowler and Nordheim [30],

$$\begin{aligned} D(E,V) &= \frac{4\left[E_e(\phi_m + \mu - E_e)\right]^{1/2}}{(\phi_m + \mu)} \\ &\quad \exp\left[-\frac{4}{3}\left(\frac{2m}{\hbar^2}\right)^{1/2}\cdot\frac{(\phi_m + \mu - E_e)^{3/2}}{eF}\right] \end{aligned} \tag{4.10}$$

Restricting the range of electron kinetic energies to those approximately equal to the Fermi energy level by putting $E_e = \mu$ in Eq. 4.10 gives

$$D(E,V) = \frac{4(\phi_m\mu)^{1/2}}{(\phi_m + \mu)}\exp\left[-6.8\times10^7\frac{{\phi_m}^{3/2}}{F}\right] \tag{4.11}$$

for μ_m in volts and F in volts per centimetre. The emitted current density (J) can be approximated by multiplying Eq. 4.10 by the total rate of arrival of electrons,

or

$$J = 6.2 \times 10^6 \frac{(\mu/\phi_m)^{1/2}}{\mu + \phi_m} F \exp\left[-6.8 \times 10^7 \frac{{\phi_m}^{3/2}}{F}\right] \quad \text{A/cm}^2 \quad (4.12)$$

4.5.3 The Fowler-Nordheim Plot

Assuming $\mu \approx E_e$ and the field $F = \beta V/d$, where β represents the field enhancement factor, V and d is the applied potential and the distance between anode and cathode. Eq. 4.12 can be rewritten in the form

$$i = \left(\frac{AB_1}{\phi_m}\right)\left(\frac{\beta V}{d}\right)^2 \exp\left(\frac{-dB_2{\phi_m}^{3/2}}{\beta V}\right) \quad (4.13)$$

where B_1 and B_2 are physical constants. Taking the natural logarithm of both sides of the equation,

$$\ln\left(\frac{i}{V^2}\right) = \ln\left(\frac{AB_1\beta}{\phi_m d^2}\right) - \frac{1}{V}\left(\frac{dB_2{\phi_m}^{3/2}}{\beta}\right) \quad (4.14)$$

The plot $\ln(i/V^2)$ against $1/V$ is called the Fowler-Nordheim (F-N) plot [30]. The field enhancement factor β and emission area are then estimated from this plot.

4.5.4 Experiment

The n-GaN samples used in this study were grown on (0001) sapphire by MOCVD. The Si-doped n-GaN thickness was 740 nm. Hall measurements showed the electron concentration was 3×10^{18} cm^{-3}. The fabrication process has been described in Section 4.4.1. The etching time is reduced because the thickness of the GaN film is thinner. Atomic force microscopy (AFM) and scanning electron microscopy (SEM) were used to image the surface morphology.

Electron field emission measurements were conducted in an ultrahigh vacuum chamber. During the measurement, the chamber pressure was kept below 10^{-6} Torr. The measurement setup is illustrated in Figure 4.13. Emission current versus applied voltage (I-V) was characterised by varying the voltage from 0 to 2500 V. The anode to cathode gap was altered to allow measurements to be made with different electrode spacing. A conductive ITO-glass screen was used as the anode plate. The anode to cathode separation was controlled by the use of spherical glass spacers placed between each corner of the sandwiched substrates. I-V measurements were obtained with a computer controlled Brandenburg Alpha III, high voltage power supply and a Keithley 2000 multimeter.

4.5.5 Results and Discussion

Surface morphology of as-grown and etched samples is shown in Figure 4.14. A smooth surface was observed for as-grown n-GaN and the surface roughness was 1.7 nm. Figure 4.15 is an SEM image of n-GaN etched for 3 minutes. The density of nanotubes was $5.9\times\ 10^{7}$ cm^{-2}. The average dimensions of n-GaN nanotubes were approximately 600 nm for the height, 300 nm for the outer diameter, and 200 nm for the inner diameter. The formation mechanism of GaN nanotubes was mainly attributed to the dislocations and the piezoelectric field. Details are given in section 4.4.2.

Figure 4.16 shows the field emission characteristics of as-grown and etched n-GaN . The turn-on electric field was measured to be 74.6 V/μm. After being treated with ICP etching, the turn-on electric field was dramatically reduced to 24.9 V/μm. Hence, the contribution of etching-induced change was significant.

Figure 4.17 shows the band diagram for a n-type semiconductor. When a strong field is applied to the material, the conduction band minimum (CBM)may be bent to the energy level lower than Fermi level. Consequently, a 'pool' of elections will collect in this depression of the CBM. The metallic nature of the electron pool indicates that Eq. 4.12, originated from the Fowler-Nordheim theory [30], is considered applicable.

Figure 4.18 shows the F-N plot for as-grown GaN and GaN nanotubes. A linear distribution has been obtained for these two samples, which is consistent with the Fowler-Nordheim theory. According to Eq. 4.14, the slope S of the straight trend line in this plot is proportional to d/β, assuming that the physical constants and work function are identical or

$$S \propto \frac{d}{\beta} \tag{4.15}$$

The field enhancement factor β for the GaN nanotubes was then estimated based on this equation. It was found that the value of β is ~5 times higher than that for the as-grown GaN, indicating that the small emitter size of the GaN nanotubes contributes to the lower electric field required for field emission.

By comparing the intercepts (ζ) in the Fowler-Nordheim plot, the emission area for these two samples can be deduced, or

$$A = \frac{\exp(\zeta)\phi_m d^2}{B_1 \cdot \beta} \tag{4.16}$$

Denoting the as-grown n-GaN as 'a' and the n-GaN nanotubes as 'b' and assuming no change in the work function of n-GaN after etching since a stoichiometric etched surface was reported after high density plasma ECR etching [42], the ratio of intercepts becomes

$$\frac{A_a}{A_b} = \frac{\exp(\zeta_a){d_a}^2\beta_b}{\exp(\zeta_b){d_b}^2\beta_a} = 50 \tag{4.17}$$

Estimating the area ratio from the SEM image (Figure 4.15) one can obtain a ratio of ~43, indicating a good agreement to the deduced value from Fowler-Nordheim theory. The result shows that the majority of the electrons may be emitted from the GaN nanotubes.

4.6 Summary

GaN nanotubes have been fabricated by ICP etching of MOCVD GaN films. The GaN nanotubes formed under the conditions of chamber pressure=15mTorr, ICP power=200W, RF power=250W, Cl_2/H_2=50/12sccm and the stage temperature 29 °C with a ramp-up rate of 2.6 °C/min. The shape of the nanotubes is that of a regular cylinder outside and the uniform hollow part extends 1 μm from the top of the tube and then becomes narrower. The inner and outer diameter of the uniform part of the nanotube is ~160 nm and ~200 nm, respectively. All GaN nanotubes were single crystal with the alignment of c-axis.

XRD, EDX and TEM electron diffraction patterns showed the composition of the material making up the nanotubes is single crystal GaN containing defects and dislocations. The stacking faults or micro-twins can be seen in TEM pictures. AFM images revealed the etching pits and the density was estimated to be 3.2×10^7 cm^{-2} which is very close to the density of GaN nanotubes 3.8×10^7 cm^{-2}.

The formation of GaN nanotubes may be aided by the electric field induced by the sheath potential and piezoelectric field induced by dislocations. These two fields affect the motion of reactive ion Cl^+ in the vicinity of GaN surface. The energetic reactive ions preferentially etch the dislocations and piezoelectric field induces a circular motion for these ions, resulting in the formation of cylindrical hollow core. The formation of the walls of these GaN nanotubes is believed to be the repellency of reactive ions from the ions inside the cylindrical hollow cores.

Confirmation of the formation mechanism has been achieved by artificially inducing dislocations along the GaN slip plan $(10\bar{1}0)$. After ICP etching for 300 seconds, large population of nanotubes were formed from the site of these newly introduced dislocations. It provides strong support to the explanation that the formation of the nanotubes is due to the presence of the dislocations.

One application of GaN nanotubes, field emission tips, was explored. The GaN nanotubes used in this study were n-type with the electron concentration at 3×10^{18} cm^{-3},average height 600 nm, and inner diameter 100 nm with a wall

thickness of 100 nm. The turn-on electric field was dramatically reduced from 74.6 V/μm for the as-grown n-GaN to 24.9 V/μm for the n-GaN nanotubes, indicating the contribution of the etching process. A Fowler-Nordheim plot was established and a linear characteristic was obtained, showing consistency with the Fowler-Nordheim theory. The field enhancement factor for the GaN nanotubes were estimated based on the slope in the Fowler-Nordheim plot and to be $\sim$5 times higher than that of the as-grown GaN. By comparing the intercepts in the Fowler-Nordheim plot the ratio of the emission area ($A_{as-grown}/A_{nanotubes}$) is estimated to be 50. This ratio is in a good agreement with the value extracted from the SEM image, implying that the majority of the emitted elections may be from the tips of the GaN nanotubes.

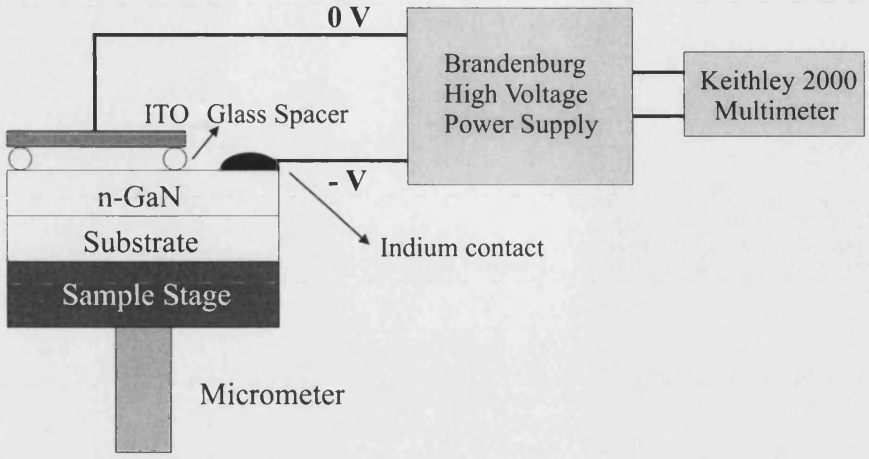

FIGURE 4.13: Schematic for the field emission measurement.

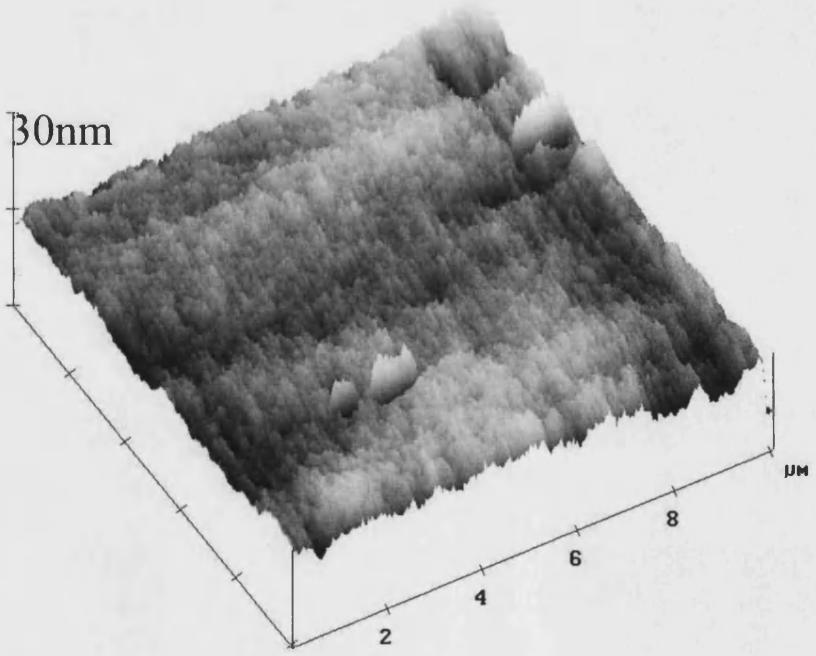

FIGURE 4.14: AFM image of the surface morphology for as-grown n-GaN.

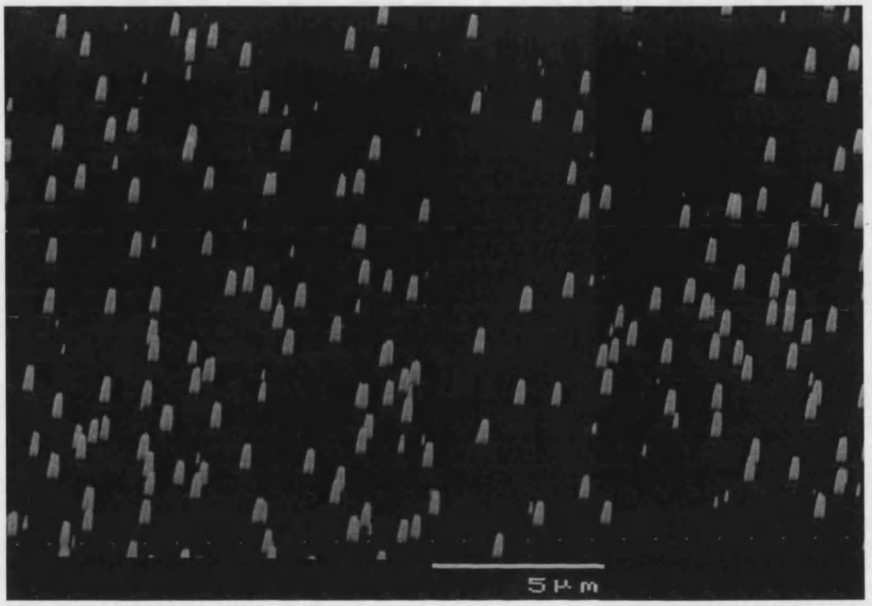

FIGURE 4.15: SEM image of the n-GaN nanotubes.

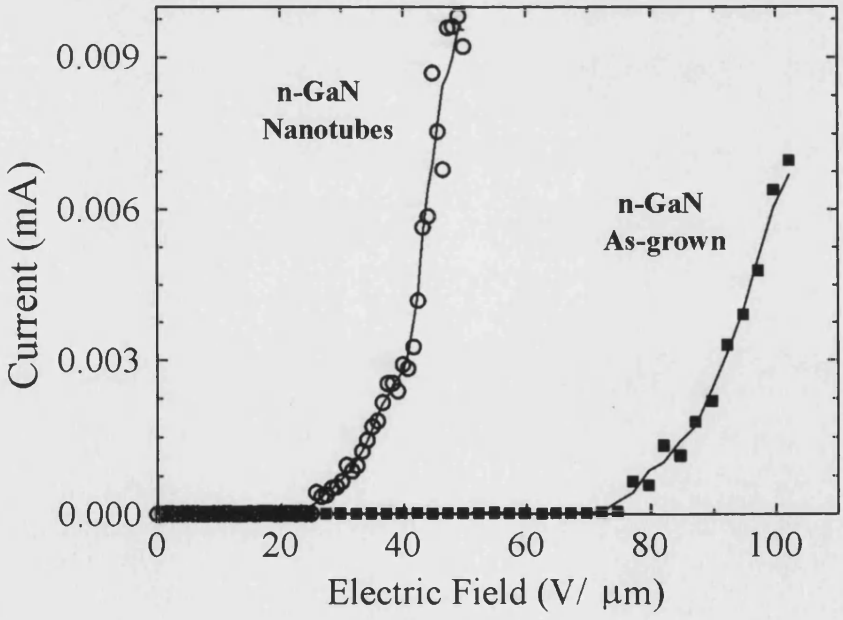

FIGURE 4.16: Field emission I-V characteristics of as-grown n-GaN and n-GaN nanotubes.

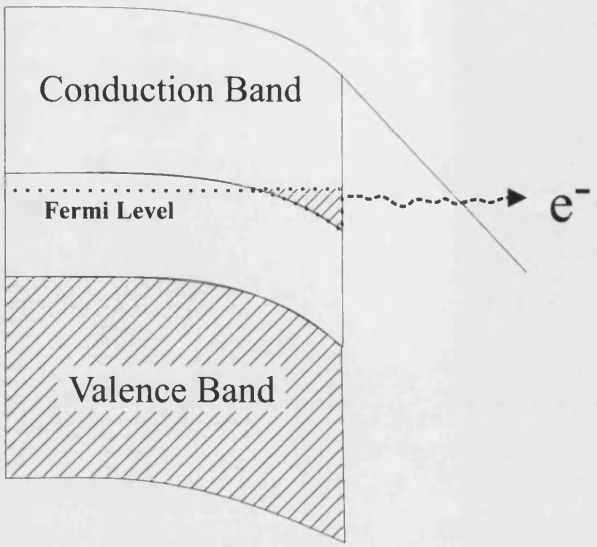

FIGURE 4.17: Field emission from the vicinity of the conduction band of a semiconductor.

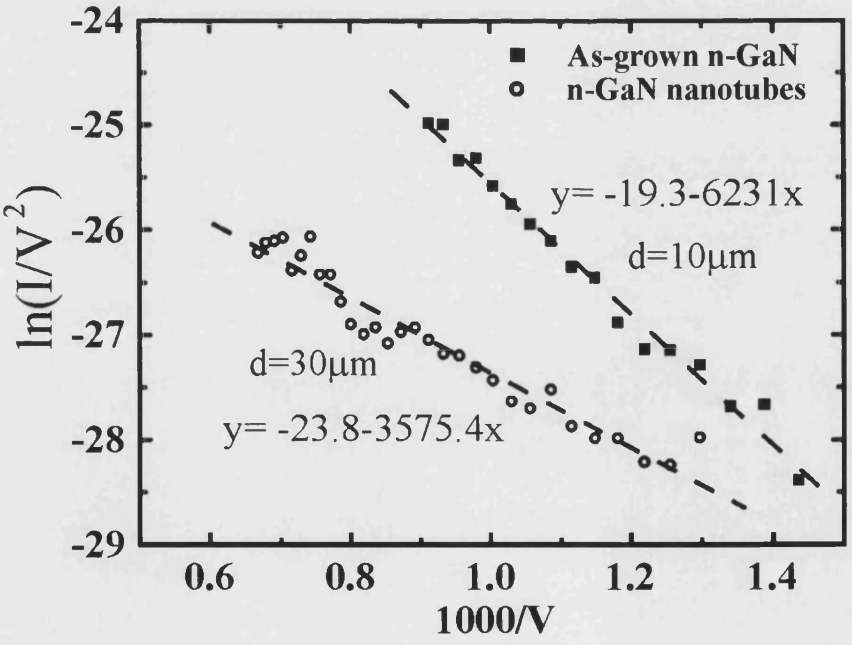

FIGURE 4.18: Fowler-Nordheim plot for as-grown GaN and GaN nano-tubes.

References

[1] S. Iijima, *Nature (London)* **354**, 56 (1991).

[2] G. Che, B. B. Lakshmi, C. R. Martin, E. R. Fisher,R. S. Ruoff, *Chem. Mater.* **10**, 260 (1998).

[3] T. W. Ebbesen, and P. M. Ajayan, *Nature* **358**, 220 (1992).

[4] R. S. Lee, H. J. Kim, J. E. Fischer, A. Thess, and R. E. Smalley, *Nature* **388**, 255 (1997).

[5] W. Q. Han, S. S. Fan, Q. Q. Li, Y. D. Hu, *Science* **277**, 1287 (1997).

[6] M. Freemantle,*Chem. Eng. News* **74**, 62 (1996).

[7] A. C. Dillon, K. M. Jones, T. A. Bekkedahl,C. H. Kiang, D. S. Bethune, and M. J. Heben, *Nature* **386**, 377 (1997).

[8] A. G. Rinzler, J. H. Hafner, P. Nikolaev, L. Lou, S. G. Kim, D. Tománek, P. Nordlander, D. T. Colbert, and R. E. Smalley, *Science* **269**, 1550 (1995).

[9] G. D. Zhan, J. D. Kuntz, J. L. Wan, and A. K. Mukherjee , *Nature Materials* **2**, 38 (2003)

[10] H. Dai, J. H. Hafner, A. G. Rinzler, D. T. Colbert, and R. E. Smalley, *Nature* **384**, 147 (1996).

[11] S. S. Wong, J. D. Harper, P. T. Lansbery, and C. M. Lieber, *J. Am. Chem. Soc.* **120**, 603 (1998).

[12] W. B. Choi, D. S. Chung, J. H. Kang, H. Y. Kim, Y. W. Jin, I. T. Han, Y. H. Lee, J. E. Jung, N. S. Lee, G. S. Park, and J. M. Kim, *Appl. Phys. Lett.* **75**, 3129 (1999).

[13] J. L. Kwo, M. Yokoyama, C. C. Lee, F. Y. Chuang, and I. N. Lin, *J Vac Sci Technol B* **19** , 1023 (2001).

[14] D. S. Bethune, C. H. Kiang, M. S. de Vires, G. Gorman, R. Savoy, J. Vazquez, and R. Beyers, *Nature* **363**, 605 (1993).

[15] I. Akasaki, H. Amano, Y Koide, K. Hiramatsu, and N.Sawaki, *J. Cryst. Growth* **98**, 209 (1989).

[16] W. Qian, M. Skowronski, M. De Graef, K. Doverspike, L. B. Rowland, and D. K. Gaskill, *Appl. Phys. Lett.* **75**, 3129 (1999).

[17] W. Qian, M. Skowronski, K. Doverspike, L. B. Rowland, and W. J. Choyke, *J. Cryst. Growth* **151**, 396 (1995).

[18] C. Youtsey, L. T. Romano, R. J. Molnar, and I. Adesida, *Appl. Phys. Lett.* **74**, 3537 (1999).

[19] P. Visconti, K. M. Jones, M. A. Reshchikov, R. Cingolani, H. Morkoç, and R. J. Molnar, *Appl. Phys. Lett.* **77**, 3532 (2000).

[20] S. P. Łepkowski, H. Teisseyre, T. Suski, P. Perlin, N. Grandjean, and J. Massies, *Appl. Phys. Lett.* **79**, 1483 (2001).

[21] E. K. Sichel, and J. I. Pankove, *J. Phys. Chem. Solids* **38**, 30 (1977).

[22] J. P. Hirth and J. Lothe, *Theory of Dislocations* (McGrawHill, New York, 1968), p.p60.

[23] W. G. Cady, *Piezoelectricity* (Dover, New York, 1964), Chap. VIII.

[24] Changchun Shi, Peter M. Asbeck, and Edward T. Yu, *Appl. Phys. Lett.* **74**, 573 (1999).

[25] R. S. Qhalid Fareed, S. Juodkazis, S. H. Chung, T. Sugahara, and S. Sakai, *Materials Chemistry & Physics* **64**, 260 (2000).

[26] C. I. Wu and A. Kahn, *Appl. Surf. Sci.* **162-163**, 250 (2000).

[27] T. Kozawa, T. Ohwaki, Y. Taga, and N. Sawaki, *Appl. Phys. Lett.* **75**, 3330 (1999).

[28] T. Sugino, T. Hori, C. Kimura, and T. Yamanoto, *Appl. Phys. Lett.* **78**, 3229 (2001).

[29] W. B. Chou, D. S. Chung, J. H. Kang, H. Y. Kim, Y. W. Jin, I. T. Han, Y. H. Lee, J. E. Jung, N. S. Lee, G. S. Park, and J. M. Kim, *Appl. Phys. Lett.* **75**, 3129 (1999).

[30] R. H. Fowler, and L. W. Nordheim, *Proc. Roy. Soc. (London) A* **119**, 173 (1928).

[31] P. M. Ajayan, and T. W. Ebbesen, *Rep. Prog. Phys.* **60**, 1025 (1997).

[32] J. P. Salvetat, J. M. Bonard, N. H. Thomson, A. J. Kulik, and L. Forró, W. Benoit, L. Zuppiroli, *Appl. Phys. A* **69**, 255 (1999).

[33] J. Hone, M. Whitney, C. Piskoti, and A. Zettl, *Phys. Rev. B* **59**, R2514 (1999).

[34] R. S. Lee, H. J. Kim, J. E. Fisher, A. Thess, and R. E. Smalley, *Nature (London)* **388**, 255 (1997).

[35] S. C. Tsang, Y. K. Chen, P. J. F. Harris, and M. L. H. Green, *Nature (London)* **372**, 159 (1994).

[36] P. J. Britto, K. S. V. Santhanam, and P. M. Ajayan, *Bioelectrochem. Bioenerget.* **41**, 121 (1996).

[37] H. Yoshida, T. Urushido, H. Miyake, and K. Hiramatsu, *Jpn. J. Appl. Phys.* **40**, L1301 (2001).

[38] R. R. Reeber, and K. Wang, *MRS Internet J. Nitride Semicond. Res.* **6**, 3 (2001).

[39] T. Hino, S. Tomiya, T. Miyajima, K. Yanashima, S. Hashimoto, and M. Ikeda, *Appl. Phys. Lett.* **76**, 3421 (2000).

[40] M. V. Malyshev, and V. M. Donnelly, *J. Appl. Phys.* **88**, 6207 (2000).

[41] R. Stratton, *Phys. Rev.* **125**, 67 (1962).

[42] Charles R. Eddy, Jr., *MRS Internet J. Nitride Semicond. Res.* **4S1**, G10.5 (1999)

Chapter 5

High Efficiency GaN-based Light Emitting Diodes

5.1 Introduction

Light emitting diodes (LEDs) have been widely used since the 1960s [1]. The operating voltage and current of LEDs are low, typically 1.5 – 4 V and 10 – 20 mA, indicative of a low power consumption; they can be produced to a very small size, and so can be considered as point sources of light. These characteristics have made them a desirable light source for mobile electronic devices. The emission spectrum of LEDs is relatively narrow, and they can be switched on and off on the order of 10ns. These properties are attractive for applications in optical data communication. In addition, LEDs are cold lamps and they can be designed to give more directional light. These characteristics reduce the pollution of heat and light to the environment.

The applications of LEDs have dramatically increased since the 1990s because blue and green LEDs have been readily available since then. Full colour LED displays [2] and traffic lights [3] have been commercialised. Another important application of LEDs is to producing white light sources. Commercially a blue LED is used to excite phosphors coated either on the top or bottom of the LED

[4]. The blue and yellow colour mixture gives white light. Because the packing of LED white light sources is very small, the application in the backlighting of LCD screens has been commercialised [5]. For the applications described above, high brightness LEDs are clearly desirable. In this chapter, one design for p-GaN ohmic contacts was aimed to achieve highly efficient current spreading and light extraction, which results in a stronger light emission.

5.2 LED Operational Theory

LEDs are semiconductor p-n junctions that under proper forward-biased conditions can emit external spontaneous radiation in the ultraviolet, visible, and infrared regions of the electromagnetic spectrum. A p-n junction consists of a p-type semiconductor, which has extra 'holes' inside the material, and a n-type semiconductor, which has extra electrons inside the material. In an intrinsic semiconductor, the Fermi level is given by [6]

$$E_F = \frac{E_g}{2} + \frac{3}{4} k_B T \ln\left(\frac{m_h^*}{m_e^*}\right) \tag{5.1}$$

where E_g is the bandgap energy, k_B is the Boltzmann constant, T is temperature and m_h^* and m_e^* are the effective hole and electron masses, respectively. When dopants are introduced to the semiconductors, the Fermi level is then changed. This energy level, named the quasi-Fermi level, in a doped semiconductor is given by [6]

$$\begin{aligned} E_{Fn} &= E_F + k_B T \ln\left(\frac{n_i}{N_i}\right) \\ E_{Fp} &= E_F + k_B T \ln\left(\frac{p_i}{N_i}\right) \end{aligned} \tag{5.2}$$

where E_{Fn} and E_{Fp} are the quasi-Fermi level in the n-doped and p-doped semiconductor, respectively, and n_i, p_i, and N_i are the carrier concentrations of n-doped,

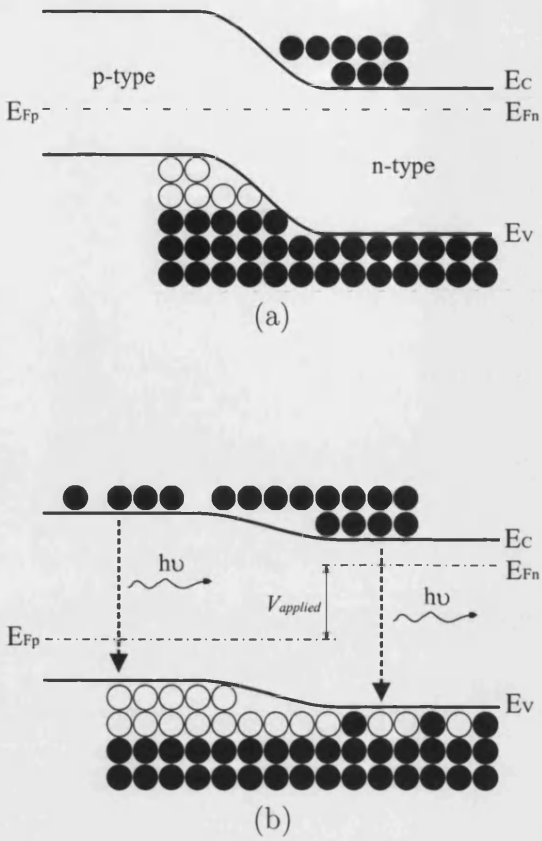

FIGURE 5.1: Carrier distribution in p-n junction under (a) zero and (b) forward bias.

p-doped and an intrinsic semiconductor, respectively. When these two semiconductors are brought together, a thermal equilibrium condition, which aligns the Fermi level, is established. According to Eq. 5.2 it is seen that the valence and conduction band have to shift to compensate the difference in the quasi-Fermi level (Figure 5.1a). When a forward bias ($V_{applied}$) is applied to a p-n junction, the quasi-Fermi level in the n-side is moved up relatively to that of the p-side and subsequently the electrons in the n-type side have sufficient energy to move across the junction to the p-type side (Figure 5.1b).

In order to restore the thermal equilibrium condition, recombination of electrons and holes take place. The possible recombination processes for a single level system are (Figure 5.2):

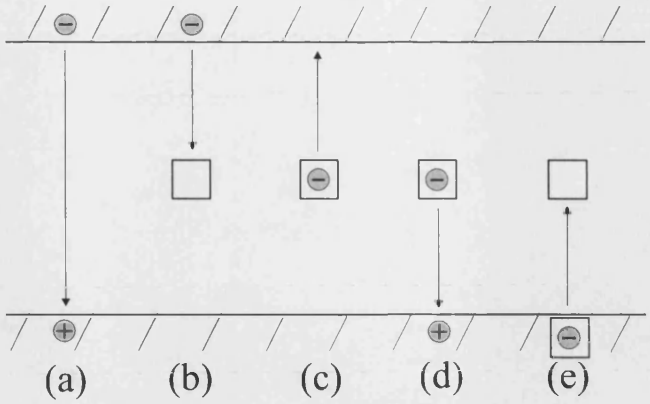

FIGURE 5.2: Illustration of a the recombination of carriers for a semiconductor: (a) band-to-band recombination, (b) electron capture, (c) electron emission, (d) hole capture, and (e) hole emission.

(a) band-to-band recombination,
(b) electron capture,
(c) electron emission,
(d) hole capture,
(e) hole emission.

In order to see the effect of trapped energy levels, a simplified condition, which assume a single level system and the hole and electron capture cross sections $\sigma_n = \sigma_p = \sigma$, is considered. The recombination rate (U) is given by [6]

$$U = \sigma v_{th} N_t \frac{p_i n_i - {N_i}^2}{n_i + p_i + 2N_i \cosh\left(\dfrac{E_t - E_F}{k_B T}\right)} \quad \text{cm}^{-3}/\text{s} \tag{5.3}$$

where v_{th} is the carrier thermal velocity, N_t is the trap density, and E_t is the trap energy level. It is seen that the recombination rate approaches a maximum as the energy level of the recombination centre approaches the middle of the bandgap, *i.e.* $E_t \approx E_F$. Thus, the most effective recombination centres are those located near the middle of the bandgap.

5.2.1 Internal Radiation

For a given input excitation energy, the radiative recombination process is in direct competition with the non-radiative process which may be induced by dopants, defects and dislocations. Hence, higher rates of radiative recombination process are desirable for LEDs. The band-to-band recombination is the dominant radiative mechanism in the electroluminescence LEDs. Thus, the corresponding emission wavelength (λ) is given by,

$$\lambda = \frac{hc}{E_g} = \frac{1.24}{E_g}\ \mu\text{m} \tag{5.4}$$

where h is Planck's constant and c is the speed of light.

Consider an LED in which the intrinsic, quasi-Fermi and trap levels are identical under forward biasing and intermediate current injection condition. Based on Eq. 5.3 the energy of radiative emission is given by

$$\begin{aligned} E_{rad} &= \int U_{rad}\, \mathrm{d}x \cdot A \cdot t \cdot h\nu \\ E_{rad} &\propto N_i \cdot A \propto i \cdot A \end{aligned} \tag{5.5}$$

where the subscription "rad" denotes the radiative recombination, A is the area of the active region, t is the time and I is the injection current. It is seen that the light emission power is proportional to the current injection and experimental works have shown the agreement (Figure 5.3) [14, 13]. According to Eq. 5.5, the condition for increasing the light emission power in the same LED structure is to increase either the injection current or the area of the active region.

5.2.2 Light Extraction from LED Structures

When light is generated in the active region, it starts to propagate inside the semiconductors. There are three loss mechanisms which reduce the intensity of

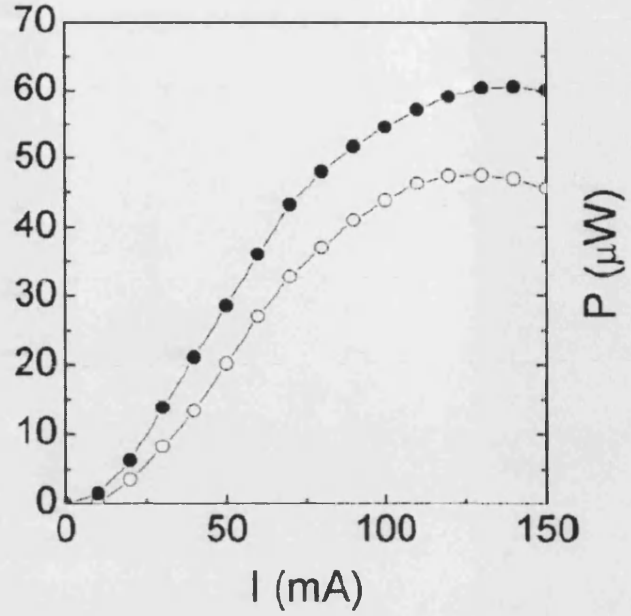

FIGURE 5.3: Light emission power vs. injection current for a GaN-based LED [14]. Note the near-linear characteristic for the injection current between 20 and 70 mA.

the emitted light:

(1) absorption within the LED material,
(2) Fresnel loss at the interface,
(3) critical angle loss due to total internal reflection.

The first mechanism can be seen in the light emitting devices consisting of highly light-absorptive semiconductors, *e.g.*, GaAs. Part of the generated light tends to be absorbed by these semiconductors. In order to re-direct emitted light to the surface, additional distributed Bragg reflectors (DBRs), which have a nearly 100% reflectance at certain wavelength, are of interest to eliminate the absorption effect. The DBR coated onto the backside of the active region can reflect more light propagated downward, resulting in more light emission from the surface (Figure 5.4).

Fresnel loss is a reflection loss. When the refractive index of the semiconductors and medium is different, the light inside the semiconductors will be reflected in the interface, resulting in low extraction of light. Anti-reflection coating, which

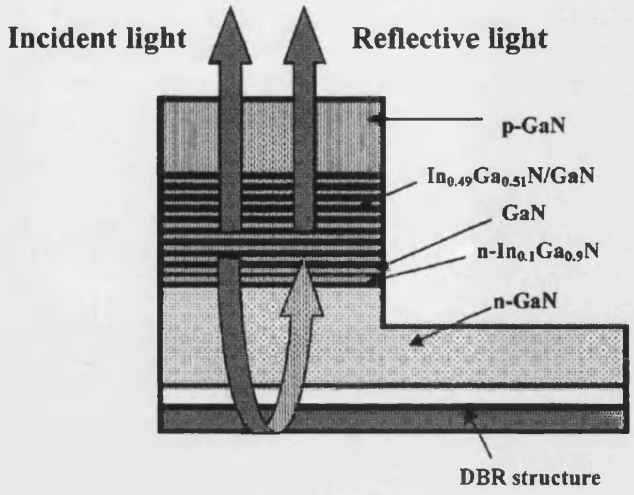

FIGURE 5.4: Illustration of a distributed Bragg reflector (DBR) coated in the backside of a LED structure [22].

employs the destructive wave mechanism, can reduced this effect (see Section 2.2.1).

Critical angle loss is due to the fact that the refractive index of semiconductors is normally larger than the medium. When the light inside the semiconductors reaches the interface, it tends to be bent away from the normal, so the exit angle (θ_t) is greater than the incident angle (θ_i) (Figure 5.5a). It is seen that all the emitted light will be trapped inside the semiconductor when $\theta_t = 90^o$. It is termed the total internal reflection; the incident angle is named the critical angle θ_c. The condition based on Snell's law is given by

$$\begin{aligned} n_2 \sin\theta_i &= n_1 \sin\theta_t \\ \sin\theta_c &= \frac{n_1}{n_2} \end{aligned} \tag{5.6}$$

where n_1 and n_2 are the refractive index for a semiconductor and medium, respectively.

One design to eliminate total internal reflection is to fabricate a cone shape

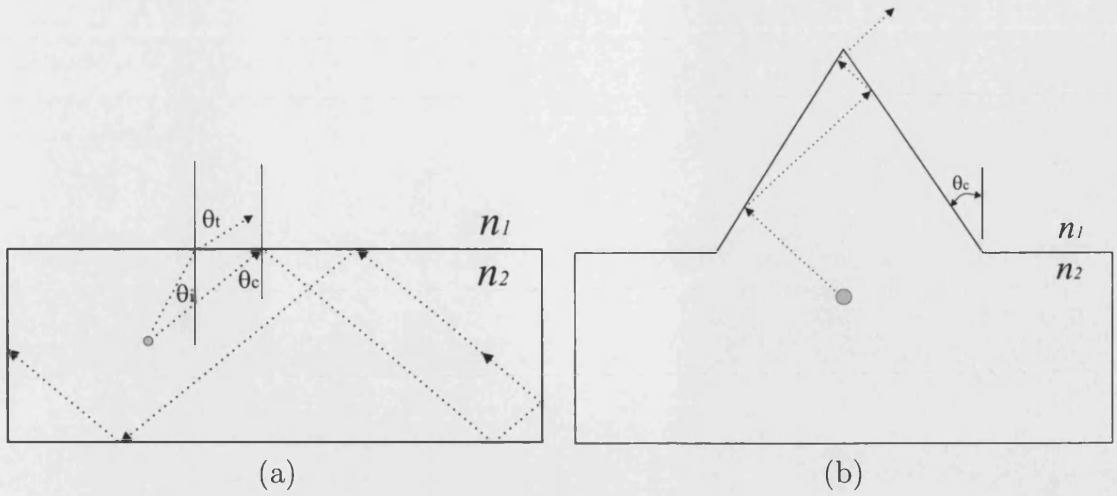

FIGURE 5.5: Illustration of different geometric shapes and light propagation inside (a) a cube-shaped and (b) a cone-shaped LED. Note that θ_c is the angle of total internal reflection.

surface with the sidewall angle equal to critical angle (Figure 5.5b), so that the light inside the cone never reaches its critical angle.

5.3 Current Spreading for LEDs

According to Eq. 5.5 it is seen that a uniform current spreading is desirable for high brightness LEDs. When a current is driven through the p-type contact of a LED, it starts to spread to the location which has the same potential. Figure 5.6 shows the current spreading paths for a conductive-substrate LED. It is seen that increase in p-type ohmic contact area can result in more uniform current spreading, but most of the emitted light will be obstructed by this contact. Sugawara *et al.* [10] used a p^+-GaAs layer under p-type ohmic contact of an AlGaInP LED to increase the current spreading laterally and noted a dramatic improvement (~40 times) in light emission efficiency. In general, improved current spreading for this type of LED mainly involved the use of additional layers between the p-type ohmic contact and p-type semiconductor layer, to match the vertical resistance in the LED structures.

For GaN-based LEDs, the current spreading issue is more important because the

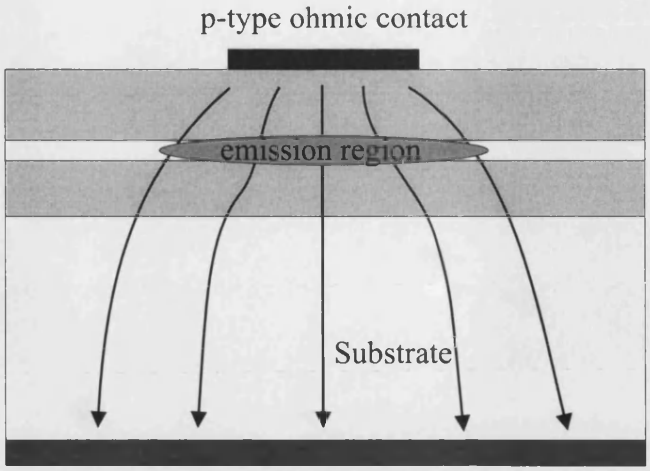

FIGURE 5.6: Illustration of the current spreading for a conductive-substrate type LED.

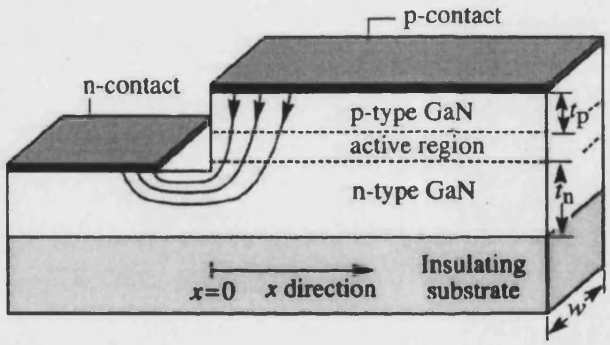

FIGURE 5.7: Illustration of the current spreading for a LED with a insulating substrate [13].

carrier injection is mainly in the lateral direction due to the use of insulating sapphire substrates. In this type of LED (Figure 5.7), the finite resistance of the n-GaN buffer and lower confinement layers can cause current "crowding" near the edge of the contact. Shatalov *et al.* [9] have studied the light emission characteristics for the GaN-based UV LEDs grown on a SiC conductive substrate and sapphire insulating substrate. It was found that the SiC LEDs have a lower differential resistance and turn-on voltage, indicating a lesser effect on the current crowding. The localised high current density will generate more heat and thus damage the devices at these locations.

To solve the current spreading issue for the insulating-substrate type LEDs, Kim *et al.* [14] proposed a simple model for uniform current spreading. Figure 5.8 demonstrates the possible current paths for a GaN LED. Denote transparent p-GaN contact, p-GaN, junction, and n-GaN as the subscription 't', 'p', 'j' and 'n', respectively. The total voltage drop (V_T) across the two contact pads is given

$$\begin{aligned} V_T &= V_t + V_p + V_j + V_n \\ &= J\rho_t(l + t_t) + J\rho_p(l + p_t) + V_j + J\rho_n(L + n_t) \end{aligned} \tag{5.7}$$

where J is the current density, ρ is the resistivity, t is the thickness of the film, and l and L is the length of active region and the distance between two contact pads, respectively. Neglect the vertical components of the transparent layer ($J\rho_t t_t$) and the n-type layer ($J\rho_n t_n$) because t_t and t_n is much smaller than l and L. The possible current paths, A and B, can be given by

$$(V_T)_A = J\rho_t l + J\rho_p t_p + V_j + J\rho_n(L - l) \tag{5.8}$$

$$(V_T)_B = J\rho_p t_p + V_j + J\rho_n L \tag{5.9}$$

Because the voltage drop between two points is independent on the path of current, applying the condition $(V_T)_A = (V_T)_B$ gives

$$J(\rho_t - \rho_n)l \approx 0 \tag{5.10}$$

It is clear that the values of ρ_t and ρ_n must be identical, or either J or l has to be reduced. The authors suggested a contact pad design to reduce the value of l. Figure 5.9 shows a modified p-GaN ohmic contact design which consists of two extended contact pads. Higher light emission intensity was observed although the additional p-GaN ohmic contact pads reduced the emission area, indicating more current passing through the active region.

Guo *et al.* [13] reported a simulation based on the assumptions that the p-GaN

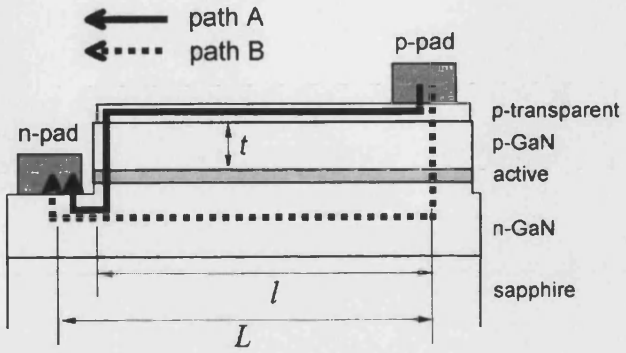

FIGURE 5.8: The possible current paths from the p-type to n-type ohmic contact for a GaN LED [14].

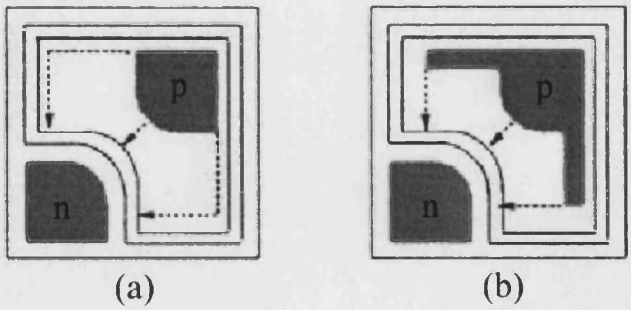

FIGURE 5.9: The contact pad for a (a) commercial LED, and (b) modified LED. Note that the size of the LEDs are 300μm $\times$ 300μm [14].

ohmic contact has equal potential, *e.g.*, a thick and highly conductive layer is used, and ignoring the temperature effect on the voltage drop across the series resistance of a LED. The current density distribution is given by [13]

$$J(x) = J(0)\exp\Big(-\sqrt{\frac{\rho_n}{t_n(\rho_c+\rho_p t_p)}}x\Big) \tag{5.11}$$

where *J(0)* is the current density at the p-type contact edge, ρ_c is the specific contact resistance, ρ_p and ρ_n are the resistivity of p-GaN and n-GaN, and t_p and t_n are the thickness of p-GaN and n-GaN. Denoting L_s as the length where the current density drops to the $1/e$ value of the current density at the edge, *i.e.*, $J(L_s)/J(0) = 1/e$, yields

$$L_s = \sqrt{\frac{t_n(\rho_c+\rho_p t_p)}{\rho_n}} \tag{5.12}$$

It is seen that the resistivity of n-GaN has to be as small as possible in order to minimise the current crowding. Alternatively, one can increase either specific contact resistance, p-GaN resistivity, thickness of p-GaN or n-GaN, to achieve uniform current spreading. However, the increase in specific contact resistance of p-GaN can induce damage to the devices [11], the alternative methods are more practical for high efficiency GaN-based LEDs.

For commercial GaN-based LEDs, a semi-transparent Ni/Au layer is normally used for p-GaN ohmic contact [12]. The thickness of the Ni/Au layer is within 10nm, resulting in a high resistance of this layer. Therefore, Kim *et al.* [15] took into account of this thin Ni/Au layer and expanded Guo's theory of current spreading, deducing a current spreading length (L_s)

$$L_s = \sqrt{\frac{\rho_c+\rho_p t_p}{\left|\frac{\rho_n}{t_n}-\frac{\rho_t}{t_t}\right|}} \tag{5.13}$$

It indicates that uniform current spreading can be achieved by matching the resistance of n-GaN and the contact layer, or by increasing the thickness of the p-GaN layers.

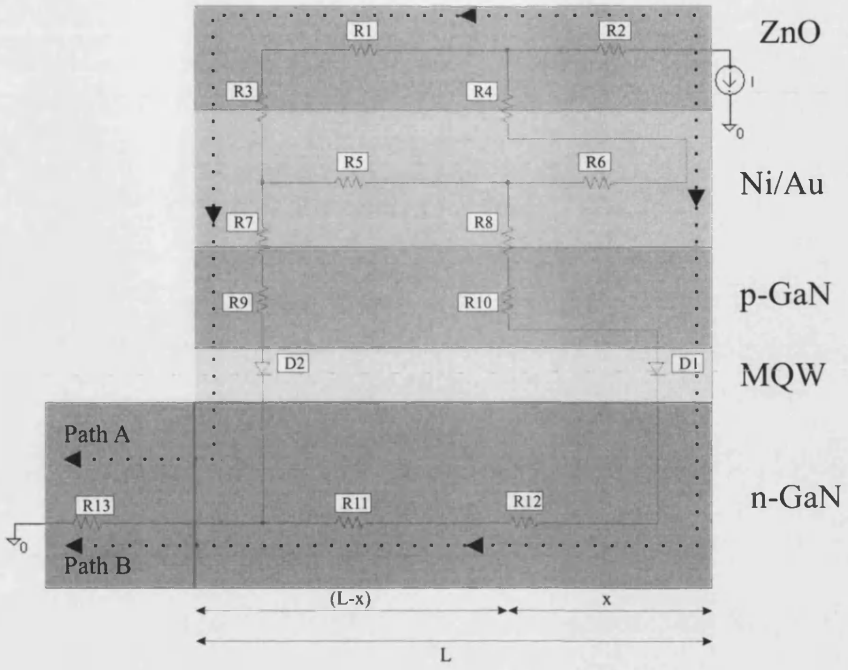

FIGURE 5.10: The equivalent circuit for a GaN LED with a Ni/Au/ZnO contact. Note that paths A and B represents the current flow path.

5.4 Current Spreading Simulation for GaN LED

According to published studies of current spreading for GaN LEDs, the resistivity of the contact layer and their thicknesses are critical. In this study, equivalent circuits for thin Ni/Au/ZnO contacts, thin Ni/Au contacts and highly conductive p-GaN ohmic contacts are used as the simulation models. Circuit analysis software *PSpice 8.0* from MicroSim Corporation was employed in the simulation.

Figure 5.10 illustrates the equivalent circuit for a stripe LED structure used in this simulation. The detailed description of the components is listed in Table 5.1. In this structure, two possible current paths, A and B, are assumed. The current across **D1** can be obtained by sweeping **x** from 0 to the length (**L**) of the LED structure. The structure data is adopted from the real LED structure used in the later experiments and the study of ZnO growth in chapter 2 and listed in Table 5.2.

Based on the settings described above, three equivalent circuits for a 1mm × 100

Components	Description
R1, R2	Lateral resistance of ZnO
R3, R4	Contact resistance between ZnO and Ni/Au
R5, R6	Lateral resistance of Ni/Au
R7, R8	Contact resistance between Ni/Au and p-GaN
R9, R10	Vertical resistance of p-GaN
D1, D2	Multiple quantum well diode
R11, R12	Lateral resistance of n-GaN
I	Current source

TABLE 5.1: List of components used in the simulation.

Description	Value
Resistivity(n-GaN)	0.01 Ω.cm
Resistivity(p-GaN)	4 Ω.cm
Resistivity(Ni/Au)	2×10^{-5} Ω.cm
Resistivity(ZnO)	7.7×10^{-3} Ω.cm
Contact resistance(ZnO – Ni/Au)	8.5×10^{-3} $\Omega.cm^2$
Contact resistance(Ni/Au – p-GaN)	1.19×10^{-2} $\Omega.cm^2$
Contact resistance(Ni/Au – p-GaN) after ZnO coating	4.81×10^{-2} $\Omega.cm^2$
Thickness(n-GaN)	1180 nm
Thickness(p-GaN)	367 nm
Thickness(Ni/Au)	10 nm
Thickness(ZnO)	45 nm
Device length	70 μm, 150 μm, 230 μm, 480 μm, and 1000 μm
Device width	100 μm

TABLE 5.2: List of values used in the simulation.

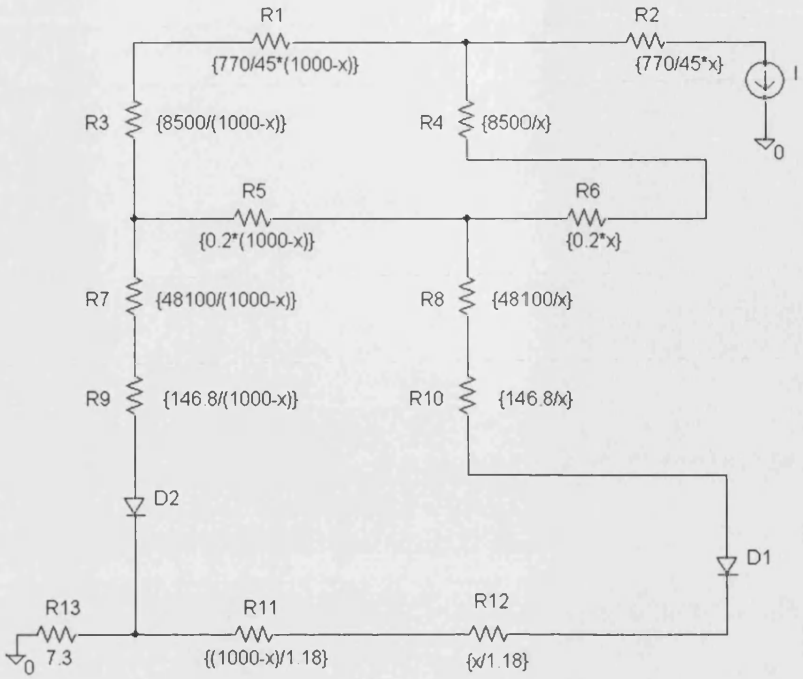

FIGURE 5.11: The equivalent circuit used in the simulation for the GaN LED with a Ni/Au/ZnO contact.

μm strip consisting of a Ni/Au/ZnO, Ni/Au and highly conductive contact for p-GaN (Figure 5.13) were created.

For the Ni/Au/ZnO film, the effective resistivity ($\rho_{(Ni/Au/ZnO)}$) is given by

$$\rho_{(Ni/Au/ZnO)} = \left(\frac{\rho_{Ni/Au} \cdot L}{t_{Ni/Au} \cdot W} + \frac{\rho_{c(ZnO-Ni/Au)}}{L \cdot W} + \frac{\rho_{ZnO} \cdot L}{t_{ZnO} \cdot W}\right) \cdot \frac{(t_{Ni/Au} + t_{ZnO}) \cdot W}{L} \tag{5.14}$$

where $\rho_{Ni/Au}$ and ρ_{ZnO} are the resistivity of Ni/Au and ZnO, respectively, $\rho_{c(ZnO-Ni/Au)}$ is the contact resistance between ZnO and Ni/Au, $t_{Ni/Au}$ and t_{ZnO} are the thicknesses of Ni/Au and ZnO layer, respectively, and L and W are the device length and width. In order to match the condition $\rho_t/t_t = \rho_n/t_n$ which is given by Eq. 5.13, the resistivity of the contact layer must be increased because

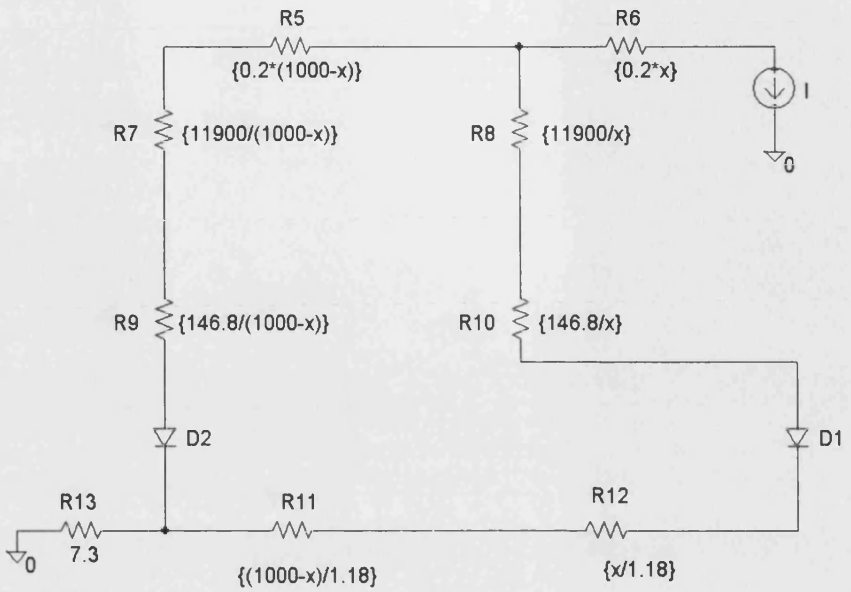

FIGURE 5.12: The equivalent circuit used in the simulation for the GaN LED with a Ni/Au contact.

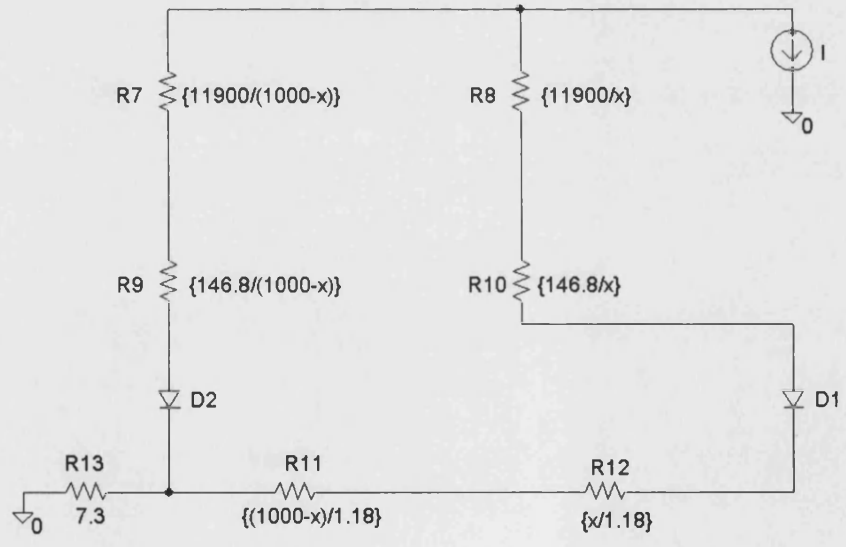

FIGURE 5.13: The equivalent circuit used in the simulation for the GaN LED with a highly conductive contact.

the resistivity of Ni/Au is low. Eq. 5.14 clearly shows that the additional ZnO layer has increased the resistivity of the contact layer, resulting in a better match between the contact and the n-GaN layer. Figure 5.14 shows the simulation results. It is seen that the Ni/Au/ZnO contact gives better current spreading for all cases. It is because of the better match between Ni/Au/ZnO and n-GaN.

In order to compare light emission from the devices, the integration of the current over x was performed because Eq. 5.5 has shown the direct relationship between light output and current. Table 5.3 shows the integrated current and the percentage over the integrated current of the Ni/Au/ZnO contact. The result of Kim's modified contact pad [14] (Figure 5.9) was first examined by this model. It was found that the integrated current was increased by 23% when the contact pad distance was reduced from $\sim$ 230 μm to 70 μm. Kim's experimental work showed that the improvement in light emission power was $\sim$22%. Hence, the simulation results showed good agreement with experimental data.

For the highly conductive contact, the integrated current has only a 6% difference compared with that of Ni/Au/ZnO for the 70μm-long strip, but it significantly increases to 20% for the 150μm-long strip. This indicates that the current crowding is severe for this type of contact. In contrast, the Ni/Au contact has a similar (3%) difference for the 70μm-long strip, but only 10% difference when the device length is increased to 150 μm. This result also shows that different contact pad design has only a minor effect for the contact pad distance, less than 70 μm, for highly conductive contacts and 150 μm for the Ni/Au contact. It implies that a more transparent contact is more suitable for the device which has the contact pad distance less than 150 μm because more light can be extracted from this transparent contact layer.

For large size GaN-based LEDs, the current spreading tends to be worse. Figure 5.14 shows the current distribution curves. It is seen that the current drops to only 20% within 300 μm for the 1mm-long strip which consists a Ni/Au/ZnO contact. The device with a highly conductive contact is much worse. The current drops to 20% within 50 μm. It is because most of the current can spread very rapidly through this highly conductive pad in the lateral direction, and the high resistance induced by the large size of the device results in current preferentially crowding in the area close to the n-GaN contact pad (Figure 5.7).

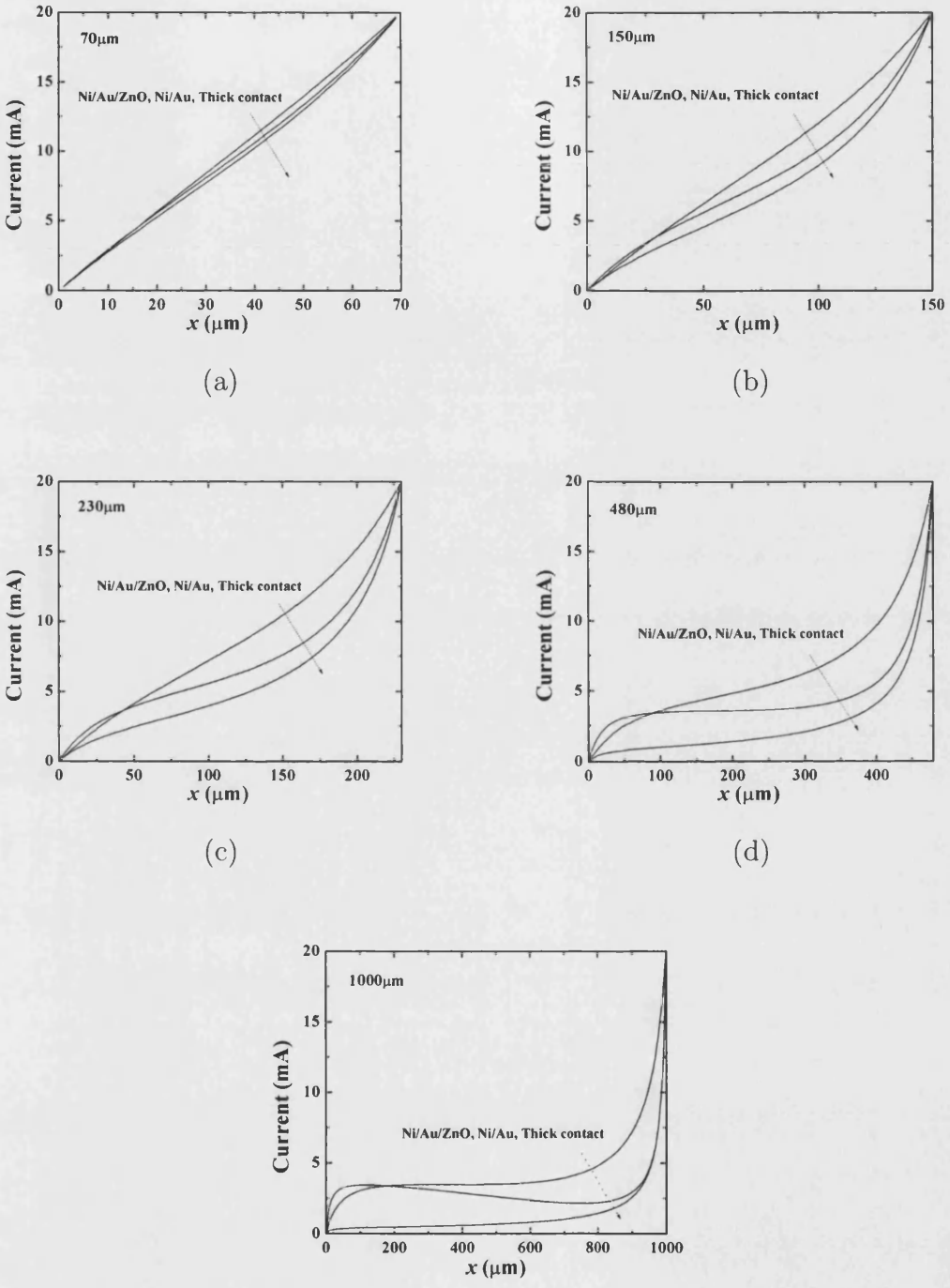

FIGURE 5.14: The simulated current distribution for the rectangular GaN-based LEDs with the width 100 μm and the lengths (a) 70 μm, (b) 150 μm, (c) 230 μm, (d) 480 μm, and (e) 1000 μm.

	70 μm		150 μm		230 μm	
	$\int I\,dx$	%	$\int I\,dx$	%	$\int I\,dx$	%
Ni/Au/ZnO	0.66863	100%	1.38029	100%	1.96445	100%
Ni/Au	0.64830	96.96%	1.23118	89.20%	1.60727	81.82%
Highly conductive	0.62952	94.15%	1.01013	79.79%	1.29982	66.17%

	480 μm		1000 μm	
	$\int I\,dx$	%	$\int I\,dx$	%
Ni/Au/ZnO	3.03523	100%	4.43902	100%
Ni/Au	2.1948	72.31%	3.06038	68.94%
Highly conductive	1.29043	42.52%	1.30229	29.34%

TABLE 5.3: Integrated current over location x and the percentage of the integrated current of Ni/Au/ZnO contact.

5.5 Design of High Efficiency GaN-based LEDs

GaN-based light emitting diodes (LEDs) have been extensively investigated because of their wide applications, *e.g.*, full-colour displays, full-colour indicators, and high efficiency lamps [7, 8, 2]. The improvement of radiation intensity from the active region and the light extraction have been the key issues for high efficiency GaN-based LEDs.

For an increase in radiation extraction from the active region, the device has to either enhance the possibility of radiative recombination in the active region, or increase the current injection to the active region, or both. The former method can be achieved by reducing non-radiative centres, *e.g.*, defects and dislocations, or by the improvements to the design of the active region. Lester *et al.* [16] have reported a high dislocation density for the GaN film grown on a sapphire substrate, due to the lattice mismatch. The authors suggested that the dislocations are not acting as efficient non-radiative recombination sites. However, Sasaoka *et al.* [17] showed that the dislocations are non-radiative recombination centres and may considerably reduce the light output from the LEDs. Thus, an improvement of GaN crystal quality is a way forward to achieve high efficiency LEDs.

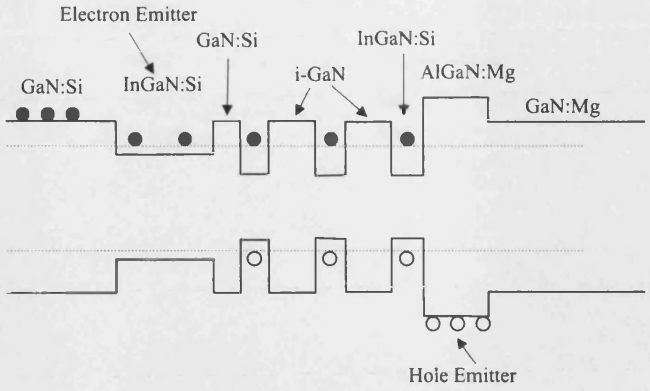

FIGURE 5.15: Energy band diagram of the charge asymmetric resonance tunnelling LED structure [18].

For the active region design, several methods have been proposed. Rebane *et al.* [18] proposed a charge asymmetric resonance tunnelling LED structure to improve the possibility of electron-hole recombination. Figure 5.15 shows the energy band diagram for this structure. The electron emitter is coupled to the active layer through a GaN:Si barrier. This barrier allows electron tunnelling, but can block holes. It has increased the capture efficiency of the electrons into the active layer, suppressed electron leakage into the hole emitter, and reduced the parasitic light generated outside the active layer. Sheu *et al.* [19] have experimentally confirmed the design and an increase in light output, ~2 times, was observed compared with a conventional LED design.

To increase the injection of current to the active region, uniform current spreading is desirable (see Section 5.3). The simulation results (section 5.4) show that the current spreading length can decrease very rapidly in large size LEDs. Thus, a better contact design can improve the current injection which results in higher efficiency of the light emission. Huh *et al.* [21] inserted a current blocking layer beneath the thick p-GaN contact pad. It effectively improved the current spreading and the reported light-output power was 62% higher than that compared with the conventional GaN LED, although the light emitting active area was reduced 30%.

To achieve higher extraction efficiency for the emitted light inside the LED structure, different geometric shapes for LEDs [20], a DBR coating beneath the active

region [22] and anti-reflection optical coating (see chapter 2) can be utilised. Krames *et al.* [20] fabricated a LED with a truncated-inverted-pyramid chip geometry, which decreases the effects of total internal reflection. The external quantum efficiency has been increased ~1.4 times by using this technique. Chen *et al.* [22] reported a coating of DBR on the backside of a GaN LED (Figure 5.4). Because of its nearly 100% reflection the light emitted downward will be reflected back to the GaN, resulting in more light emission from the top and sidewalls. The integrated light output power for the sidewalls and top surface has been increased 2 times.

A Ni/Au/ZnO contact for p-GaN has been theoretically and experimentally shown to improve light extraction (see chapter 2). In addition, the simulation results have demonstrated a more efficient current spreading by using the Ni/Au/ZnO contact. By combining these two effects, it is expected to be more effective in improving light emission from LEDs. The following experimental work will focus on the investigation of the light emission intensity from the different size of GaN-based LEDs.

5.6 Experiment

Metalorganic chemical vapour deposition (MOCVD) was used to grow a 1 μm-thick unintentionally doped GaN buffer layer on a (0001) sapphire substrate. This was followed by the growth of 1.18 μm-thick Si-doped n-GaN. Subsequently, a two-period $In_{0.25}GaN_{0.75}$/GaN multiple quantum well (MQW) was grown, followed by the deposition of a 0.367 μm-thick Mg-doped p-GaN (Figure 5.16). A Ni/Au=5nm/5nm layer was then deposited on the top of this LED structure by an e-beam evaporation system and then annealed at 500 °C in oxygen for 5 minutes. This sample was cut into two pieces and one of the pieces had a 45 nm-thick ZnO film coated on the top of the Ni/Au film by ion beam deposition. The deposition condition is the same as that described in Section 2.3.3. The p-GaN contact was patterned by ion beam etching with circular dots whose radii were 1000 μm, 480 μm and 230 μm. The p-GaN was selectively etched to expose n-GaN layer by inductively-coupled plasma etching. This was followed by the deposition of Ti/Al=20nm/100nm on the n-GaN. The current-voltage (I-V) characteristics of

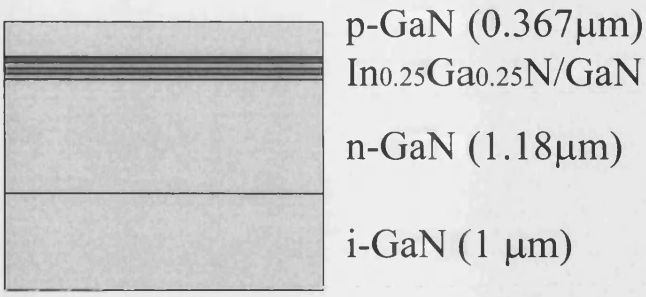

FIGURE 5.16: The structure detail of the LED.

the LEDs were measured using a Keithley 238 high current source measurement unit.

The ZnO film was directly in contact with the Au film of the Ni/Au layer. It indicates the measurement of specific contact resistance for ZnO – Au contact is necessary. The circular transmission line method (CTLM) (see Section 2.1.2) was used to determine the specific contact resistance. The I-V characteristic between the central dot and outer contact is linear, indicating ohmic behaviour. The specific contact resistance of the ZnO – Au interface was estimated at 8.5×10^{-3} $\Omega.cm^2$.

5.7 Results and Discussion

Figure 5.17 shows the I-V characteristic for an LED which consists of a Ni/Au/ZnO (LED[Ni/Au/ZnO]) and Ni/Au (LED[Ni/Au]) contact. It is seen that the differential resistance of LED[Ni/Au/ZnO] is higher than that of LED[Ni/Au]. It is because the series resistance of LED[Ni/Au/ZnO] was increased by the additional ZnO, which can be seen in Eq. 5.14.

Figure 5.18 demonstrates the electroluminescence of the circular LED with radii of 1mm (LED[1mm]), 480μm (LED[480μm]) and 230μm (LED[230μm]). The light emission is measured from the backside of the LED structure. The emission peak wavelength is 460nm for all samples. The peak intensity of LED[Ni/Au/ZnO] is higher than that of LED[Ni/Au] for all size of LEDs, in-

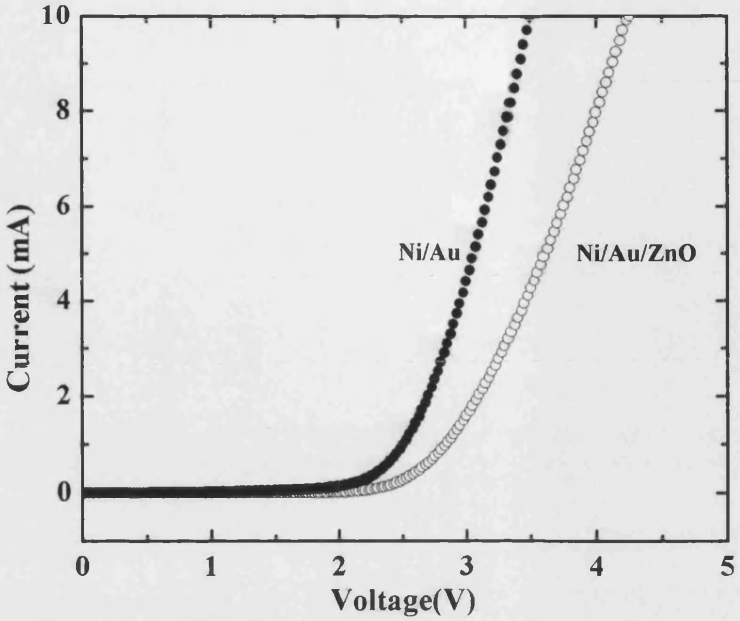

FIGURE 5.17: I-V characteristic of the LED with a Ni/Au and Ni/Au/ZnO contact.

dicating a higher light emission efficiency obtained by LED[Ni/Au/ZnO].

The difference in the current spreading efficiency for LED[Ni/Au/ZnO] and LED[Ni/Au] was examined by comparing the light emission intensity for different size. It is seen that the difference was increased when the device size becomes larger. These results are consistent with the simulations (see Section 5.4).

The difference in the measured emission intensity for LED[230μm] with the Ni/Au/ZnO and Ni/Au contact (Figure 5.18(c)) is 30%, while that of the integrated current in the simulation is 20%, which may be due to the formation of the discontinuous Ni/Au film after annealing (see Section 2.2.5). The additional conductive ZnO film has acted as a conductor between the discontinuous Ni/Au island structures. For large area LEDs, the total contact area of the Ni/Au film may be dramatically reduced because of the formation of these island structures, resulting in a much lower current spreading through the contact layer. This effect can be seen in Figure 5.18(a) and (c). For LED[480μm], the difference in the measured emission intensity is 60%, but the difference in the integrated current from the simulation is only 29%. LED[1mm] is the worst case. The difference

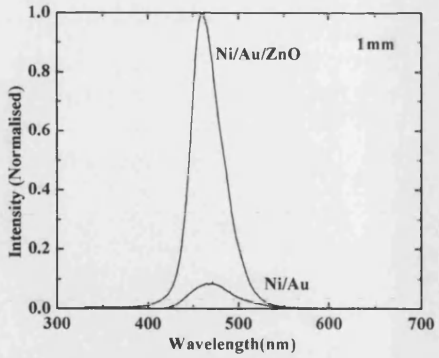

(a)

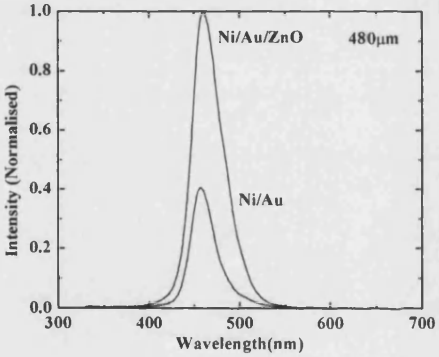

(b)

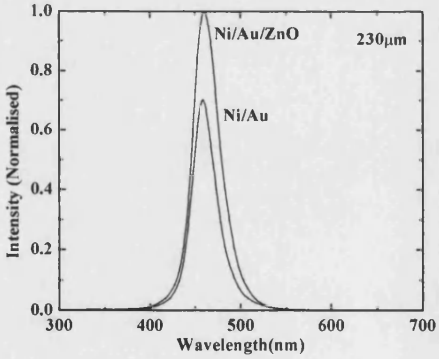

(c)

FIGURE 5.18: The electroluminescence of a circular LED with a radius of (a) 1mm, (b) 480μm, and (c) 230μm at an injected current of 30mA.

between measured emission intensity and simulation result is 90% and 31%, respectively. This result shows that the additional ZnO film has not only acted as an anti-reflection film, but also acted to make the electrical conduct continuous.

5.8 Summary

The design of high efficiency GaN-based LEDs has been undertaken by a simulation of current spreading and later examined by experiments. A simulation involving equivalent circuits and circuit analysis software *PSpice 8.0*, has been made and compared with experimental work. The simulation results are found to be consistent with the experimental work.

The simulation is based on the assumption that the voltage drop between two given paths of current flow from p-contact to n-contact has to be small for uniform current spreading. Consequently the current spreading situation may be evaluated by comparing the voltage difference between two different given paths of the current flow. Thus, an equivalent circuit for the Ni/Au/ZnO, Ni/Au, and highly conductive p-GaN contact was created for the simulation. The simple structure of GaN-based LED, consisting a transparent Ni/Au or Ni/Au/ZnO contact, p-GaN, InGaN quantum well and n-GaN, was used.

The simulation results showed that the Ni/Au/ZnO contact has better current spreading characteristics than the Ni/Au contact, for the contact pad distance 70 μm to 1mm. The difference in the integrated current between these two type of contacts increased from 3% for the 70 μm-long strip to 31% for the 1mm-long strip. For the highly conductive contact, the current spreading is inferior to the Ni/Au/ZnO and Ni/Au contact because the difference in resistivity of the p-GaN contact and n-GaN is large, resulting in larger voltage drop for a given two different paths of current flow. The difference in the integrated current for the Ni/Au/ZnO contact and the highly conductive contact is as high as 72% for the 1mm-long strip.

Circular LEDs with radii of 230 μm, 480 μm and 1 mm were fabricated. The I-V characteristics show that the differential resistance of the LEDs with a

Ni/Au/ZnO contact is larger than that of the LEDs with a Ni/Au contact. This is attributed to the additional ZnO induced increase in series resistance. The difference in light emission intensity between LED[Ni/Au/ZnO] and LED[Ni/Au] was increased when the device size became larger, which is consistent with the integrated current calculated in the simulation. It indicates the current spreading situation may be significantly degraded for large LED[Ni/Au]. By comparing the measured light emission intensity and integrated in the simulation it was found that the consistency is getting worse when the device size becomes larger. It may be due to the formation of discontinuous Ni/Au island structures because the simulation assume a continuous p-GaN contact used. The additional ZnO film has acted to make the film continuous, resulting in a better current spreading though the p-GaN contact layer.

References

[1] J. I. Pankove, and J. E. Berkeyheiser, *Proc. IRE.* **50**, 1976 (1962).

[2] F. Nguyen, *Synthetic Metals* **122**, 215 (2001).

[3] W. J. Gartner, and C. R. Myers, *US Patent* **5,898,381** (1999).

[4] P. Schlotter, J. Baur, Ch. Hielscher, M. Obloh, R. Schmidt, and J. Schneider, *Materials Science & Engineering B* **59**, 390 (1999).

[5] M. J. Hall, B. J. Truesdale, and T. M. Narasimhan, *US Patent* **5,898,381** (1999).

[6] S. M. Sze, *Physics of Semiconductor Devices*, 2nd edition(John Wiley & Sons, Inc., Canada, 1981).

[7] S. Nakamura, T. Mukai, and M. Senoh, *Appl. Phys. Lett.* **64**, 1687 (1994).

[8] H. X. Jiang, S. X. Hin, J. Li, J. Shakya, and J. Y. Lin, *Appl. Phys. Lett.* **78**, 1303 (2001).

[9] M. Shatalov, G. Simin, V. Adivarahan, A. Chitnis, S. Wu, R. Pachipulusu, V. Mandavilli, K. Simin, J. P. Zhang, J. W. Yang, and M. A. Khan, *Jpn. J. Appl. Phys. Part 1* **41**, 5083 (2002).

[10] H. Sufawara, K. Itaya, M. Ishikawa, and G. Hatakoshi, *Jpn. J. Appl. Phys. Part 1* **31**, 2446 (1992).

[11] S. Nakamura, M. Senoh, and T. Mukai, *Appl. Phys. Lett.* **62**, 2390 (1993).

[12] S. Nakamura, T. Yamada, M. Senoh, M. Yamada, and K. Bando, *US Patent* **5,563,422** (1994).

[13] X. Guo, and E. F. Schubert, *J. Appl. Phys.* **90**, 4191 (2001).

[14] H. Kim, J. M. Lee, C. Huh, S. W. Kim, D. J. Kim, S. J. Park, and H. Hwang, *Appl. Phys. Lett.* **77**, 1903 (2000).

[15] H. Kim, S. J. Park, H. Hwanga, and N. M. Park, *Appl. Phys. Lett.* **81**, 1326 (2002).

[16] S. S. Lester, F. A. Ponce, M. G. Craford, and D. A. Steigerwald, *Appl. Phys. Lett.* **66**, 1249 (1995).

[17] C. Sasaoka, H. Sunakawa, A. Kimura, M. Nido, A. Usui, and A. Sakai, *J. Cryst. Growth* **189/190**, 61 (1998).

[18] Y. T. Rebane, Y. G. Shreter, B. S. Yavich, V. E. Bougrov, S. I. Stepanov, and W. N. Wang, *Phys. State Solid A* **180**, 121 (2000).

[19] J. K. Sheu, G. C. Chi, and M. J. Jou, *IEEE Photonic. Tech. Lett.* **13**, 1164 (2001).

[20] M. R. Krames, M. Ochiai-Holcomb, G. E. Höfler, C. Carter-Coman, E. I. Chen, I.-H. Tan, P. Grillot, N. F. Gardner, H. C. Chui, J. W. Huang, S. A. Stockman, F. A. Kish, M. G. Craford, T. S. Tan, C. P. Kocot, M. Hueschen, J. Posselt, B. Loh, G. Sasser, and D. Collins, *Appl. Phys. Lett.* **75**, 2365 (2001).

[21] C. Huh, J. M. Lee, Dong-Joon Kim, and S. J. Park, *J. Appl. Phys.* **92**, 2248 (2002).

[22] C. H. Chen, S. J. Chang, Y. K. Su, G. C. Chi, J. K. Sheu, and J. F. Chen, *IEEE J. Sel. Top. Quant.* **8**, 284 (2002).

Chapter 6

Conclusions and Future Work

6.1 Conclusions

The demands for high efficiency light emitting devices, especially in the blue and UV range, for solid-state lighting applications are continuously growing. Since the 1990s, group III-nitrides have been the most promising materials for these applications. While the crystal growth and doping techniques are gaining great attention, reliable processing and device design for high efficiency light emitting devices is the other critical consideration needed for group III-nitrides to reach their full potential. This thesis has focused on several processing techniques and device designs aimed at improving the brightness of light emitting diodes.

The phenomenon of light extraction from GaN-based surface light emitting devices has been investigated. The mechanism for the increased light transmission in an annealed thin Ni/Au contact was first theoretically and then experimentally conducted. The results showed that the increased light transmission in the Ni/Au contact is mainly due to the open areas induced by the formation of island structures after annealing. This was followed by investigation of the importance of Au in the Ni/Au contact. The presence of Au was demonstrated as being essential for lowering the specific contact resistance. Subsequently, the study of ZnO film growth by ion beam sputtering using a metallic Zn target followed. It

was found that the oxygen flow rate and substrate temperature have significant effects on the structural and electrical properties of the ZnO film. Finally, a novel Ni/Au/ZnO contact for p-GaN was theoretically and experimentally studied. The addition of a ZnO film has effectively increased the light transmission to 89% at a wavelength of 470 nm, which is 15% higher than that of the Ni/Au contact.

The effects of inductively-coupled plasma etching on the etch rate, DC bias and surface morphology for a GaN LED structure was reported. It was found that the ICP power, RF power, chamber pressure, and RF power are the most significant parameters for the etch rate, DC bias, surface roughness, and sidewall angle, respectively. An optimisation method based on the experimental data was developed. Investigation of the damage induced by the SiO_2 ion beam deposition has subsequently been undertaken because SiO_2 is a widely used material for etching masks and insulation. The result demonstrated that the photoluminescence intensity was reduced after the coating with SiO_2.

One novel processing technique involving inductively-plasma etching has been developed for the fabrication of GaN nanotubes. These nanotubes have a wall thickness of $\sim$20 nm and an outer diameter $\sim$200 nm. The etching technique was then applied to the fabrication of n-GaN field emission emitters in the form of nanotubes. The dramatic decrease in the turn-on electric field for electron emission has been observed. It is attributed to the geometric-induced electric field enhancement.

The developed Ni/Au/ZnO and inductively-coupled plasma etching have applied to the fabrication of GaN-based light emitting diodes. The current spreading for this type of light emitting diode was studied first by the analysis of equivalent circuits for the LEDs. The results indicated that the current spreading length is strongly dependent on the p-GaN contact layer. The addition of a ZnO film on the Ni/Au contact has induced a better match to the n-GaN layer, resulting in a better current spreading. It also found that the current crowding for the commercial indicator GaN-based LEDs, which is 300 μm square, is not critical. However, the light emission intensity for the large LEDs is highly sensitive to the p-GaN contact pad design.

6.2 Suggestions for Future Work

In this work, the light transmission for the GaN-based devices has been increased to 89% at a wavelength of 470nm by using a Ni/Au/ZnO contact. However, this Ni/Au/ZnO contact is not feasible for UV LEDs because ZnO has high absorption in the UV light range. Thus, different transparent materials which have low contact resistance with p-GaN have to be used for the anti-reflection design. The low contact resistance may be achieved either by seeking a material which has a comparable work function to p-GaN or developing processing techniques to lower the barrier between contacts and p-GaN.

In the work of inductive-coupled plasma etching for a GaN-based LED, a column structure was formed after etching for all conditions. However, a smooth surface was observed for bulk GaN etching, indicating that the formation of the column structure is related to the additional AlGaN or InGaN layers in the LED structure. More detailed studies are suggested in order to develop an understanding of the formation mechanism. In the work on the damage induced by SiO_2 deposition, the damage has been evaluated by measuring the photoluminescence decrease for a multiple quantum well structure. The damage path and depth may be also investigated by microstructure analysis.

Fabrication of GaN nanotubes is a very attractive proposition because many applications for carbon nanotubes have been explored. In this work, the technique has been applied to the fabrication of field emission emitters. To make GaN nanotubes to reach their full potential in such applications, it is suggested that further effort is placed on understanding the characteristics of the fabrication process and on the properties of the nanotubes.

The importance of the current spreading designs has been shown in this work. The Ni/Au/ZnO contact for p-GaN has demonstrated higher current spreading efficiency than is obtained by conventional Ni/Au contacts. For large p-GaN contact areas, more efficient current spreading design is essential. Efficient current spreading design can be achieved by inserting a more conductive layer between the active region and the n-GaN layer or by use of more complicated designs for p-GaN contact pad.